Investigation of the Formation Process of Recombining Plasmas in the Galactic Supernova Remnants with the Suzaku X-Ray Observatory

Hideaki Matsumura

Department of Physics, Graduate School of Science, Kyoto University
Kitashirakawa Oiwake-cho, Sakyo, Kyoto, Kyoto, 606-8502, Japan
matumura@cr.scphys.kyoto-u.ac.jp

January 5, 2018

Abstract

In most of the supernova remnants (SNRs), plasmas are expected to have an ionization degree below the equilibrium and to be in a ionization-dominant state. Recent observations with Japanese X-ray satellites, ASCA and Suzaku, revealed non-standard plasmas, which have higher ionization degree than expected in a collisional ionization equilibrium. The plasmas are thought to be in a recombination-dominant state, and thus called recombining plasmas (RPs). Such plasmas are not anticipated in a standard picture of the SNR plasma evolution. Although some scenarios are proposed to explain the RPs, the formation process of the RP is not fully understood yet. In any scenario, a key seems to be interactions between the SNR and ambient dense gas.

To understand the formation process of RPs, we perform spatially resolved spectroscopic analyses of X-ray emissions from the Galactic SNRs, G166.0+4.3, IC 443, W44, and W49B with Suzaku. We compare spatial variations of physical parameters of the RPs with distributions of the ambient gas. In all the remnants, the spectral analyses reveal good correlations between locations of plasmas with lower electron temperatures and those of surrounding dense molecular clouds. The lower electron temperatures of the RPs can be explained well by the thermal conduction between an SNR plasma and a molecular cloud. For a more quantitatively investigation, we estimated cooling timescales of the thermal conduction in each remnant. In all the remnants, the conduction timescales are shorter than a characteristic timescale for a plasma to reach collisional ionization equilibrium. Therefore, we conclude that the RPs can be realized by the thermal conduction scenario.

Contents

List of Figures

List of Tables

Chapter 1

Introduction

Supernova remnants (SNRs) are the objects resulting from an explosion of a star, i.e., supernova (SN). Elements up to Fe are created through stellar nucleosynthesis and SN nucleosynthesis and are ejected into the interstellar space. A shock wave caused by an SN explosion propagates in the interstellar space. The expanding shock wave supplies thermal and non-thermal energy into the interstellar space. The shock heats the plasma up to a temperature of $\sim 10^7$ K. Non-thermal population of particles or cosmic rays are widely believed to be generated through the diffusive shock acceleration mechanism working at blast waves of SNRs. Thus, SNe and SNRs act as major sources of metal and energy in galaxies.

X-ray observations provide a powerful probe to study physics regarding SNR plasmas, which emit thermal electron bremsstrahlung and various characteristic emission lines from ions in the X-ray band. In an SNR plasma, ions are gradually ionized by collisions with electrons. The plasma reaches a collisional ionization equilibrium after $\sim 10^5$ yr. Since most of the SNRs have an age of $\lesssim 10^4$ yr, SNR plasmas are naturally expected to have an ionization degree below the equilibrium and to be in a ionization-dominant state. It was found that many SNRs indeed have ionization-dominant plasmas through X-ray observations.

Recent observations with Japanese X-ray satellites, ASCA and Suzaku, however, revealed peculiar plasmas in some SNRs, which have higher ionization degree than expected in a collisional ionization equilibrium. The plasmas are thought to be in a recombination-dominant state, and thus called recombining plasmas (RPs). Such plasmas are not anticipated in the standard picture of the SNR plasma evolution described above. Although some scenarios are proposed to explain the RPs, the formation process of the RP is not fully understood yet. In any scenario, a key seems to be interactions between the SNR and ambient dense gas.

In this thesis, aiming to understand the formation process of the RPs, we analyze Suzaku data of four Galactic SNRs: G166.0+4.3, IC 443, W44, and W49B, and discuss implications of the results. In particular, we carry out spatially resolved spectroscopy in order to study the influence of interactions between the SNR shell and ambient gas on the characteristics of the SNR plasma. The overviews of SNRs and physics regarding SNR plasmas are reviewed in Chapters 2 and 3, respectively. Chapter 4 gives a description of the instruments used for the data analysis. The data analysis and results on G166.0+4.3, IC 443, W44 and W49B are described in Chapters 5, 6, 7, and 8, respectively. In Chapter 9, the results are summarized and the origin of the RPs in the remnants are discussed.

The final conclusion of this thesis is given in Chapter 10.

Chapter 2

Overview of Supernova Remnants

Supernovae (SNe) are the energetic explosive events that occur at the last stage of evolution of stars. An SN explosion releases kinetic energy of $\sim 10^{51}$ ergs, with an initial velocity of $\sim 3 \times 10^4$ km s^{-1}. The expanding forward shock sweeps up the surrounding interstellar medium (ISM) while a reverse shock propagates back into the SN ejecta.

The relics of the SNe, called Supernova remnants (SNRs), can be observed in various energy bands such as radio, optical, X-ray, and gamma ray. SNRs provide us with information about the progenitors, explosion mechanisms, and evolution of the remnants. In this chapter, we explain the basic characteristics of SNe and SNRs.

2.1 Supernovae

2.1.1 Nucleosynthesis

Stellar nucleosynthesis is a generic term of nuclear reactions that elements heavier than H are generated in stars, but that at the time of supernova explosions is called supernova nucleosynthesis and is distinguished. When a high-density part occurs in interstellar gas, gravity in the part becomes strong. Surrounding gas are accumulated by the gravity and stellar temperature increase in inverse proportion to a radius of the star. A thermonuclear fusion reaction will start when a distance between protons in the center is close to beyond the Coulomb barrier which is the repulsion force between protons.

p-p chain process

The proton-proton chain (p-p chain) reaction starts at the phase of stellar evolution when the core temperature reaches $\sim 10^7$ K. The process is described as

$$\begin{aligned} {}^1\mathrm{H} + {}^1\mathrm{H} &\rightarrow {}^2\mathrm{H} + e^+ + \nu_e \\ {}^2\mathrm{H} + {}^1\mathrm{H} &\rightarrow {}^3\mathrm{He} + \gamma \\ {}^3\mathrm{He} + {}^3\mathrm{He} &\rightarrow {}^4\mathrm{He} + 2\,{}^1\mathrm{H}. \end{aligned}$$

The p-p chain is a main process in stars with masses $< 2\,M_\odot$ on their main sequence.

CNO cycle

When the core temperature reaches $\sim 2\times10^7$ K, the other reaction, the CNO (carbon-nitrogen-oxygen) cycle becomes dominant;

$$\begin{aligned}
^{12}\mathrm{C} + {}^{1}\mathrm{H} &\rightarrow {}^{13}\mathrm{N} + \gamma \\
{}^{13}\mathrm{N} &\rightarrow {}^{13}\mathrm{C} + e^{+} + \nu_e \\
{}^{13}\mathrm{C} + {}^{1}\mathrm{H} &\rightarrow {}^{14}\mathrm{N} + \gamma \\
{}^{14}\mathrm{N} + {}^{1}\mathrm{H} &\rightarrow {}^{15}\mathrm{O} + \gamma \\
{}^{15}\mathrm{O} &\rightarrow {}^{15}\mathrm{N} + e^{+} + \nu_e \\
{}^{15}\mathrm{N} + {}^{1}\mathrm{H} &\rightarrow {}^{12}\mathrm{C} + {}^{4}\mathrm{He}.
\end{aligned}$$

He burning process

When H is depleted by the above nuclear fusion reactions, He burning begins in the star's core. Since ^{8}Be is an unstable nucleus, ^{12}C is finally synthesized by triple-alpha process;

$$\begin{aligned}
{}^{4}\mathrm{He} + {}^{4}\mathrm{He} &\rightarrow {}^{8}\mathrm{Be} + \gamma \\
{}^{8}\mathrm{Be} + {}^{4}\mathrm{He} &\rightarrow {}^{12}\mathrm{C} + \gamma \\
{}^{12}\mathrm{C} + {}^{4}\mathrm{He} &\rightarrow {}^{16}\mathrm{O} + \gamma.
\end{aligned}$$

The triple alpha process converts He to C and O.

Fusion of heavier elements

When the temperature exceeds $\sim 6\times10^8$ K in the cores of massive stars, carbon-burning process takes place. The principal reactions are

$$\begin{aligned}
{}^{12}\mathrm{C} + {}^{12}\mathrm{C} &\rightarrow {}^{20}\mathrm{Ne} + {}^{4}\mathrm{He} \\
{}^{12}\mathrm{C} + {}^{12}\mathrm{C} &\rightarrow {}^{23}\mathrm{Na} + {}^{1}\mathrm{H},
\end{aligned}$$

and when the temperature increases, Ne and O burning processes start. These processes are described as

$$\begin{aligned}
{}^{20}\mathrm{Ne} + \gamma &\rightarrow {}^{16}\mathrm{O} + {}^{4}\mathrm{He} \\
{}^{20}\mathrm{Ne} + {}^{4}\mathrm{He} &\rightarrow {}^{24}\mathrm{Mg} + \gamma,
\end{aligned}$$

and

$$\begin{aligned}
{}^{16}\mathrm{O} + {}^{16}\mathrm{O} &\rightarrow {}^{32}\mathrm{S} + \gamma \\
{}^{16}\mathrm{O} + {}^{16}\mathrm{O} &\rightarrow {}^{31}\mathrm{S} + n \\
{}^{16}\mathrm{O} + {}^{16}\mathrm{O} &\rightarrow {}^{31}\mathrm{P} + {}^{1}\mathrm{H} \\
{}^{16}\mathrm{O} + {}^{16}\mathrm{O} &\rightarrow {}^{28}\mathrm{Si} + {}^{4}\mathrm{He},
\end{aligned}$$

respectively. Furthermore, ^{32}S, ^{36}Ar and ^{40}Ca are synthesized by the alpha capture of ^{28}Si.

When the temperature exceeds $\sim 4 \times 10^9$ K, Si burning process starts. Si, S, Ar and Ca capture ^{4}He and synthesize iron group elements such as Cr, Mn, Ti, Fe, Co, Ni and Zn. In the complete Si burning process, most of Si burns out and a large amount of ^{56}Ni is synthesized. ^{56}Fe and ^{56}Co are generated by the the beta decay of ^{56}Ni.

In a star whose mass is larger than ~ 8 solar mass ($M_\odot$), the C burning progresses and produces O + Ne + Mg. If the mass exceeds $\sim 10\,M_\odot$, heavier elements from Si to Fe are synthesized in order. Therefore, in a massive star, an onion-like structure formed at the final stage of its evolution (Figure 2.1).

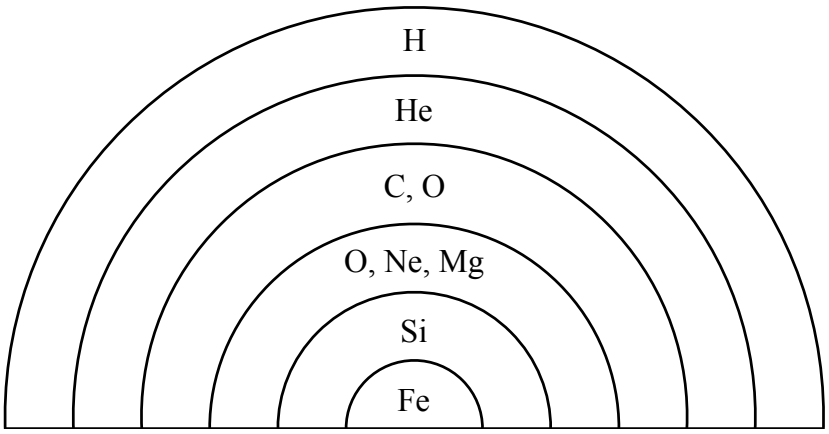

Figure 2.1: Scheme of onion-like structure in a massive star.

2.1.2 Classification of Supernovae

The fundamental classification scheme of SNe is traditionally based on their optical spectra and light curves as shown in Figure 2.2. If an optical spectrum lacks absorption lines of hydrogen Balmer series, the SN is classified as Type I. On the other hand, the SN is classified as Type II when its spectrum contains the hydrogen lines (Minkowski, 1939, 1940). Type I SNe are sub-classificated according to the presence of Si and He absorption feature (e.g., Elias et al., 1985; Wheeler et al., 1987). The SNe with strong silicon feature are classified as Type Ia. The SNe without strong silicon feature and with helium feature are defined as Type Ib, whereas those without silicon and helium features are classified as Type Ic. Subclasses of Type II SNe are distinguished by the shape of their light curves. The SNe are defined as Type II-L if the shapes of the light curves are linear, whereas the light caves are plateau in the Type II-P SNe (e.g., Barbon et al., 1973). The typical light curves of each SN type are shown in Figure 2.3.

As can be seen from the definition, this classification dose not reflect explosion mechanisms of SNe. The progenitors of Type Ia SNe are presumed to be white dwarfs with near-Chandrasekhar mass ($\sim 1.4\,M_\odot$), whereas Type II progenitors are considered to be massive stars ($M \gtrsim 10\,M_\odot$). We describe details of the characteristics for Types Ia and II in the following. Although the spectra of Type Ib SNe lacks hydrogen absorption lines, the property of their light curves is very similar to those of Type II SNe. Furthermore, Type Ib SNe are observed only in spiral galaxies and star forming regions. Therefore, the

progenitors of Type Ib SNe are presumed to be massive stars that have lost their hydrogen envelopes. The progenitors of Type Ic SNe are also presumed to be massive stars, which may be progenitors of gamma-ray bursts (GRBs).

Type Ia Supernovae

Type Ia SNe are observed in all types of galaxies including elliptical galaxies, where no massive stars exist. The lack of hydrogen absorption lines in the Type Ia spectra suggests that progenitors do not have outer hydrogen envelopes. As we mentioned, the progenitor of Type Ia SNe is likely to be while dwarfs. When the mass of the white dwarf reaches about the Chandrasekhar limit ($1.4\,M_{\odot}$), its gravity exceeds the electron degeneracy pressure, and the carbon burning is ignited as the core. Nuclear fusion advances explosively, and the star is totally disrupted. This explosion does not leave a compact object such as a neutron star or a black hole. Type Ia SNe mainly yield Fe-peak elements and intermediate-mass elements Si to Ca. In the literature of nucleosynthesis models of Type Ia SNe, the heavy elements such as Si and Fe are selectively synthesized (Nomoto et al., 1984; Iwamoto et al., 1999).

Two possible scenarios are considered for Type Ia SNe. One is the single degenerate scenario (Whelan & Iben, 1973), which assumes a white dwarf accreting from a nondegenerate companion. Webbink (1984) proposed the other scenario; the double degenerate scenario. They assumed the merger of two white dwarfs whose combined mass exceeds the Chandrasekhar limit. One of the proofs to support the single degenerate scenario is possible detection of Tyhco Brahe's 1572 SN (Ruiz-Lapuente et al., 2004). They suggested that the SN was occurred by a binary system of the while dwarf and the red giant star. On the other hand, the results of SN 2009dc, whose progenitor mass exceeds the Chandrasekhar limit, supports the degenerate scenario (e.g., Yamanaka et al., 2009). The origin of Type Ia SNe is still under debate.

Type II Supernovae

Type II SNe are the origin of massive stars with the main sequence masses of $\geq 10\,M_{\odot}$. In these massive stars, the nucleosynthesis proceeds to produce Fe in the core. When the central temperature in the Fe core exceeds $\sim 3 \times 10^9$ K, photo-disintegration of Fe nuclei takes place;

$$\begin{aligned} {}^{56}\mathrm{Fe} &\rightarrow 13\,{}^{4}\mathrm{He} + 4\,n - 124.4\ \mathrm{MeV} \\ {}^{4}\mathrm{He} &\rightarrow 2\,{}^{1}\mathrm{H} + 2\,n - 28.3\ \mathrm{MeV}. \end{aligned}$$

The star cannot support the gravity any more and collapses gravitationally because the thermal energy is absorbed in the reaction. The inflating matter released the gravitational energy which is $\sim 10^{53}$ ergs by the gravitational collapse in total. The gravitational energy creates a shock wave which propagates outward. The kinetic energy of the explosion is typically $\sim 10^{51}$ ergs because neutrinos carried out 99% of the gravitational binding energy. This explosion leaves a compact object such as a neutron star or a black hole.

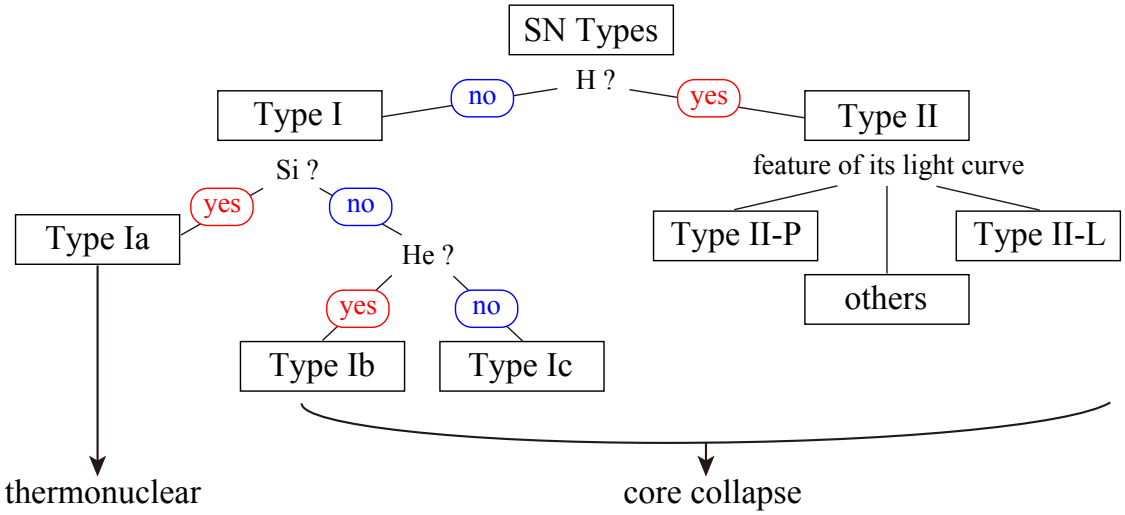

Figure 2.2: Classification scheme of supernovae based on the features of the spectra and light curves.

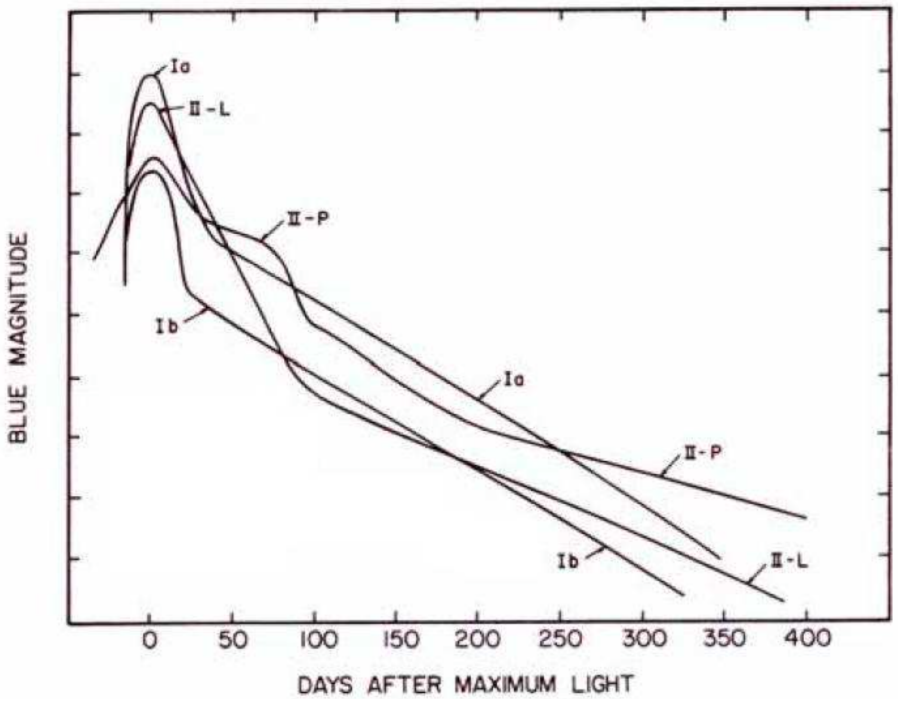

Figure 2.3: Light curves for Type Ia, Ib, II-P, and II-L supernovae (Wheeler & Harkness, 1990).

2.2 Shock Wave Heating

The supersonic SN explosion generates shock wave which compresses, heats up, and accelerates the media. As shown in Figure 2.4, we take a coordinate to be the rest frame of the shock, and define upstream and downstream. The tangential component of the gas velocity is assumed to be zero on both sides. Then, conservation of mass, momentum, and energy across the shock front can be described as

$$\rho_{\rm u} v_{\rm u} = \rho_{\rm d} v_{\rm d} \tag{2.1}$$

$$\rho_{\rm u} v_{\rm u}^2 + p_{\rm u} = \rho_{\rm d} v_{\rm d}^2 + p_{\rm d} \tag{2.2}$$

$$\frac{1}{2} v_{\rm u}^2 + w_{\rm u} = \frac{1}{2} v_{\rm d}^2 + w_{\rm d}, \tag{2.3}$$

respectively, where ρ, v, p, w are the mass density, velocity, pressure, and enthalpy of upstream (subscript u) and downstream (subscript d), respectively. Considering ideal gas, the enthalpy is given as

$$w = C_p T = \frac{\gamma p}{(\gamma - 1)\rho} \ , \tag{2.4}$$

where C_p, γ are the heat capacity at constant pressure and the ratio of the heat capacity at constant pressure to that at constant volume ($= C_p/C_V$), respectively.

From Equations 2.1, 2.2, 2.3 and 2.4, relations between the physical condition of the upstream and the downstream, called Rankine-Hugoniot relations, are obtained as

$$\frac{\rho_{\rm u}}{\rho_{\rm d}} = \frac{v_{\rm d}}{v_{\rm u}} = \frac{(\gamma+1)p_{\rm u} + (\gamma-1)p_{\rm d}}{(\gamma-1)p_{\rm u} + (\gamma+1)p_{\rm d}} \tag{2.5}$$

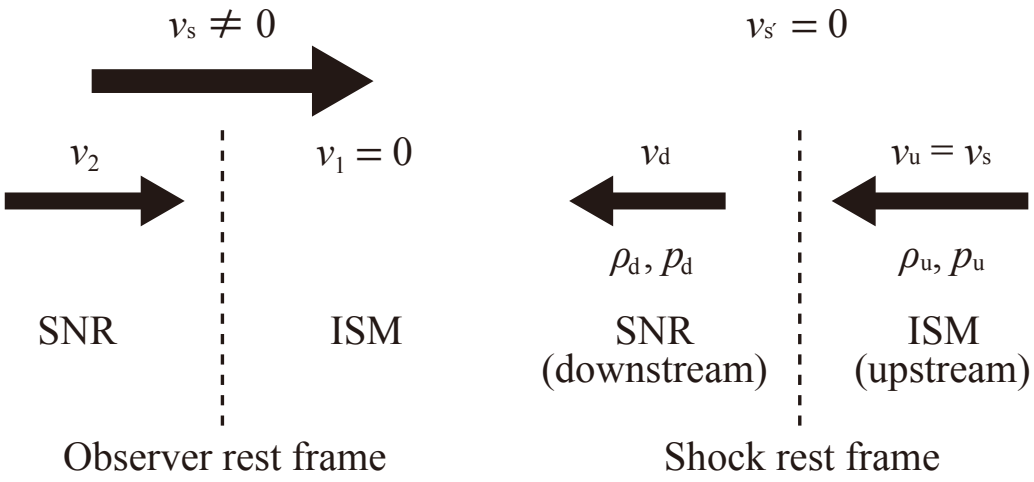

Figure 2.4: A schematic view of the shock wave in observer rest frame (left) and shock rest frame (right). v, ρ, p, w, and T are the velocity, density, pressure, enthalpy, and temperature, respectively. Subscripts s, u and d indicate shock, upstream and downstream, respectively.

$$\frac{p_{\rm u}}{p_{\rm d}} = \frac{(\gamma+1)\rho_{\rm u} - (\gamma-1)\rho_{\rm d}}{(\gamma+1)\rho_{\rm d} - (\gamma-1)\rho_{\rm u}} \tag{2.6}$$

$$\frac{T_{\rm d}}{T_{\rm u}} = \frac{p_{\rm d}\rho_{\rm u}}{p_{\rm u}\rho_{\rm d}} = \frac{p_{\rm d}}{p_{\rm u}}\frac{(\gamma+1)p_{\rm u} + (\gamma-1)p_{\rm d}}{(\gamma-1)p_{\rm u} + (\gamma+1)p_{\rm d}} \tag{2.7}$$

$$v_{\rm u}^2 = \frac{1}{2\rho_{\rm u}}\{(\gamma-1)p_{\rm u} + (\gamma+1)p_{\rm d}\} \tag{2.8}$$

$$v_{\rm d}^2 = \frac{1}{2\rho_{\rm u}}\frac{\{(\gamma+1)p_{\rm u} + (\gamma-1)p_{\rm d}\}^2}{(\gamma-1)p_{\rm u} + (\gamma+1)p_{\rm d}}. \tag{2.9}$$

Assuming the strong shock ($p_{\rm d}/p_{\rm u} \gg 1$), Equations 2.6, 2.7, 2.8 and 2.9 can be rewritten as

$$\frac{\rho_{\rm u}}{\rho_{\rm d}} = \frac{v_{\rm d}}{v_{\rm u}} = \frac{\gamma-1}{\gamma+1} \tag{2.10}$$

$$\frac{T_{\rm u}}{T_{\rm d}} = \frac{p_{\rm d}}{p_{\rm u}}\frac{\gamma-1}{\gamma+1} \tag{2.11}$$

$$v_{\rm u}^2 = \frac{(\gamma+1)p_{\rm d}}{2\rho_{\rm u}} \tag{2.12}$$

$$v_{\rm d}^2 = \frac{(\gamma-1)^2 p_{\rm d}}{2(\gamma+1)\rho_{\rm u}}, \tag{2.13}$$

respectively. Since $v_{\rm u} = v_{\rm s}$ (see Figure 2.4), we can derive the mean shock velocity at the rest frame of the upstream using Equations 2.10 and 2.13 as

$$kT_{\rm d} = \mu m_{\rm H}\frac{p_{\rm d}}{\rho_{\rm d}} = \frac{2(\gamma-1)}{(\gamma+1)^2}\mu m_{\rm H} v_{\rm s}^2, \tag{2.14}$$

where k, μ and $m_{\rm H}$ are the Boltzmann constant, the mean atomic weight and the hydrogen mass, respectively. Assuming the non-relativistic monatomic gas ($\gamma = 5/3$), the density and velocity ratios in the downstream to the upstream, and the post-shock temperature are obtained as

$$\frac{\rho_{\rm d}}{\rho_{\rm u}} = 4 \tag{2.15}$$

$$\frac{v_{\rm d}}{v_{\rm u}} = \frac{1}{4} \tag{2.16}$$

$$kT_{\rm d} = \frac{3}{16}\mu m_{\rm H} v_{\rm s}^2, \tag{2.17}$$

respectively. The post-shock temperature is determined only by the shock speed. In addition, the shock wave heats up all particles with different masses to the similar velocities determined by the shock speed. Therefore, the energy non-equipartition between protons and electrons are expected. The shock wave heating can be understood as the energy conversion from the kinetic energy to the internal (thermal) energy.

2.3 Evolution of SNRs

An SNR is generally composed of an expanding ejecta material (ejecta) and ISM swept up by the shock wave. The evolution of SNRs can be divided into following several phases; free expansion, adiabatic, radiative cooling, disappearance, and transition phases (see e.g., Cioffi et al., 1988; Truelove & McKee, 1999). These phases are mainly determined by the ratio of a mass of the ejecta ($M_{\rm ej}$) to that of the swept-up ISM ($M_{\rm ISM}$). For simplicity, we assume that the density of the ambient gas is uniform.

2.3.1 Free expansion phase

After the SN explosion, the stellar materials are ejected around. The explosion generates a forward shock wave and compresses surrounding ISM. In the initial phase, the ejecta expands keeping its kinetic energy and velocity constant because $M_{\rm ISM}$ is much smaller than $M_{\rm ej}$ and is negligible. The expansion velocity ($v_{\rm s}$) is $\sim 10^4$ km s^{-1}, which is much larger than the sound speed of ~ 10 km s^{-1} in the surrounding ISM. Most of the explosion energy (E) is released the kinetic energy while only 2–3% of its total is converted into thermal energy. Therefore, $v_{\rm s}$ can be described as

$$v_{\rm s} = \sqrt{\frac{2E}{M_{\rm ej}}} = 1.0 \times 10^9 \left(\frac{E}{10^{51}\ {\rm erg}}\right)^{1/2} \left(\frac{M_{\rm ej}}{M_\odot}\right)^{-1/2} \ {\rm cm\ s^{-1}}\ . \tag{2.18}$$

The mass of the swept-up ISM is expressed by

$$M_{\rm ISM} = \frac{4}{3}\pi R_{\rm s}^3 \mu m_{\rm H} n_0, \tag{2.19}$$

where $R_{\rm s}$ and n_0 is the radius of the expanding shell and the hydrogen number density of the swept-up ISM, respectively. Since the free expansion phase continues until that $M_{\rm ISM}$ is close to $M_{\rm ej}$, the timescale since the explosion (t) can be approximately estimated at

$$t \sim 1.9 \times 10^2 \left(\frac{E}{10^{51}\ {\rm erg}}\right)^{-1/2} \left(\frac{M_{\rm ej}}{M_\odot}\right)^{5/6} \left(\frac{\mu}{1.4}\right)^{-1/3} \left(\frac{n_0}{1\ {\rm cm^{-3}}}\right)^{-1/3} \ {\rm yr} \tag{2.20}$$

from an equation of $R_{\rm s} = v_{\rm s} t$ and Equations 2.18 and 2.19. The free expansion phase typically continues for $t \lesssim 10^{2-3}$ yr as shown in Equation 2.20.

2.3.2 Adiabatic phase (Sedov phase)

When $M_{\rm ISM}$ becomes much larger than $M_{\rm ej}$ (typically $\gtrsim 10\ M_{\rm ej}$), the kinetic energy is transferred to the swept-up ISM. In a phase where energy loss by radiation cooling from the ISM can be negligible, the expansion is adiabatic, and therefore, this phase is called the adiabatic phase. In the adiabatic phase, we can be applied the Sedov solution to quantify an estimate for the outcome of a point explosion; density, pressure, and temperature of the gas, and the distribution of the shock velocity. Therefore, the phase is also called the Sedov phase. The radius and velocity of the blast wave, and the mean temperature just behind the shock front are described as

$$R_{\rm s} = 4 \times 10^{19} \left(\frac{t}{10^4 \text{ yr}}\right)^{2/5} \left(\frac{E}{10^{51} \text{ erg}}\right)^{1/5} \left(\frac{n_0}{1 \text{ cm}^{-3}}\right)^{-1/5} \text{ cm} \quad (2.21)$$

$$v_{\rm s} = \frac{dR_{\rm s}}{dt} = 5 \times 10^7 \left(\frac{t}{10^4 \text{ yr}}\right)^{-3/5} \left(\frac{E}{10^{51} \text{ erg}}\right)^{1/5} \left(\frac{n_0}{1 \text{ cm}^{-3}}\right)^{-1/5} \text{ cm s}^{-1} \quad (2.22)$$

$$T_{\rm s} = 3 \times 10^6 \left(\frac{t}{10^4 \text{ yr}}\right)^{-6/5} \left(\frac{E}{10^{51} \text{ erg}}\right)^{2/5} \left(\frac{n_0}{1 \text{ cm}^{-3}}\right)^{-2/5} \text{ K}, \quad (2.23)$$

respectively. As shown in those equations, the evolution during this phase is determined only by t, E and n_0. Since the ISM density is much larger than that of the ejecta, X-ray emission from the ISM is dominant at all the X-ray emission in the remnant. Therefore, n_0 and $T_{\rm s}$ can be estimated from the thermal X-ray spectrum of the SNR. The radius $R_{\rm s}$ is also determined observationally if the distance to the remnant is known, and then, we can derive t and E from Equations 2.21 and 2.23. Until the end of the phase ($t \sim 10^{3-4}$ yr), $\sim$ 70% of the initial explosion energy is converted into the thermal energy (Chevalier, 1974).

In transition phase between the free expansion and the adiabatic phase, the outer shock (forward shock) sweeps up the ISM and its speed decreases with time according to Equation 2.22, whereas the inner ejecta keeps expanding at constant speed in Equation 2.18. The swept-up ISM pushes back on the ejecta and causes another shock wave to propagate inward through the ejecta, called "reverse shock" (McKee, 1974). The forward shock heats surrounding ISM, whereas the ejecta is heated by the reverse shock. Figure 2.5 shows a schematic view of the SNR in the transition phase.

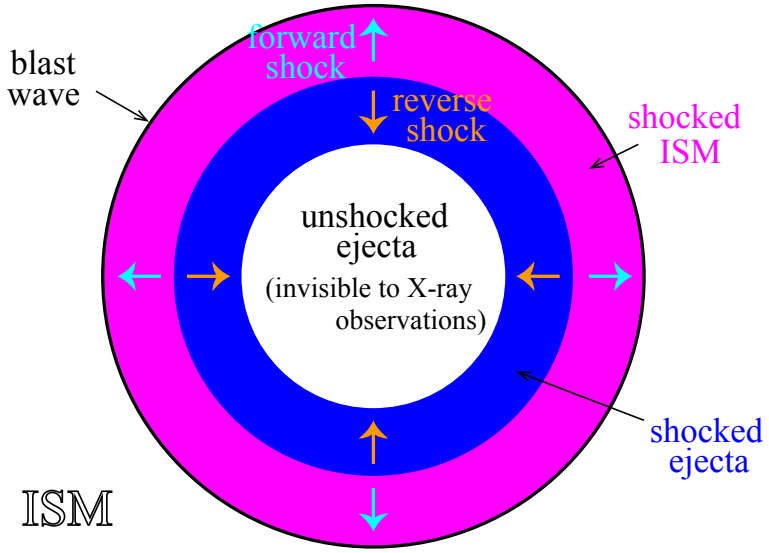

Figure 2.5: A schematic view of the SNR in the transition phase between the free expansion and the adiabatic phase.

2.3.3 Radiative cooling phase

As shown in Equations 2.22 and 2.22, $v_{\rm s}$ and $T_{\rm s}$ decrease over time during the adiabatic phase. When the radiative energy loss becomes large compared with the internal energy of the remnant, the evolution is no longer adiabatic. This phase is called the radiative cooling phase. As shown in Figure 2.6, electrons recombine with the heavy elements, such as C and O, with $T_{\rm s} \lesssim 3 \times 10^5$ K, and a shell of the SNR becomes cooler and denser. The shell expands conserving its momentum, and an equation of $PV^\gamma =$ const. is established, where P and V are the mean pressure and the volume of the gas, respectively. Therefore, assuming the non-relativistic monatomic gas ($\gamma = 5/3$), the time dependency of the shock expansion is described as

$$R_{\rm s} \propto t^{2/7} \tag{2.24}$$

$$v_{\rm s} \propto t^{-5/7} \ . \tag{2.25}$$

McKee & Ostriker (1977) called this stage the pressure-driven snowplow phase.

When the temperature cools down further, the shock expands conserving its radial momentum; $M_{\rm s} v_{\rm s} =$ const., where $M_{\rm s}$ is the mass of the shell because the pressure can be ignored. In the stage called the momentum-conserving snowplow phase (Cioffi et al., 1988), the time dependency of the shock expansion is obtained as

$$R_{\rm s} \propto t^{1/4} \tag{2.26}$$

$$v_{\rm s} \propto t^{-3/4}. \tag{2.27}$$

The radiative cooling phase continues for $t \gtrsim 10^4$ yr.

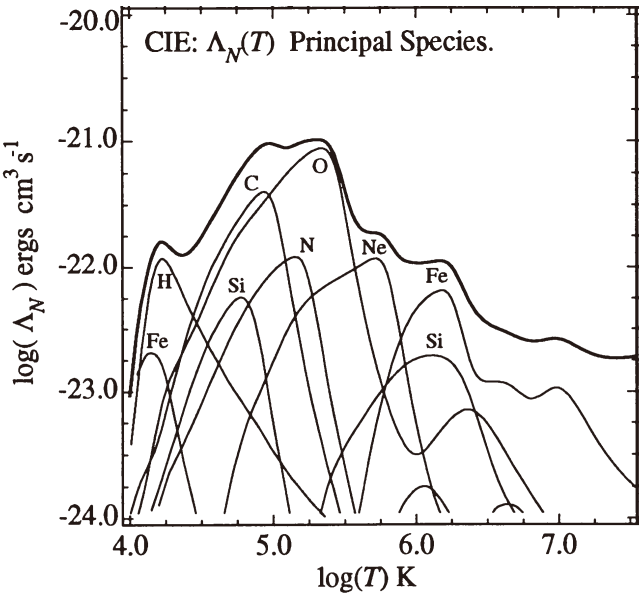

Figure 2.6: Cooling coefficient for an optically-thin thermal plasma with solar abundances (Anders & Grevesse, 1989) as a function of plasma temperature (Sutherland & Dopita, 1993).

2.3.4 Disappearance phase

After the shock velocity drops to the sound speed in the ISM, the SNR lose its boundary and goes out into the ISM. The age of SNRs in the disappearance phase is $\sim 10^5$–10^6 yr.

2.4 Classification of SNRs

In most of SNRs, their X-ray morphologies are almost the same as those in the radio band. SNRs have been classified into broad categories of shell-like, plerionic (Crab-like) and composite, based on their radio morphologies. Shell-like SNRs are characterized by limb-brightened morphology in radio and X-ray bands as shown in Tycho's SNR (Figure 2.7). The radio emission is mainly produced by synchrotron radiation from electrons which is accelerated up by a blast wave. The X-ray emission is composed of thermal and/or non-thermal X-rays. The origin of the non-thermal X-ray emission is the same as the radio emissions but the energy of the accelerated electrons is the TeV order. We describe the origin of the thermal X-rays in Capter 3. Most of the shell-like SNRs are young SNRs in the free expansion or adiabatic phases such as Tycho, Kepler and Cassiopeia A.

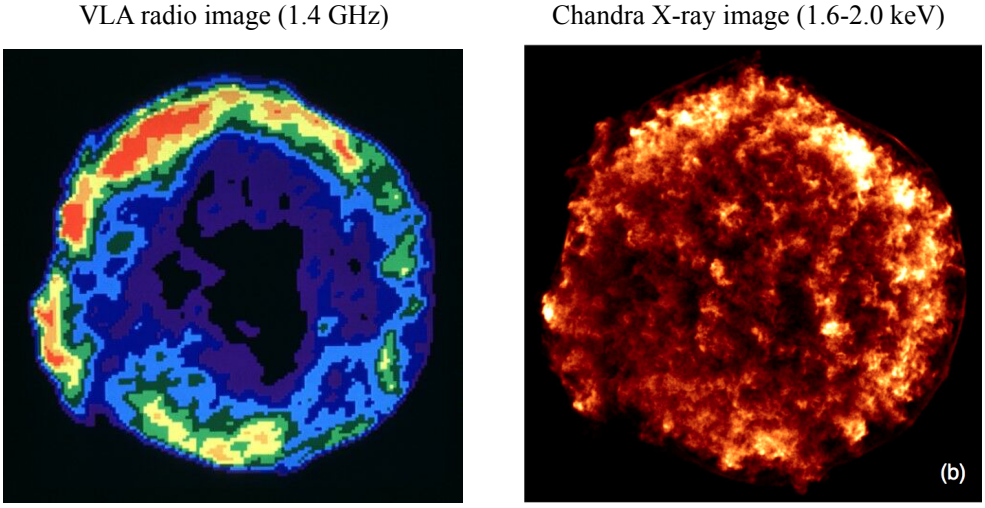

Figure 2.7: X-ray and radio images of the shell-like SNR, Tyhco. (right) X-ray image in the energy band of 1.6-2.0 keV with Chandra (Lu et al., 2015). (left) 1.4 GHz radio continuum image from with the Very Large Array (VLA; Credit Radio: NSF/NRAO/VLA).

The plerionic SNRs have center-filled emissions in both the radio and X-ray bands (see emissions from 3C 58 in Figure 2.8). Crab Nebula is the most famous remnant of this type, and therefore, the plerionic SNRs are also called Crab-like SNRs. The origin of the central emission is a pulsar wind nebula (PWN) powered by a rapidly rotating neutron star (pulsar). The energy loss of the pulsar causes relativistic electrons and positrons which radiates a synchrotron radiation by interacting with the magnetic field of the pulsar. If the center-filled emission from a PWN coexists with a shell emission as those of the shell-like SNRs, the remnants are categorized into composite SNRs. We show

the emissions from a typical composite SNR G11.2-0.3 in Figure 2.9. These remnants associating with a neutron star account for $\sim 15\%$ of all X-ray-detected Galactic SNRs.

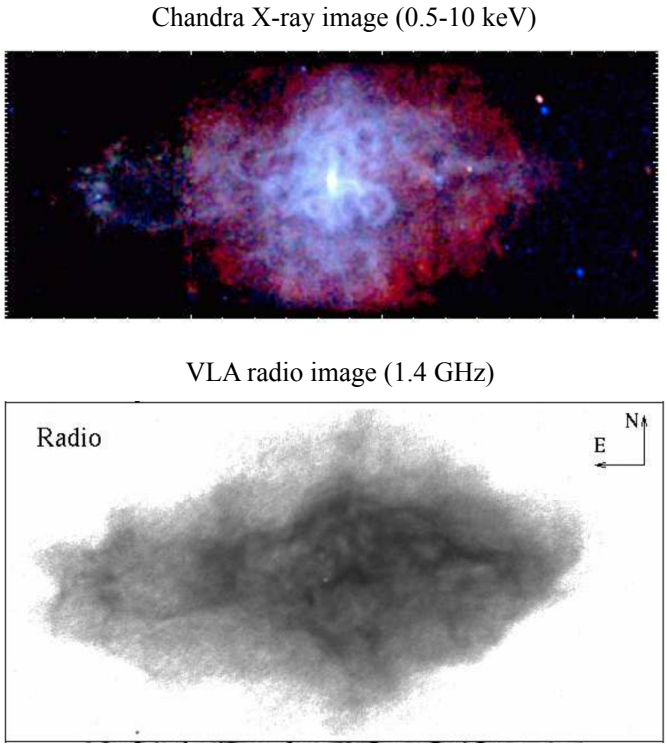

Figure 2.8: X-ray and radio images of the plerionic SNR, 3C 58 (Slane et al., 2004). (upper) X-ray image in the energy band of 0.5-10.0 keV with Chandra. (bottom) 1.4 GHz radio continuum image from with VLA.

Rho & Petre (1998) claimed that some SNRs have a radio shell with a center-filled X-ray morphology. They classified them into mixed-morphology SNRs. Figure 2.10 shows X-ray and radio images of a typical mixd-morphology SNR, W44. Rho & Petre (1998) also claimed that $\sim 25\%$ of the X-ray-detected SNRs are categorized into the mixed-morphology class. While the formation mechanism of the mixed-morphology SNRs has not been fully understood, two scenarios are mainly considered. One is the evaporating cloudlet scenario (White & Long, 1991), and the other is the thermal conduction scenario (Cox et al., 1999; Shelton et al., 1999). White & Long (1991) suggested that many small clouds in the center of the remnant are heated by the blast wave and evaporate, and then, emit X-rays. Cox et al. (1999); Shelton et al. (1999) considered that outer X-ray plasma are cooled by the thermal conduction between the plasma and molecular clouds associated with the remnant, and the center-filled X-ray morphology are produced. In either scenario, interactions between the blast wave and the clouds play an important role in the formation of the X-ray morphology. Most mixed-morphology SNRs are actually associated with molecular clouds as indicated by CO line emissions or OH (1720 MHz) masers (e.g., Lazendic & Slane, 2006).

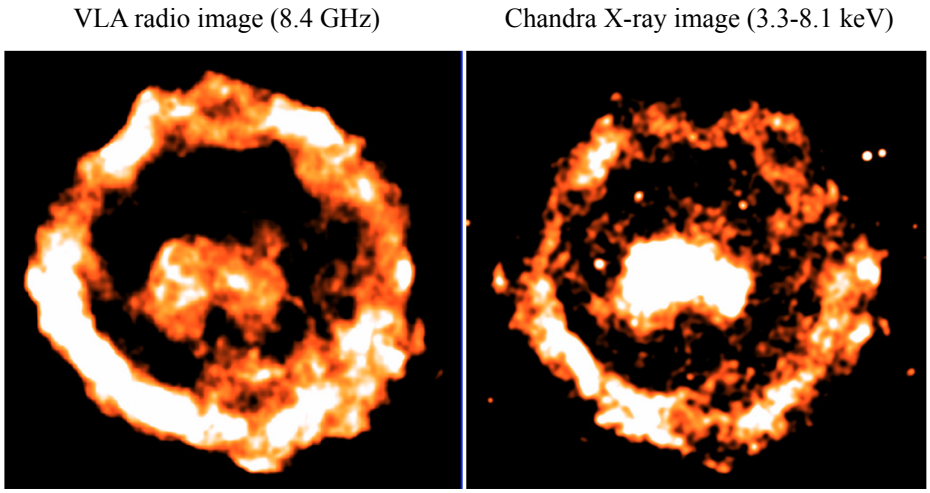

Figure 2.9: X-ray and radio images of the composite SNR, G11.2-0.3 (Borkowski et al., 2016). (right) X-ray image in the energy band of 3.3-8.1 keV with Chandra. (left) 8.4 GHz radio continuum image from with VLA.

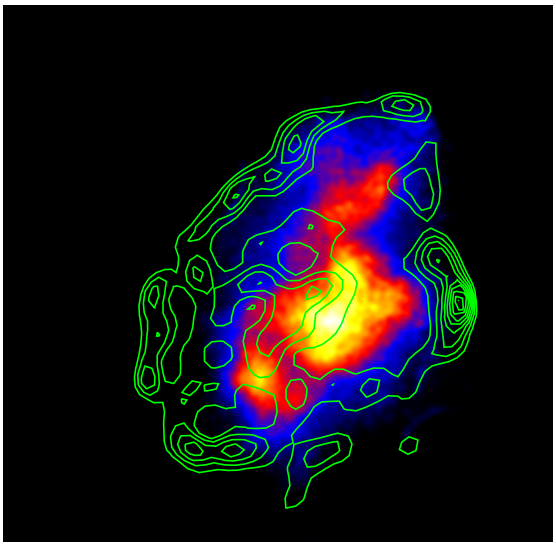

Figure 2.10: X-ray and radio images of the mixd-morphology SNR, W44. Suzaku X-ray image in the energy band of 0.3-10.0 keV with VLA 1.5 GHz radio contours.

Table 2.1: Classification of SNRs.

	Radio		X-ray	
	shell-like	center-filled	shell-like	center-filled
Shell-like SNRs	◯	×	◯	×
plerionic SNRs	×	◯ (PWN)	×	◯ (PWN)
Composite SNRs	◯	◯ (PWN)	◯	◯ (PWN)
Mixed-morphology SNRs	◯	×	×	◯

Chapter 3

Thermal X-ray Plasma in Supernova Remnants

3.1 Ionization State of Thermal Plasma

Thermal plasma is classified into three states based on relation between its electron temperature (kT_e) and ionization temperature (kT_z). The relation in each state is described as

(1) $kT_e > kT_z$; Ionization-dominant state,
(2) $kT_e = kT_z$; Collisional ionization equilibrium (CIE) state,
(3) $kT_e < kT_z$; Recombination-dominant state,

respectively. The ionization state of SNR plasmas changes during their evolution. The shock wave heating converts the translational motion into the thermal random motion (§2.2).

The temperature of the particle behind the shock wave increases in direct proportion to the product of its mass and the square of the shock velocity ($kT_{\rm i} \propto m_{\rm i} v_{\rm s}^2$). Since an ion mass is much larger than the electron mass (m_e), the ion temperature ($kT_{\rm i}$) and kT_e is non-equilibrium ($kT_{\rm i} \sim 2000 kT_e$). Then, the temperatures become equilibrium by the particle interaction with the timescale of the electron-electron and electron-proton interaction described as

$$\tau_{\rm ee} \sim 4.9 \times 10^8 \left(\frac{n_e}{1\ {\rm cm}^{-3}}\right)^{-1} \left(\frac{kT}{1\ {\rm keV}}\right)^{3/2} \left(\frac{\ln\Lambda}{30.9}\right) \quad {\rm s} \tag{3.1}$$

$$\tau_{\rm ep} \sim 3.1 \times 10^{11} \left(\frac{n_p}{1\ {\rm cm}^{-3}}\right)^{-1} \left(\frac{kT}{1\ {\rm keV}}\right)^{3/2} \left(\frac{\ln\Lambda}{30.9}\right) \quad {\rm s} \tag{3.2}$$

where $\ln\Lambda$ is the Coulomb logarithm (Zeldovich & Raizer, 1966).

Following Masai (1994), the timescale to reach an ionization equilibrium is calculated as

$$\tau_{\rm ion} = \sum_{Z}^{j=1} (n_e S_j)^{-1} = \left(\frac{n_e}{1\ {\rm cm}^{-3}}\right)^{-1} (\min(S_i))^{-1} \sim 10^{12} \left(\frac{n_e}{1\ {\rm cm}^{-3}}\right)^{-1} \quad {\rm s} \tag{3.3}$$

where S_Z is the ionization rate coefficient from the ion of Z. From comparison of these timescales, it is interpreted that the protons heated the electrons, and then the electrons ionize the ions.

We show ion fractions of O, Ne, Mg, Si, S and Fe in the CIE state as a function of kT_z in Figure 3.1. The fraction of highly ionized ions increases as the kT_z rises, and therefore, a weighted centroid-energy of emission lines becomes high. As shown in Figure 3.2, the fractions in non-equilibrium plasmas are significantly different with that in the CIE plasma.

In general, ages of old SNRs are comparable to the ionization timescale, so that their plasmas are in a CIE state. The plasmas in young and middle age SNRs are in a ionizing-dominant (underionized) state (called IP; ionizing plasma). However, in some SNRs, recombination-dominant plasmas (called RP; recombining plasma) are discovered (e.g., Kawasaki et al., 2002, 2005; Ozawa et al., 2009b; Yamaguchi et al., 2009). In order to realize the recombination-dominant state, special gas-environments around the SNR are required. We describe the formation process of the RPs in §3.3.

3.2 X-ray Emission from Thermal Plasmas

Here, we show mechanisms of thermal X-ray emissions, composing of continuum and line components, from SNR plasmas.

3.2.1 Continuum emission

The continuum emission from the SNR plasma consists of three components; bremsstrahlung, radiative recombination continuum (RRC), and two-photon emission due to free-free, free-bound, and bound-bound transitions of electrons, respectively.

Bremsstrahlung

When a free electron in the plasma is deflected by an ion, it decelerates and produces electromagnetic radiation called bremsstrahlung. The emissivity of the bremsstrahlung for a electron with the Maxwell-Boltzmann distribution is given by

$$\epsilon_{\rm ff} = \frac{32\pi e^6}{3m_e c^3}\left(\frac{2\pi}{3km_e}\right)^{1/2} T_e^{-1/2} Z_{\rm i}^2 n_e n_{\rm i} \exp\left(\frac{-E}{kT_e}\right) \overline{g_{\rm ff}} \tag{3.4}$$

$$= 6.8\times10^{-38}\ T_e^{-1/2} Z_{\rm i}^2 n_e n_{\rm i} \exp\left(\frac{-E}{kT_e}\right) \overline{g_{\rm ff}}\quad {\rm ergs}^{-1}\ {\rm cm}^{-3}\ {\rm Hz}^{-1}, \tag{3.5}$$

where e, c, k, m_e, Z, n_e, $n_{\rm i}$, E, and $\overline{g_{ff}}$ are the electron charge, light speed, Boltzmann constant, electron mass, atomic number, densities of electron and ion, emitted photon energy, and velocity averaged Gaunt factor (e.g., Rybicki & Lightman, 1979), respectively. For a typical thermal plasma emitting X-rays, the Gaunt factor is described as

$$\overline{g_{\rm ff}} = \left(\frac{3}{\pi}\frac{kT_e}{E}\right)^{1/2}, \tag{3.6}$$

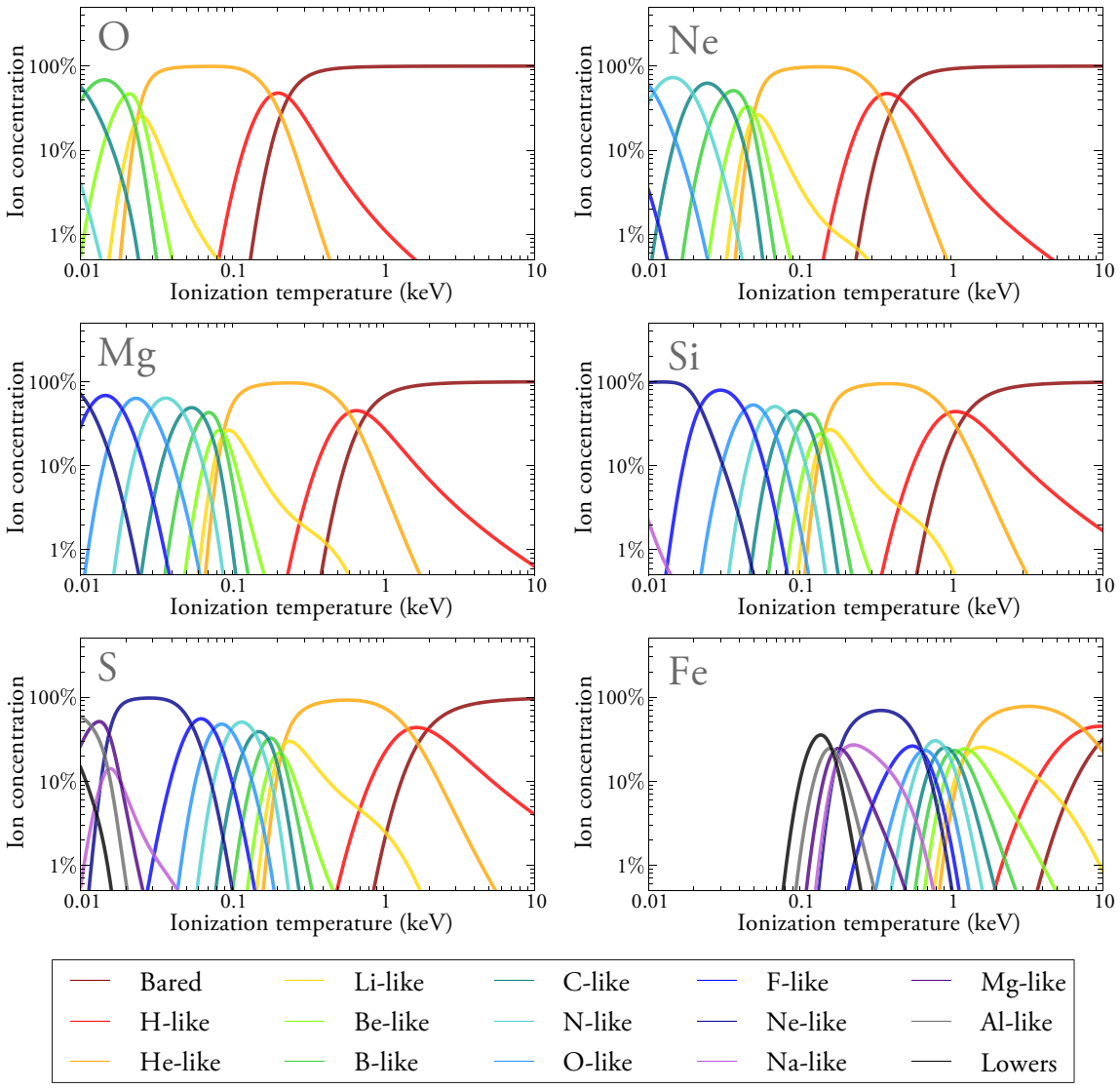

Figure 3.1: Ion populations as a function of the ionization temperatures for O, Ne, Mg, Si, S from Arnaud & Rothenflug (1985) and Fe from Arnaud & Raymond (1992). The figure is taken from Sawada (2011).

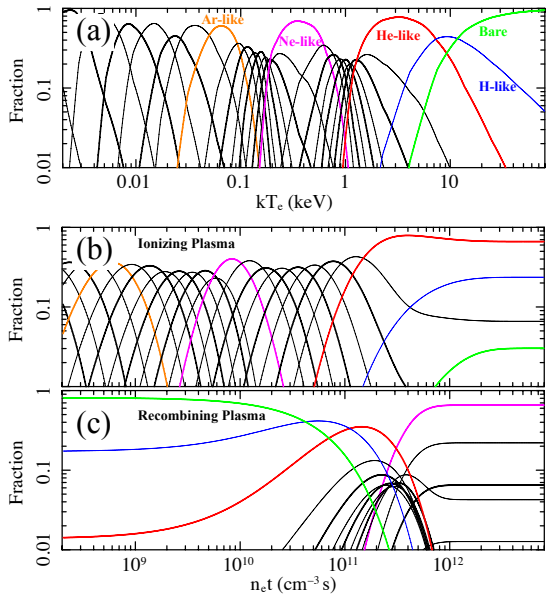

Figure 3.2: (a) Ion population of Fe in a CIE plasma as a function of the electron temperature kT_e. Orange, magenta, red, blue, and green lines represent Ar-like, Ne-like, He-like, H-like, and bare Fe, respectively. (b) Ion population of Fe in an $kT_e = 5$ keV ionizing plasma as a function of the ionization timescale $n_e t$. (c) Same as (b) but for recombining plasma where the initial and current electron temperatures are assumed to be 30 keV and 0.3 keV, respectively. The figure is taken from Smith et al. (2014).

and therefore, the spectral shape of the bremsstrahlung only depends on T_e. Equation 3.4 can be approximated for each relation between E and kT_e as

$$\epsilon_{\rm ff} \propto \begin{cases} E^0 & (E \ll kT_e) \\ E^{-0.4} & (E \lesssim kT_e) \\ \exp\left(-\frac{E}{kT_e}\right) & (E > kT_e). \end{cases} \tag{3.7}$$

Thus, the bremsstrahlung spectrum has the energy cut-off near $E \sim kT_e$ as shown in Figure 3.3, and we can measure T_e from the observed spectrum of hot plasmas.

Radiative recombination continuum

RRC is electromagnetic radiation emitted when a free electron recombines with an ion. Figure 3.4 shows an emission process of the RRC. The energy of emitted photon is the sum of the kinetic energy of the free electron and the binding energy of the recombined electron. The spectrum of the RRC has an energy edge depending on the binding energy of the recombined electron as shown in Figure 3.3. The emissivity of the RRC for electrons with the Maxwell-Boltzmann distribution is given by

$$\epsilon_{\rm bf} = 4 n_e n_{Z,j+1} E \left(\frac{E - E_{\rm edge}}{kT_e}\right) \sqrt{\frac{1}{2\pi m_e kT_e}}\ \sigma_n^{\rm rec}(E - E_{\rm edge})\ \exp\left(-\frac{E - E_{\rm edge}}{kT_e}\right), \tag{3.8}$$

where $n_{Z,j+1}$, $E_{\rm edge}$, and $\sigma_n^{\rm rec}$ are the density of the ion with the atomic number Z and the ionization state $j+1$, the binding energy of the recombined electron, and the recombination cross section to the level n, respectively.

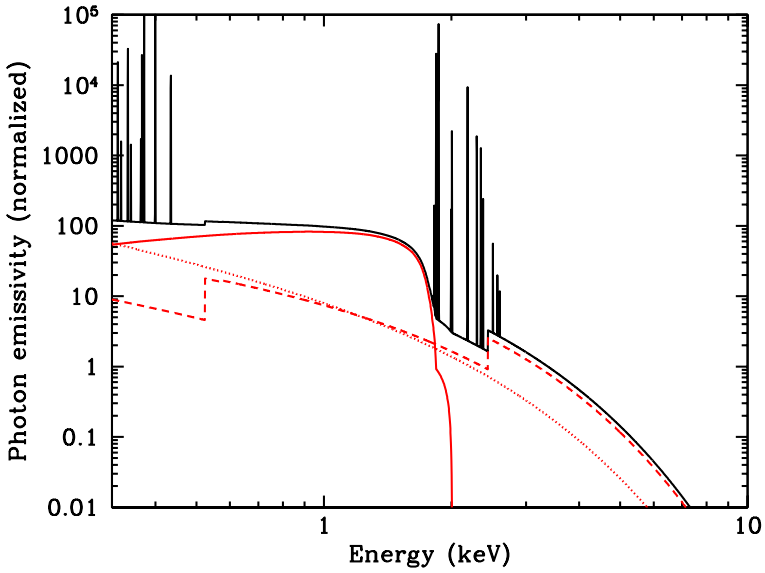

Figure 3.3: The emissivity of a pure silicon plasma in a recombined-dominant state (kT_e = 1 keV, $n_e t = 5 \times 10^{10}$ cm^{-3} s). Shown are the contributions of bremsstrahlung (red dotted line), radiative recombination continuum (red dashed line) and two-photon emission (red solid line). The figure is taken from Vink (2012).

When the electron temperature is much lower than the binding energy ($kT_e \ll E_{\rm edge}$), Equation 3.8 can be approximated as

$$\epsilon_{\rm bf} \propto \exp\Big(-\frac{E-E_{\rm edge}}{kT_e}\Big) \quad (E \geq E_{\rm edge}) \tag{3.9}$$

$$= 0 \quad (E < E_{\rm edge}). \tag{3.10}$$

In this dissertation, we denote the RRC emitted by the recombination of H-like ions to the ground state of He-like ions as "He-RRC", and call that of bare ions to the ground state of H-like ions "H-RRC". We summarize $E_{\rm edge}$ of He-RRC and H-RRC for heavy elements in Table 3.1.

Two-photon emission

When an electron is excited from $1s^2\ ^1S_0$ to $1s\,2s\ ^1S_0$ states by a free electron, the electron cannot transit directly from $1s\,2s\ ^1S_0$ to $1s^2\ ^1S_0$ because of a selection rule. In a low-density environment, second collision does not happen easily, and therefore, the electron transits while emitting two photons. Although the sum of the energy of the two photons is conserved, the energy of the each photon is not uniquely determined. Therefore, a spectrum of the two-photon emission is a continuum as shown in Figure 3.3.

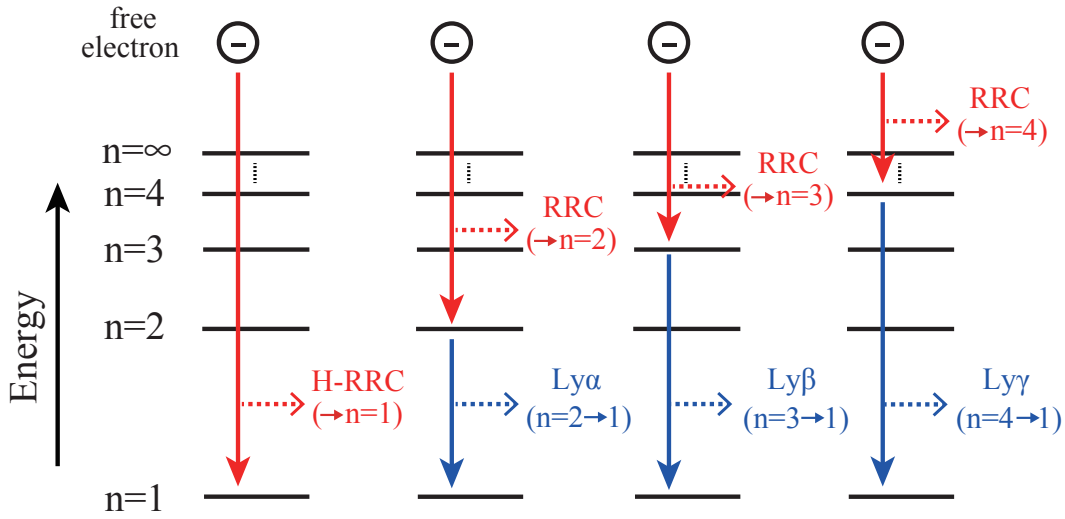

Figure 3.4: Schematic illustration of emission mechanism for radiation recombination continua (red arrows) and cascade lines (blue arrows).

Table 3.1: K-shell edge energies ($E_{\rm edge}$) of He-RRC and H-RRC. These values correspond to the K-shell binding potential of He-like and H-like ions, respectively.

Z	Element	$E_{\rm edge}$ (keV)	
		He-RRC	H-RRC
12	Mg	1.763	1.958
14	Si	2.439	2.666
16	S	3.225	3.482
18	Ar	4.121	4.406
20	Ca	5.128	5.440
26	Fe	8.830	9.194

3.2.2 Line emission

The line emission is due to bound-bound transitions with different energy levels for electrons. For a hydrogen atom, the energy of a photon is described as

$$E = R_y \left(\frac{1}{n^2} - \frac{1}{n'^2} \right), \tag{3.11}$$

where R_y, n, and n' are the Rydberg constant (13.6 eV), and the principal quantum number of before and after the transition, respectively. For heavy H-like elements with the atomic number of Z, that is given by

$$E \sim Z^2 R_y \left(\frac{1}{n^2} - \frac{1}{n'^2} \right). \tag{3.12}$$

The emission lines of H-like Kα ($2p \rightarrow 1s$), H-like Kβ ($3p \rightarrow 1s$), and H-like Kγ ($4p \rightarrow 1s$) are called Lyα, Lyβ, and Lyγ lines, respectively.

In the case of He-like ions, Kα emission are composed of resonance ($1s2p\ ^1\mathrm{P}_1 \rightarrow 1s^2\ ^1\mathrm{S}_0$), forbidden ($1s2s\ ^3\mathrm{S}_1 \rightarrow 1s^2\ ^1\mathrm{S}_0$), and inter-combination ($1s2p\ ^3\mathrm{P}_{2,1} \rightarrow 1s^2\ ^1\mathrm{S}_0$) transition lines (Figure 3.5). The emission lines of He-like Kα ($n = 2 \rightarrow 1$), He-like Kβ ($n = 3 \rightarrow 1$), and He-like Kγ ($n = 4 \rightarrow 1$) are called Heα, Heβ, and Heγ lines, respectively. We show centroid-energies of K-shell lines in Table 3.2.

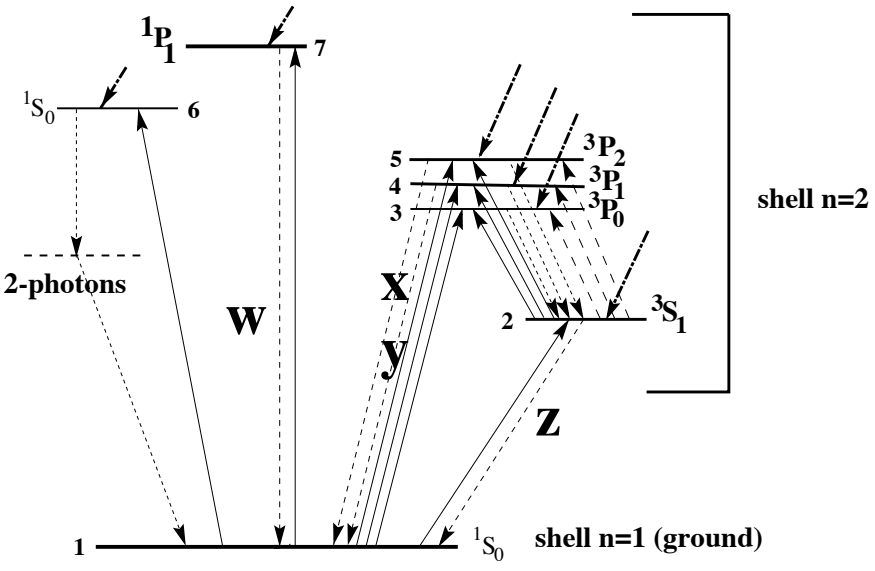

Figure 3.5: Level scheme for a He-like ion. Transitions of **w**, (**x**, **y**), and **z** indicate that of resonance, inter-combination, and forbidden lines, respectively. (Porquet et al., 2001)

As radiation processes with the bound-bound transitions in SNRs, the photoelectric effect and the collisional excitation are well known. However, in a recombination-dominant state, the dielectronic recombination and the cascade decay are not negligible.

Table 3.2: Centroid senergies (eV) of K-shell lines of H-like and He-like ions.

	Lyα	Lyβ	Lyγ		Heα		Heβ	Heγ
				res.*	frb.*	int.*		
O	654	775	817	574	561	569	665	698
Ne	1022	1211	1277	922	905	915	1072	1127
Mg	1472	1745	1840	1352	1330	1343	1579	1660
Si	2006	2377	2506	1865	1840	1854	2183	2294
S	2623	3107	3277	2461	2431	2447	2884	3033
Ar	3323	3936	4151	3140	3104	3124	3685	3875
Ca	4106	4864	5130	3908	3845	3892	4582	4819
Fe	6966	8266	8732	6702	6641	6670	7798	8217
Ni	8077	9590	10107	7806	7744	7766	9190	9680

*res., frb., and int. indicate resonance, forbidden, and inter-combination lines, respectively.

Dielectronic recombination

Dielectronic recombination is a radiative process when a free electron is captured and in the end a photon is emitted. When a free electron recombines with an ion, a core electron is subsequently excited. The electron returns to a lower level and emits a satellite line at a slightly lower energy than the normal transition. Figure 3.6 shows the emission mechanism for the dielectronic recombination.

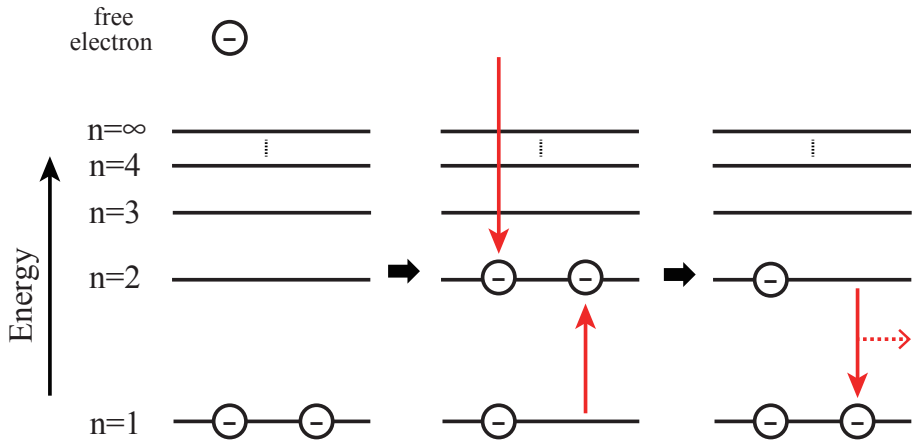

Figure 3.6: Schematic illustration of emission mechanism for the dielectronic recombination.

Cascade decay

Cascade decay is accompanied by the recombination of electrons into higher excited levels in the free-bound transitions (Figure 3.4). In plasmas with a recombination-dominant state, the intensity ratio of the cascade decay to the other normal transitions is higher than that in plasmas with a state of collisional ionization equilibrium.

3.3 Recombining Plasma in SNRs

3.3.1 Discovery of recombining plasma

Kawasaki et al. (2002) reported a first observation of RPs in SNRs. They analyzed ASCA data of the mixed-morphology SNR IC 443 and measured kT_z based on the H-like to He-like Kα intensity ratios of Si and S, and compared them with kT_e. They found that kT_z is significantly higher than kT_e, and suggested that the plasma is overionized. In the observations of IC 443 (Yamaguchi et al., 2009) and W49B (Ozawa et al., 2009b) with Suzaku, they discovered RRCs, which provides clear evidence that the plasmas are in an extremely recombining state. Subsequent Suzaku observations revealed RPs in other mixed-morphology SNRs in the Galaxy as well as in the Large Magellanic Cloud. We summarized the SNRs where RPs are clearly or possibly detected with Suzaku observations in Table 3.3.

3.3.2 Formation process of recombining plasma

The formation process of RPs has not been fully understood yet, but two scenarios are mainly discussed. One is the rarefaction scenario (Itoh & Masai, 1989). If a supernova explodes in a dense circumstellar matter (CSM) around the massive progenitor, ejecta and the CSM are shock-heated and quickly ionized because of the high density. When the shock breaks the CSM out to a lower density ISM, kT_e is decreased by adiabatic cooling. Kawasaki et al. (2002) proposed the other scenario, the thermal conduction scenario. If an SNR shock is interacting with a molecular cloud, thermal conduction occurs between the SNR plasma and the cloud, and, therefore, kT_e drops. Since the recombination timescales of ions are generally longer than the conduction timescales, kT_z cannot follow the decrease of kT_e, and RPs can be realized.

Both of the scenarios require special gas-environments around the remnants; a dense CSM and a molecular cloud for the rarefaction and thermal conduction scenarios, respectively. In order to investigate the origin of RPs, we need to obtain spatial distributions of physical parameters of the thermal plasmas (e.g., kT_e, $n_e t$) and to compare the parameters and the gas environments.

3.3.3 Toward the understanding of the origin of RPs

In order to understand the origin of RPs, we used Suzaku data of the Galactic SNRs G166.0+4.3, IC 443, W44 and W49B, and perform spatial resolved spectroscopy. These SNRs are known to have unique ambient gas through observations in the radio, infrared, X-ray and/or gamma-ray bands. In some of the remnants, the previous observations already reported the detection of RPs. The sizes of the SNRs allows us to divide the remnants into some regions by using the Suzaku telescope. The high sensitivity and the high energy resolution of Suzaku can detect RRCs of heavy elements and enable us to accurately determine the X-ray spectral features of the thermal plasma.

Table 3.3: List of the SNRs where RPs are clearly or possibly detected with Suzaku observations.

SNR	$kT_{\rm init}$ (keV)	kT_z (keV)	kT_e (keV)	$n_e t$ (10^{11} s cm^{-3})	Cloud Interaction	Reference
W49B	–	$2.46^{+0.08}_{-0.07}$	$1.52^{+0.01}_{-0.02}$	–	Yes	Ozawa et al. (2009b)
IC 443 (1)	–	~ 1.0(Si), ~ 1.2(S)	$0.61^{+0.03}_{-0.02}$	–	Yes	Yamaguchi et al. (2009)
IC 443 (2)	5 (fixed)	–	0.16–0.28 keV ($\rm RP_{cold}$)	3.8–15.1	Yes	Matsumura et al. (2017b)
〃	〃	–	0.48–0.67 keV ($\rm RP_{hot}$)	〃	〃	〃
G359.1-0.5	–	$0.77^{+0.09}_{-0.08}$	0.29 ± 0.02	–	Yes	Ohnishi et al. (2011)
W28	3 (fixed)	–	$0.40^{+0.02}_{-0.03}$	6.3	Yes	Sawada & Koyama (2012)
W44	1.00 ± 0.05	–	0.47 ± 0.01	$6.2^{+0.9}_{-0.4}$	Yes	Uchida et al. (2012)
G346.6-0.2	5 (fixed)	–	$0.30^{+0.03}_{-0.01}$	$4.8^{+0.1}_{-0.4}$	Yes	Yamauchi et al. (2013)
3C391 (1)	–	–	0.58 ± 0.01	–	Yes	Ergin et al. (2014)
3C391 (2)	$1.8^{+1.6}_{-0.6}$	–	$0.18^{+0.03}_{-0.05}$	$14.0^{+1.5}_{-2.2}$	Yes	Sato et al. (2014)
CTB 37A	5 (fixed)	–	$0.49^{+0.09}_{-0.06}$	$1.3^{+0.3}_{-0.1}$	Yes	Yamauchi et al. (2014)
G290.1-0.8	$1.7^{+1.2}_{-0.3}$	–	$0.45^{+0.02}_{-0.01}$	$12.2^{+1.3}_{-0.9}$	Possible	Kamitsukasa et al. (2015)
N49	11 ± 1	–	0.62 ± 0.01	9.8 ± 1.1	Yes	Uchida et al. (2015)
Kes 17	5 (fixed)	–	0.73 ± 0.03	$1.6^{+0.6}_{-0.3}$	Yes	Washino et al. (2016)
G166.0+4.3	3 (fixed)	–	0.46 ± 0.03	$6.1^{+0.5}_{-0.4}$	Possible	Matsumura et al. (2017a)
3C400.2	$3.15^{+0.02}_{-0.01}$	–	$0.71^{+0.03}_{-0.02}$	$1.8^{+0.2}_{-0.5}$	Possible	Ergin et al. (2017)

Chapter 4

Instruments

4.1 Suzaku Satellite

Suzaku is the fifth in a series of Japanese X-ray astronomy satellites devoted to observations of celestial X-ray sources (Mitsuda et al., 2007). It was launched by the Japan Aerospace Exploration Agency (JAXA) aboard an M-V launch vehicle from JAXA's Uchinoura Space Center on July 10, 2005. The spacecraft was put into a near-circular orbit at a $\sim$ 570 km altitude with an inclination angle of $\sim 31^\circ$ and an orbital period of $\sim$ 96 min. Figure 4.1a shows a schematic view of the Suzaku satellite in orbit. The length of the spacecraft is 6.5 m after the deployment of the extensible optical bench (EOB) and the total weight is 1706 kg. Suzaku had been operated for $\sim$ 10 yr, which exceeds its planned lifetime of $\sim$ 2 yr. Because of problems on its batteries and attitude control, the operation of Suzaku has been finished on June 1, 2015.

Suzaku carried two imaging detectors: the X-ray Imaging Spectrometer (XIS; Koyama et al., 2007) and the X-ray Spectrometer (XRS; Kelley et al., 2007) combined with the X-ray Telescopes (XRT; Serlemitsos et al., 2007) and a non-imaging hard X-ray detector: the Hard X-ray Detector (HXD; Kokubun et al., 2007; Takahashi et al., 2007). Figure 4.1b and Table 4.1 present a side view and the specifications of the instruments and the telescopes on Suzaku, respectively. The XIS consists of four cameras with X-ray charge-coupled devices (CCDs) named XIS0, 1, 2 and 3. The CCDs of XIS0, 2 and 3 are front-illuminated (FI) devices whereas that of XIS1 is a back-illuminated (BI) CCD. XIS2 and a part of XIS0 have not been functioning since November 2006 and June 2009, respectively (Suzaku XIS documents in 2007 and 2010). The HXD covers the bandpass of 10–600 keV. The XRS is the first micro-calorimeter system for X-ray astronomy but it failed to work after August 8, 2005 because of a liquid helium coolant loss. In this dissertation, we used data of the XIS so that we describe the details of the XRT and the XIS in the following sections.

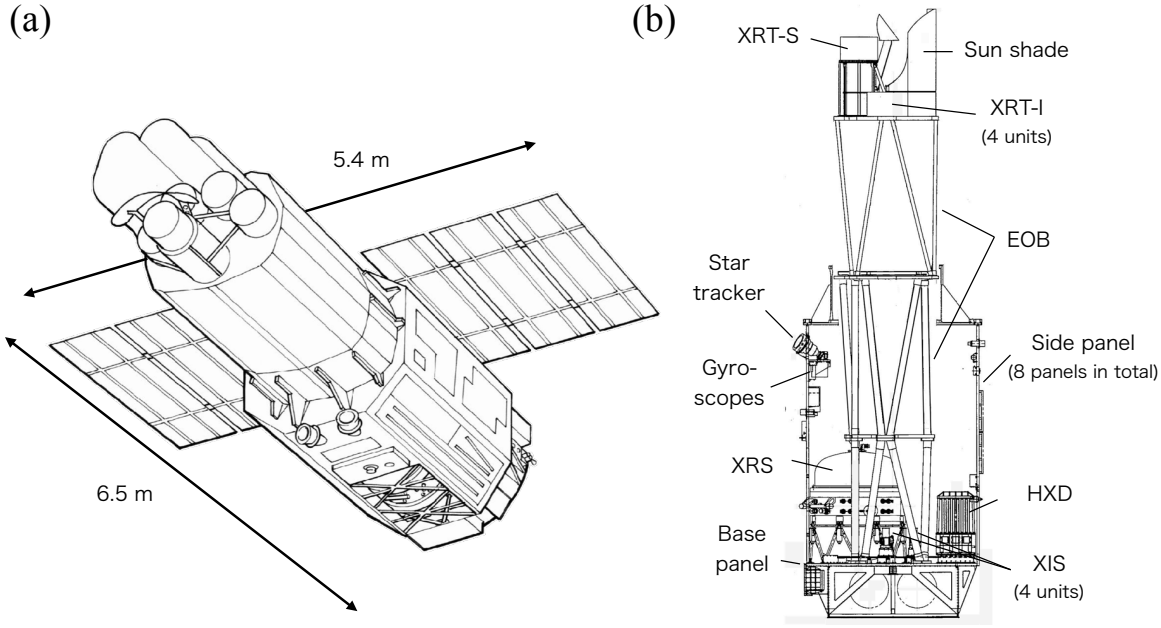

Figure 4.1: Schematic view of the Suzaku satellite (Mitsuda et al., 2007).

Table 4.1: Overview of Suzaku capabilities (Mitsuda et al., 2007).

XRT	Focal length	4.75 m
	Field of view	$17'$ at 1.5 keV, $13'$ at 8 keV
	Effective area	440 cm^2 at 1.5 keV, 250 cm^2 at 8 keV
	Angular resolution	$2'$ (Half power diameter)
XIS	Field of view	$17'.8 \times 17'.8$
	Bandpass	0.2–12 keV
	Pixel grid / size	1024×1024 / 24 μm $\times$ 24 μm
	Energy resolution	$\sim$ 130 eV FWHM at 6 keV
	Effective area	330 cm^2 (FI), 370 cm^2 (BI) at 1.5 keV
	(including the XRT)	160 cm^2 (FI), 110 cm^2 (BI) at 8 keV
HXD	Field of view	$4^\circ.5 \times 4^\circ.5$ ($\gtrsim$ 100 keV), $34' \times 34'$ ($\lesssim$ 100 keV)
	Bandpass	10–600 keV

4.2 X-ray Telescope (XRT)

4.2.1 Mechanism and design

The refractive index of, for instance, glass for X-rays is close to unity as opposed to a much larger value for visible light. Therefore, we cannot use the same focusing method as visible light to focus X-rays. The most common method to focus X-rays is using total external reflection. X-rays are reflected when the grazing incidence angle is shallow enough ($\lesssim 1^\circ$). In 1952, Wolter proposed the design composed of two-stage reflection mirrors in order to realize a wide filed-of view (FOV). The Wolter type I telescope is the most widely used for X-ray astronomy. It is composed of primary and secondary mirrors in parabolic and hyperbolic shapes, respectively (Figure 4.2).

Suzaku carried five Wolter type I telescopes. One is for the XRS (named XRT-S), and the others are for the XIS (named XRT-I). We hereafter refer to XRT-I simply as the XRT. The XRT contains in total 175 pairs of concentric thin-foil reflectors, whose thickness is 175 μm (Figure 4.3). The diameter and weight of the XRT are 399 mm and 19.3 kg, respectively. The total weight of the four modules of the XRT is only $\lesssim 80$ kg which is smaller than those of mirrors aboard other X-ray astronomy satellites such as Chandra (~ 950 kg) and XMM-Newton (~ 1300 kg).

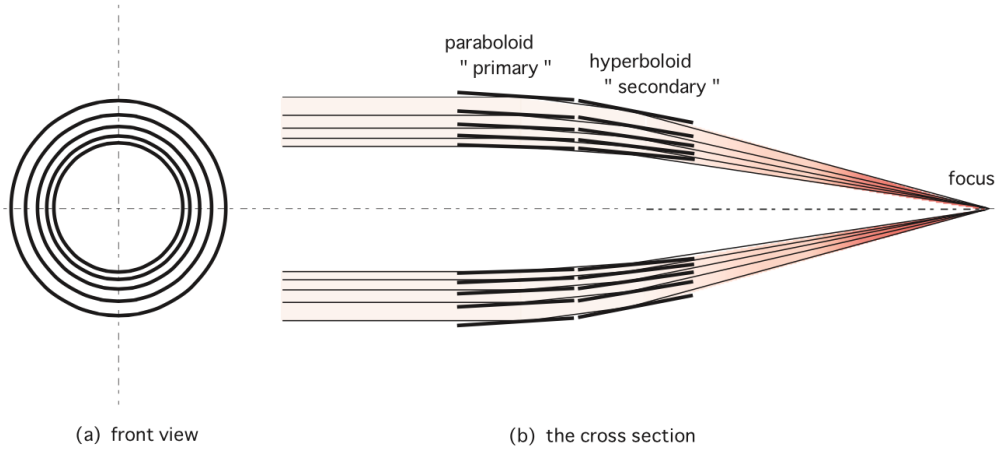

Figure 4.2: Schematic view of the XRT composed of nested reflectors: (a) front view; (b) cross section including the optical axis (Mori et al., 2005).

4.2.2 Performance

In spite of its light weight, the XRT has a large effective area, 450 cm^2 at 1.5 keV and 250 cm^2 at 7 keV, which is comparable to those of the mirrors aboard XMM-Newton (Figure 4.4a). However, the XRT trades off the spatial resolution. In order to evaluate the spatial resolution, we commonly use a half power diameter (HPD), which is defined as a diameter within which 50% of focused X-rays from a point source are enclosed. The HPDs of the XRT are $1'.8$–$2'.3$ (see Figure 4.4b), which is about one order of magnitude larger than those of Chandra and XMM-Newton.

The effective area is a function of the off-axis angle, which tends to decrease toward the off-axis. This effect is called “vignetting”. The vignetting effect is more evident in higher

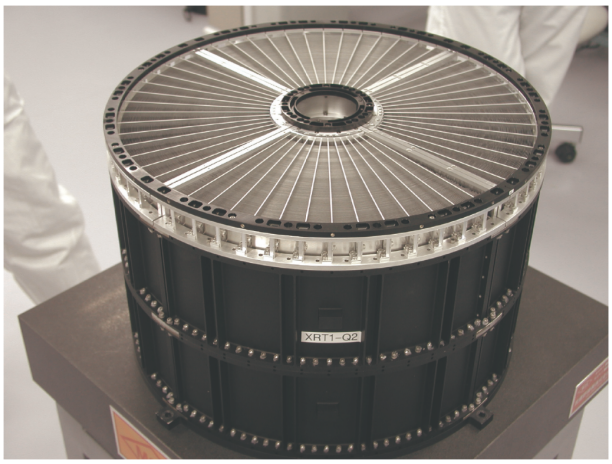

Figure 4.3: Photograph of the XRT (Serlemitsos et al., 2007).

energies because the critical angle for total external reflection is in inverse proportion to the X-ray energy. Figure 4.5 shows the vignetting curves of the XRT in the 3–6 keV and 8–10 keV bands.

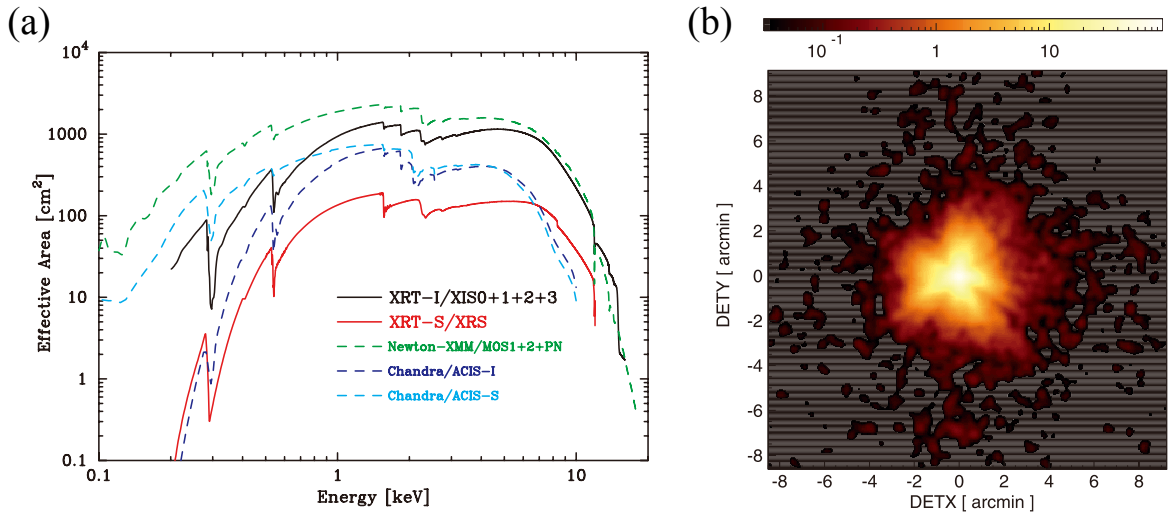

Figure 4.4: (a) Total effective area of the four XRT-I modules with those of XMM-Newton and Chandra. Transmissions of the thermal shield and the optical blocking filter, and the quantum efficiency of the CCD are all taken into account. (b) XIS0 image of a bright point source, SS Cygni. The figures are taken from Serlemitsos et al. (2007)

4.3 X-ray Imaging Spectrometer (XIS)

4.3.1 Overview of the XIS

Figure 4.6 shows a photograph and a side view of a XIS module. The pixel structure of the CCDs is classified as a MOS type which consists three layers; Metal, Oxide, and Semiconductor. The CCD chips have layers of poly-silicon, silicon-dioxide and p-type

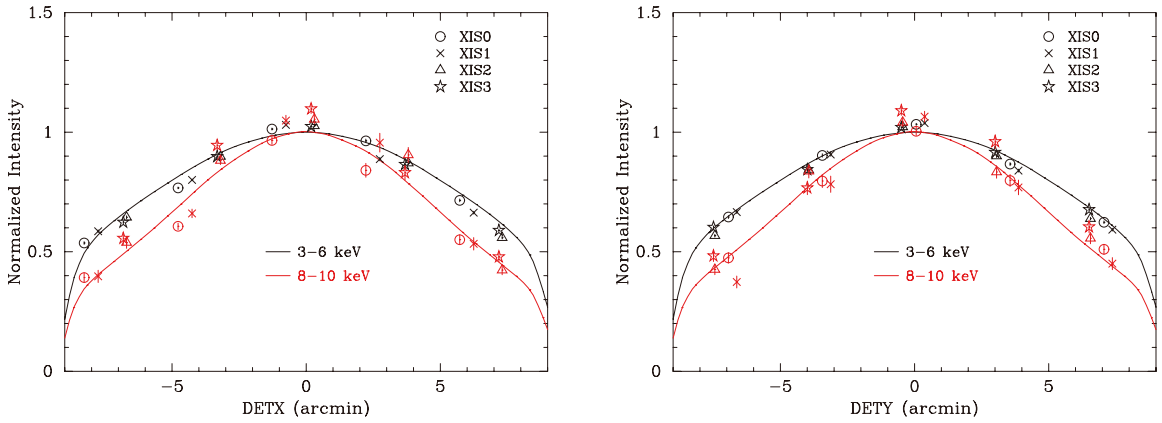

Figure 4.5: Vignetting curves of the XRT. The data points are obtained from observations of the Crab nebula. The model curves are calculated with a ray-tracing simulator with spectral parameters of the Crab nebula. The figures are taken from Serlemitsos et al. (2007).

silicon, which function as a MOS-junction. Each CCD has four segments (A, B, C, and D) consisting of an imaging area, a frame-store region and a readout node (Figure 4.7). The imaging area has 1024×1024 pixels with a pixel size of 24 μm $\times$ 24 μm. Combined with the XRT, the imaging area covers the $17'.8 \times 17'.8$ region in the sky. When an X-ray photon is absorbed in the depletion layer of the CCD, electron-hole pairs are produced in proportion to the X-ray energy. Generated charge is transferred from the imaging area to the frame-store region after an exposure, and is read out from the node.

In the FI CCDs, incident X-rays are attenuated by the 0.7 μm thick gate structure so that quantum efficiency (QE) on the low-energy side is lower. On the other hand, the BI CCD gains high QE in the low-energy band because of its thin dead layer, $\sim$ 10 nm (Figure 4.8). In the high energy band above $\sim$ 4 keV, the QE of XIS0 is higher than that of XIS1 because of the thicker depletion layer ($\sim$ 76 μm for the FI CCDs and $\sim$ 42 μm for the BI CCD). In the case of the BI CCD, X-ray photons are incident from the opposite side of the electrode so that we need to fully deplete it. It is difficult to process a thick full-depletion layer.

4.3.2 Calibration; charge transfer inefficiency

In orbit, CCDs suffer from radiation damage such as crystallographic defects in the depletion layer generated by cosmic rays. When signal charge is transferred to the readout nodes, a part of the charge is trapped in the crystallographic defects and is lost, which increases charge transfer inefficiency (CTI). The charge loss is a stochastic process so that the amount of the loss fluctuates and energy resolution also deteriorates (Nakajima et al., 2008; Ozawa et al., 2009a).

In order to reduce the CTI, we use a method of a spaced-raw charge injection (SCI) (Prigozhin et al., 2000; Bautz et al., 2004; LaMarr et al., 2004). Artificial charge is injected into given pixels from serial registers attached to the top of each column and fills the traps so that subsequent charge is transferred with less charge loss. Figure 4.9 shows a trend of centroid energy and width of the Mn Kα lines (5.895 keV) from the ^{55}Fe radioactive

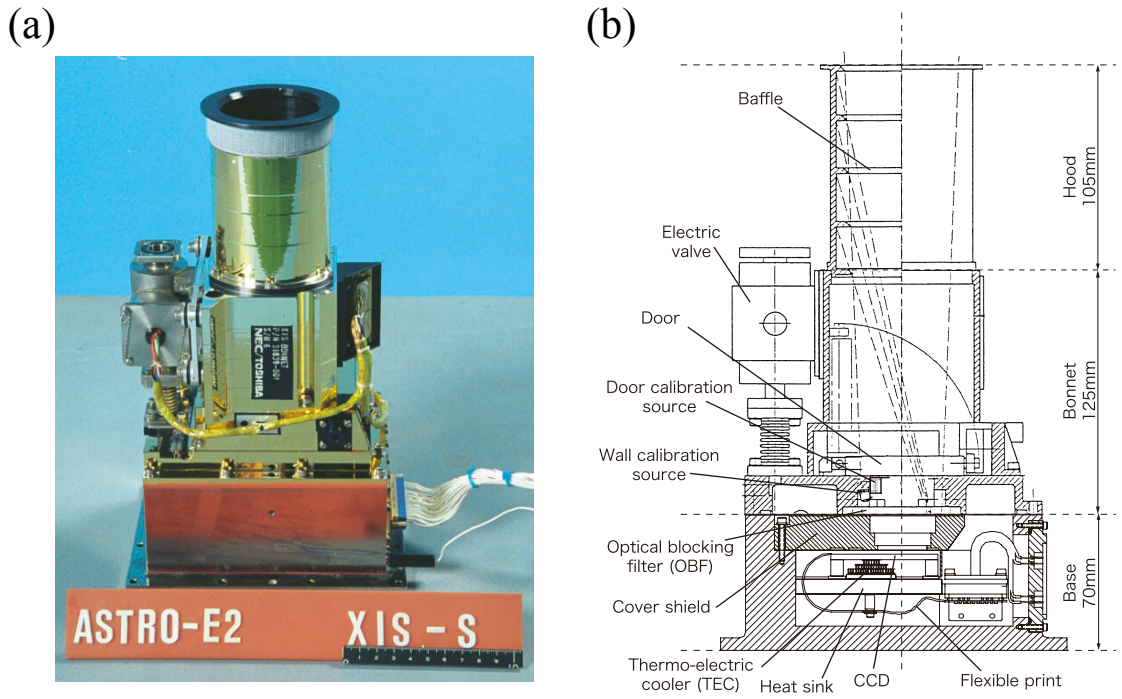

Figure 4.6: (a) Photograph and (b) side view of the XIS (Koyama et al., 2007).

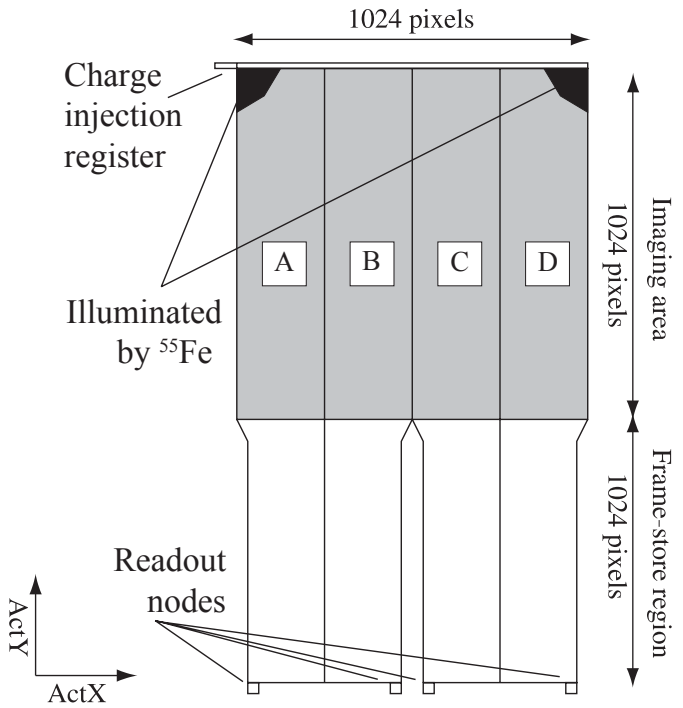

Figure 4.7: Schematic view of the XIS CCD (Koyama et al., 2007).

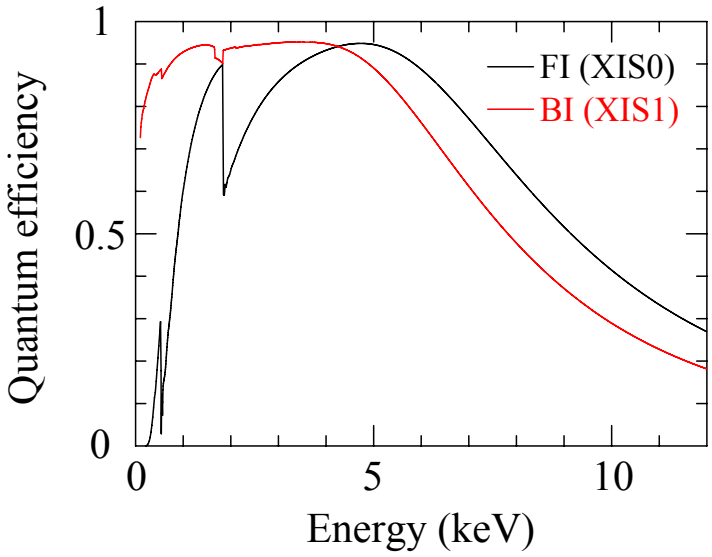

Figure 4.8: Quantum efficiency of the XIS0 (black) and the XIS1 (red) as a function of incident photon energy (Koyama et al., 2007).

sources equipped on two corners of each XIS (see Figure 4.7). The centroid energy of each sensor was decreasing from the launch to August 2006 and the width was increasing in this period. The XIS team for the first time performed the SCI in August 2006, and then, the centroid energy and the width were recovered. At the start of the SCI operations, the amount of the artificial charge was equal to the amount produced by 6 keV and 2 keV X-ray photons for the FI and BI CCDs, respectively. The CTI of XIS1 was more rapidly increasing as shown in Figure 4.9, and, therefore, the injected charge amount was changed from 2 keV to 6 keV in 2011.

The gain and the energy resolution of each sensor are improved by the SCI. However, the pulse height shows periodic variation because the SCI depends on the distance between the pixel of interest and the preceding charge injection row. Therefore, all the XIS data are calibrated with a method to correct the pulse height for the periodic variation (Uchiyama et al., 2009). Figures 4.10 and 4.11 show the trend of centroid energy and width of the the Mn Kα lines after the calibration, respectively. The uncertainty of the energy-scale determination is $\lesssim$ 20 eV (0.3%) for each sensor.

4.3.3 Calibration; gain

For gain calibrations of the XIS in the high energy band, Mn Kα and Kβ lines of the calibration source are used. For calibration in the low-energy band, the XIS team uses emission lines of O Lyα (0.654 keV), Ne Heα (0.921 keV), Ne Lyα (1.021 keV) and Mg Heα (1.352 keV) from the bright SNR E0102−72.3 (Figure 4.12). Figure 4.13 shows trends of centroid energies of the emission lines of XIS0. The gains of all the XIS sensors are calibrated $\lesssim$ 10 eV.

We describe below our own gain calibration method with an example of W49B. In analyses of thermal emission of SNRs, centroid energies of emission lines provide us with information of electron temperatures and degrees of ionization of the plasmas. The un-

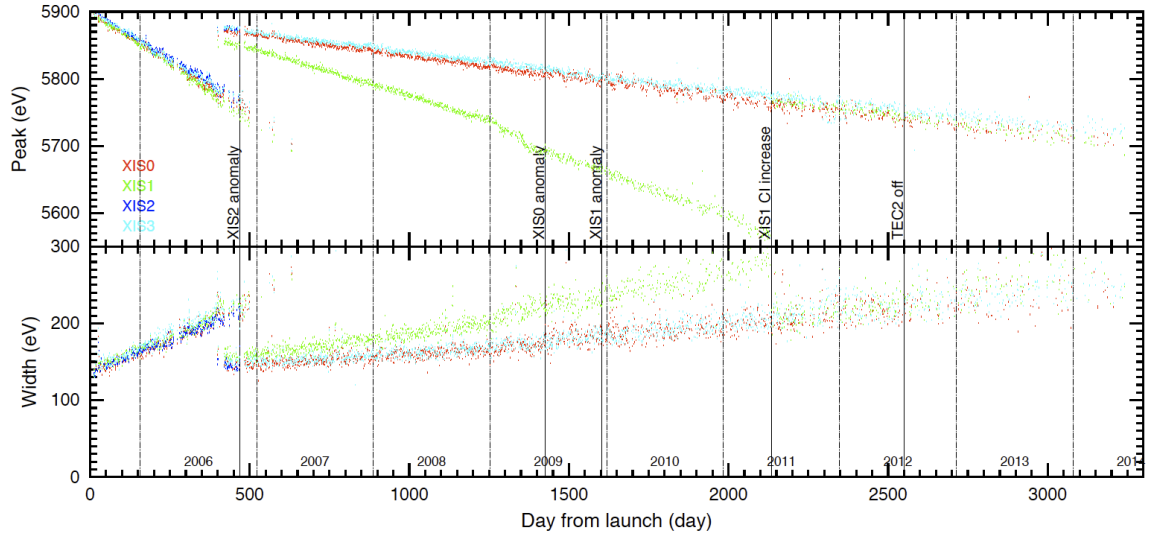

Figure 4.9: Trend of centroid energy (top panel) and width (bottom panel) of the Mn Kα lines for uncalibrated data of the XIS (Suzaku Technical Description).

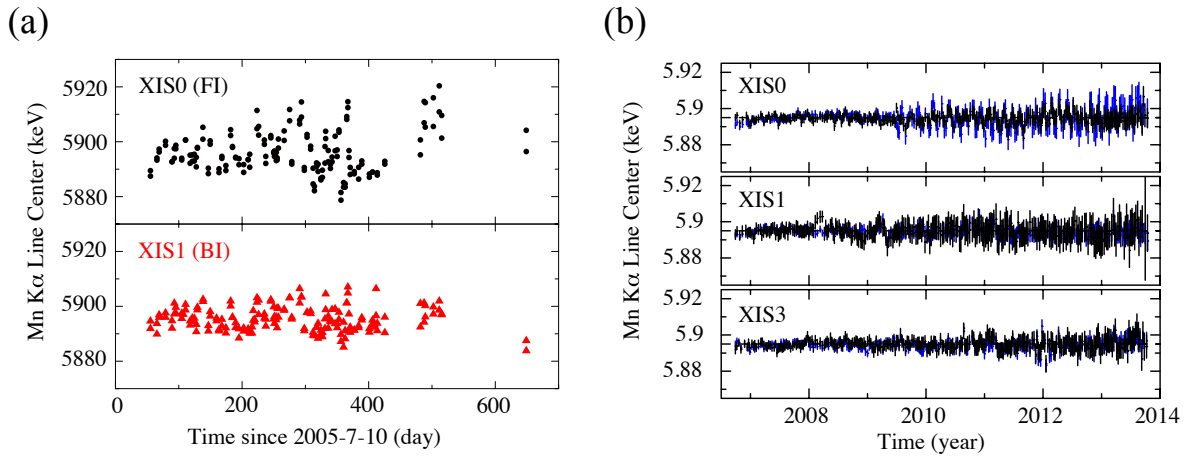

Figure 4.10: Trend of centroid energy of the Mn Kα lines for calibrated data of the XIS (a) before and (b) after turning on the charge injection technique. The black and blue points in panel (b) indicate the segment A and D data of each sensor, respectively (Suzaku Technical Description).

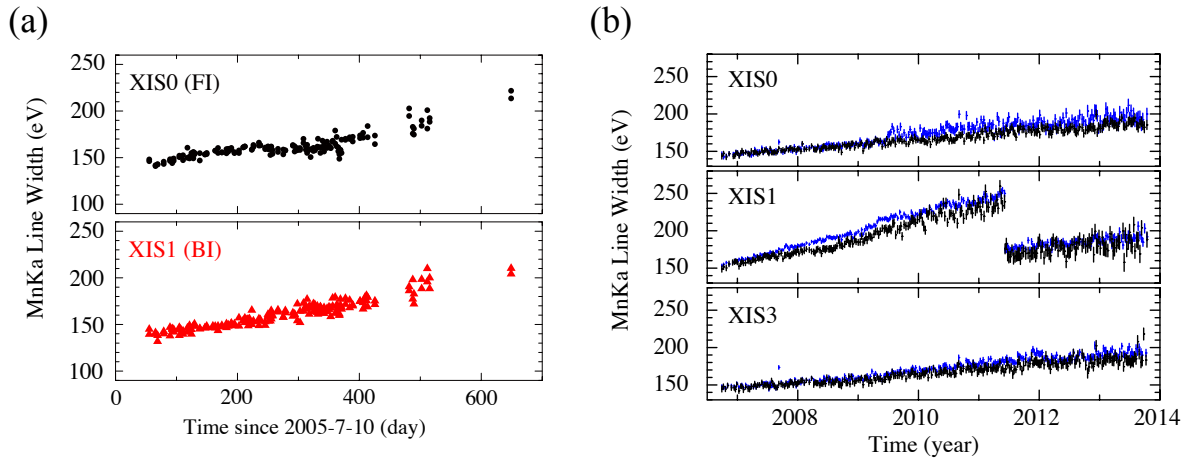

Figure 4.11: Trend of width of the Mn Kα lines for calibrated data of the XIS (a) before and (b) after turning on the charge injection technique. The black and blue points in panel (b) indicate the segment A and D data of each sensor, respectively (Suzaku Technical Description).

certainty of $\sim$ 10 eV significantly affects spectral fitting results. Therefore, we need a more accurate calibration than that performed by the XIS team.

For the gain collection, we used Lyα lines of Si (2.006 keV), S (2.628 keV), Ar (3.323 keV) and Ca (4.108 keV) from W49B and a Mn Kα line (5.895 keV) from the calibration sources. Heα lines were not used because centroid energies of lower ionized lines, such as Li-like and Be-like lines, are close to those of Heα lines, and intensity ratio of them depend on electron temperatures and ionization degrees of plasmas. We fitted narrow-band spectra in each energy band around the lines with a Gaussian and a power raw for the underlying continuum. We then obtained the relation between the true energies and the Gaussian centroids with linear regression (Figure 4.14). We corrected the gain using the relation. Figure 4.15 shows XIS0 spectra of the SNR W49B before and after the gain correction. The emission lines are moved toward the true values.

4.3.4 Data reduction; flickering pixels

Before analyzing XIS data, we must discard hot pixels and flickering pixels. The former always output pulse heights larger than the threshold for X-ray event detection, whereas the latter output large pulse heights intermittently. The number of these pixels increase in the orbit due to the radiation damage. Hot pixels are automatically identified and removed in orbit. On the other hand, it is difficult to remove flickering pixels in orbit, and thus, they are filtered out in the on-ground data reduction process.

In order to remove the flickering pixels, the XIS team provides maps of the flickering pixels called "noisy pixel maps" for each sensor (Figure 4.16). The XIS team defined the flickering pixels as those exceeding a threshold in a given period of time, and searched the pixels from 19 month data in the non X-ray background database. Ratios of the flickering pixels to the total are 1.5% (15594 pixels), 6.1% (64020 pixels), and $< 0.1\%$ (4139 pixels) in XIS0, 1, and 3, respectively. We show spectra of the SNR G166.0+4.3 before and after the filtering of the flickering pixels (Figure 4.17).

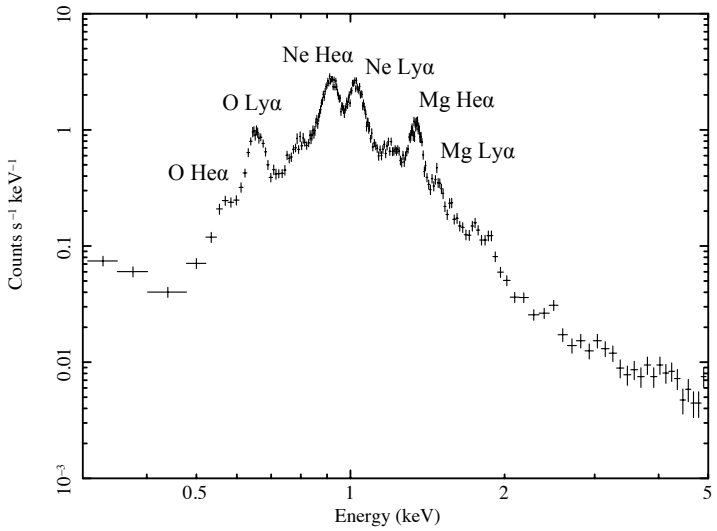

Figure 4.12: XIS0 Spectrum of the SNR E0102−72.3.

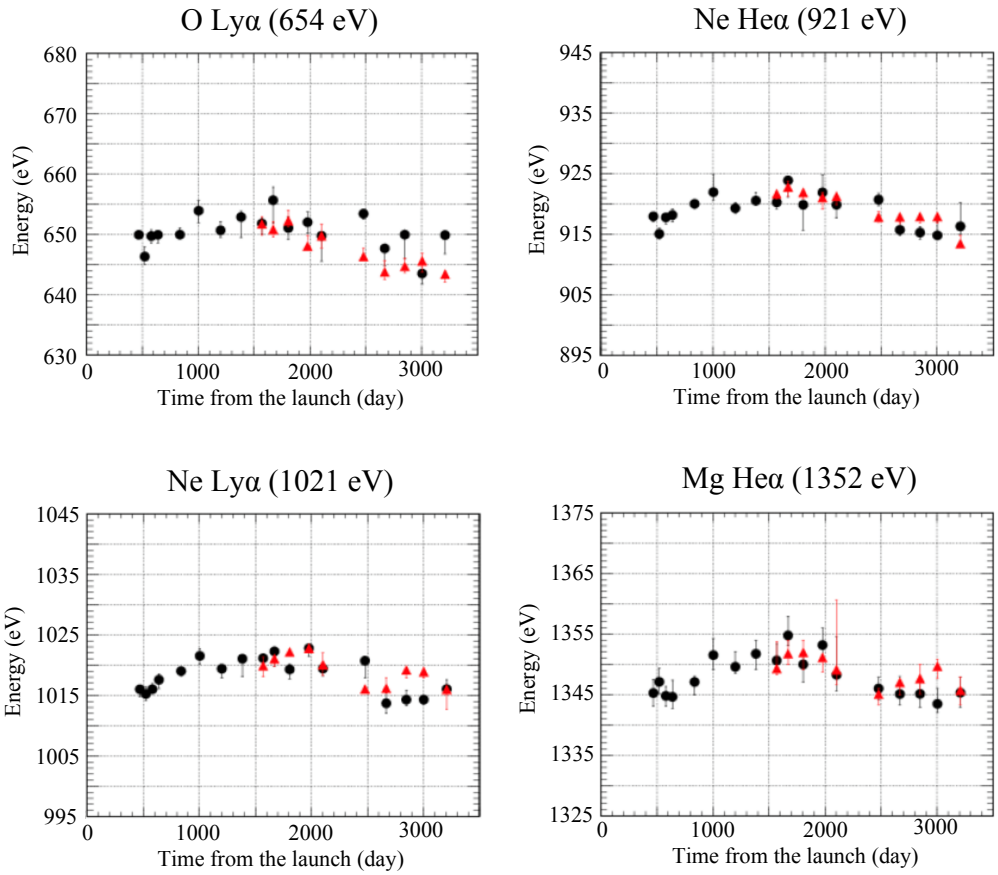

Figure 4.13: Trends of centroid energies of O Lyα, Ne Heα, Ne Lyα and Mg Heα of E0102−72.3 obtained with XIS0. The black and red points are data taken in readout modes with no option and with the 1/4 window option (for a bright source), respectively (Suzaku Technical Description).

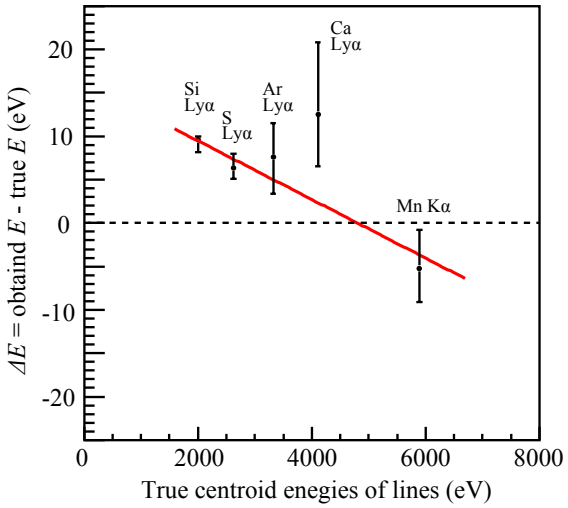

Figure 4.14: Comparison of centroid energies of emission lines from W49B before applying the calibration described in §4.3.3. The red line indicates a function estimated by linear regression.

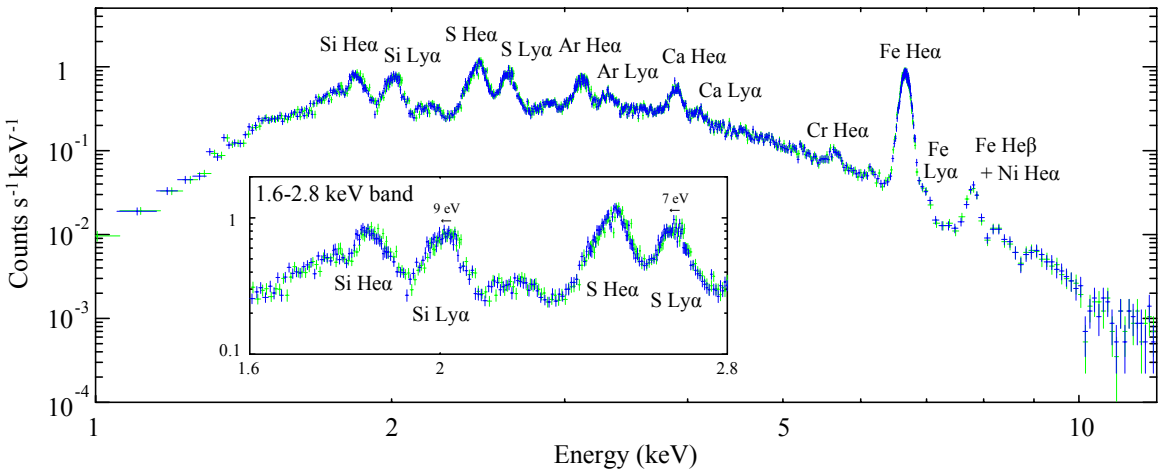

Figure 4.15: Green and Blue crosses show XIS0 spectra of the SNR W49B before and after the gain correction, respectively. Centroid energies of the Si and S Lyα lines shift 9 and 7 eV after the correction, respectively.

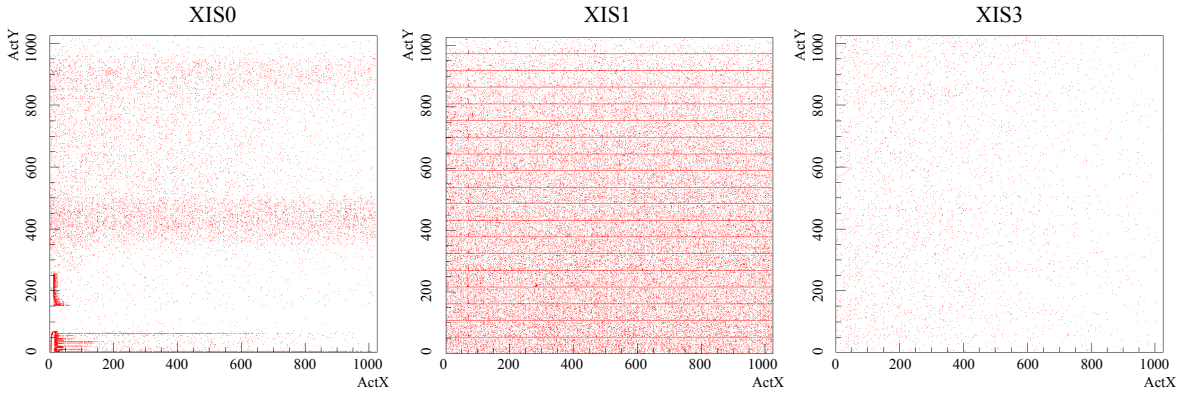

Figure 4.16: Maps of the flickering pixels provided in April 2016.

4.3.5 Non X-ray background (NXB)

In the orbit, high energy particles produce background signals, called non X-ray background (NXB). NXB spectra are obtained by observations pointing toward the Earth at night. Figure 4.18 shows the NXB spectra of XIS0 (FI CCD) and XIS1 (BI CCD). The NXB includes the fluorescence X-ray lines of Al Kα, Si Kα, Ni Kα and Kβ, and Au Lα, Lβ and Mα from materials of the spacecraft, and Mn Kα and Kβ from the ^{55}Fe calibration sources. One of the origin of the continuum emissions is Compton scattering of cosmic X-rays or X-rays produced by interactions between cosmic rays and the satellite structure. The other is an ionization of cosmic-ray electrons or secondary electrons produced by the interactions.

Figure 4.19 shows the NXB spectra obtained by CCDs on Chandra, XMM-Newton and Suzaku in other to compare their background levels. The XIS has lower background level in the energy band of 3–10 keV because of the lower altitude of the orbit of Suzaku.

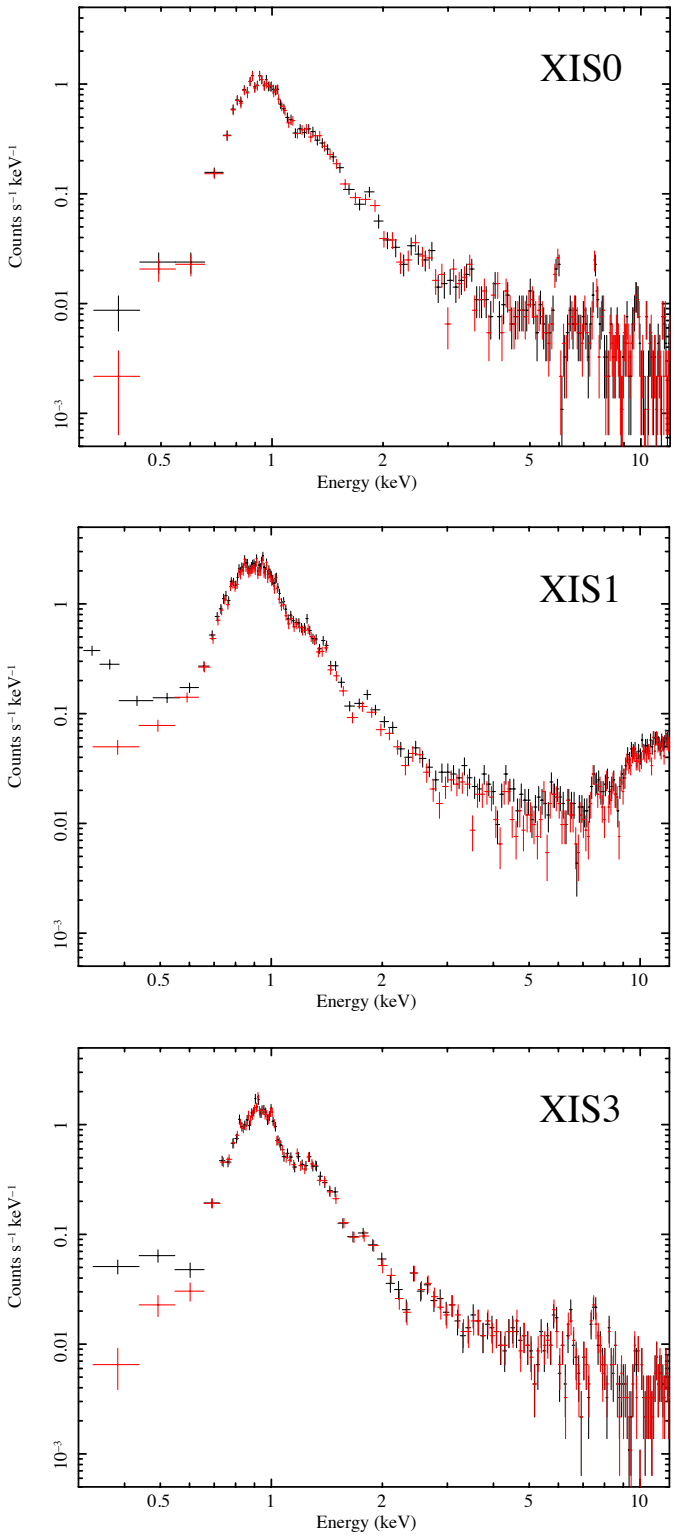

Figure 4.17: Spectra of each sensor in the northwest region of the SNR G166.0+4.3. Black and red crosses indicate the spectra before and after the reduction of the flickering pixels, respectively.

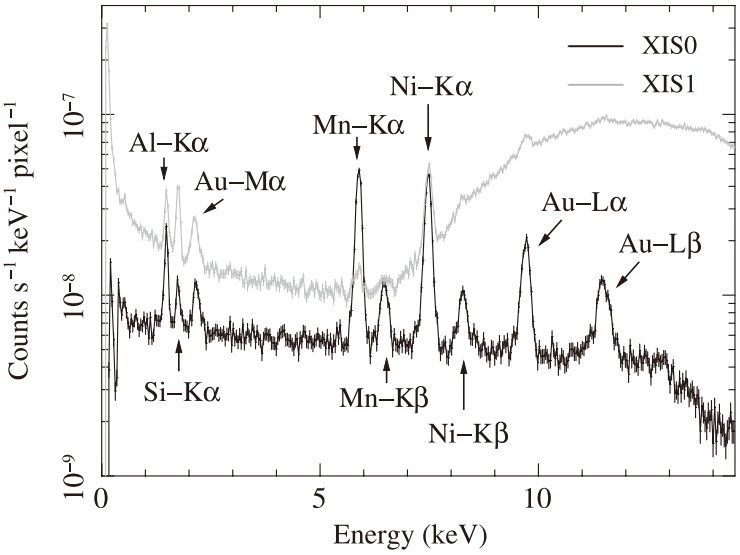

Figure 4.18: Spectra of the NXB in the XIS0 (black) and the XIS1 (gray) (Tawa et al., 2008).

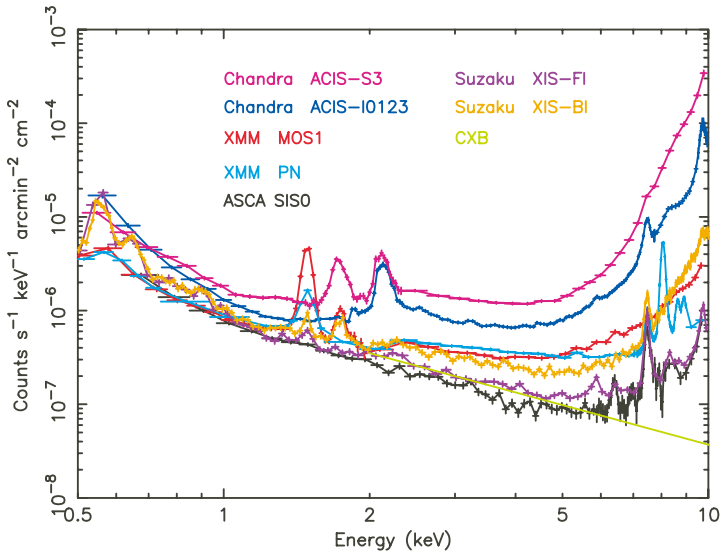

Figure 4.19: XIS background counting rate as a function of energy. The background rate was normalized with the effective area and the field of view, which is a good measure of the sensitivity determined by the background for spatially extended sources. The background rate of Chandra and XMM-Newton adopted from Katayama et al. (2004) are shown for comparisons. (Mitsuda et al., 2007)

Chapter 5

G166.0+4.3

5.1 Previous Works and Our Aims

G166.0+4.3 is a Galactic SNR whose radio shell has a large bipolar structure in the west with a smaller semicircle shell in the east (Sharpless, 1959; Landecker et al., 1982; Pineault et al., 1987). Landecker et al. (1982) estimated the distance to G166.0+4.3 as 5.0 ± 0.5 kpc by using the Σ-D-z (surface brightness-diameter-distance above the Galactic plane) relationship. Pineault et al. (1987) suggested that the gas density in the east is higher than that in the west because of the unusual morphology of the radio shell.

G166.0+4.3 was observed in the X-ray band with ROSAT (Burrows & Guo, 1994), ASCA (Guo & Burrows, 1997) and XMM-Newton (Bocchino et al., 2009). Burrows & Guo (1994) found that the X-ray morphology is distinct from the radio morphology and reproduced the spectrum with CIE models (Figure 5.1). They estimated the age of the remnant to be $\sim 2.4 \times 10^4$ yr by applying the evaporating cloudlet model (White & Long, 1991) and assuming the estimated distance of 5 kpc. Bocchino et al. (2009) classified G166.0+4.3 as an mixed-morphology SNR and reported that the spectra can be reproduced by an IP model.

The gas environment of G166.0+4.3 is clearly different between the east and the west, according to the morphology of the radio shell. It is one of the best sources for studying plasma evolution depending on the environment. In this Chapter, we report on observational results of G166.0+4.3 with Suzaku, which has high sensitivity and high energy resolution in the energy band of 0.3–12 keV. Throughout this chapter, errors are quoted at 90% confidence levels in the text and tables, and error bars in the figures indicate 1σ confidence intervals. We assume 5 kpc as the distance to the remnant. All spectral fits are performed with XSPEC version 12.9.0n. The plasma models are calculated with ATOMDB version 3.0.2. We used solar abundances given by Anders & Grevesse (1989).

5.2 Suzaku Observation and Data Reduction

We performed Suzaku observations of G166.0+4.3. Table 5.1 summarizes the observation log. In this analysis, we used data from the XIS installed on the focal planes of the XRT. XIS2 and a part of XIS0 are not used in what follows (see §4.3.1).

We reduced the data using the HEADAS software version 6.19. We used the calibration database released in 2015 October for data processing. The total exposure time of the five

observations is $\sim$ 226 ks after the standard data screening. In the processing of the XIS data, we removed cumulative flickering pixels by referring to the noisy pixel maps provided by the XIS team (§4.3.3). We also discarded pixels adjacent to the flickering pixels. NXBs were estimated by `xisnxbgen` (Tawa et al., 2008). The redistribution matrix files and the ancillary response files were produced by `xisrmfgen` and `xissimarfgen` (Ishisaki et al., 2007), respectively.

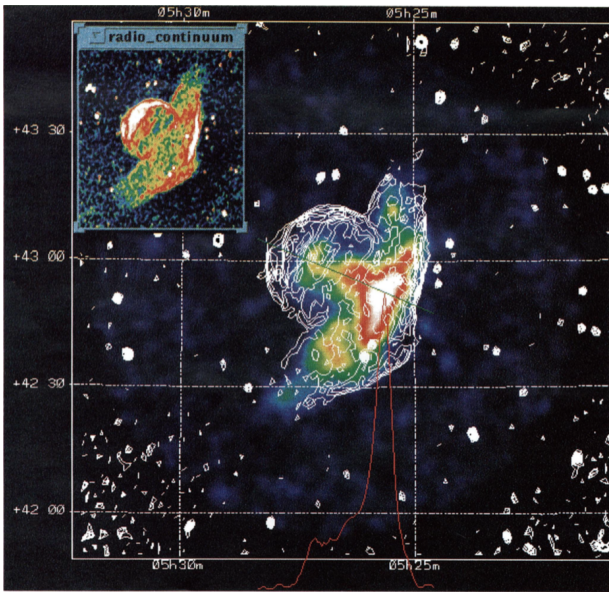

Figure 5.1: ROSAT image of G166.0+4.3 in the 0.52-2.02 keV band with 1.4 GHz radio contours (Burrows & Guo, 1994). The coordinates refer to the J2000.0 epoch. The red curve along the bottom of the image represents the X-ray intensity along the slice shown as a green line, which passes through the center of the SNR near its plane of symmetry. The inset in the upper left-hand corner is a color image of the radio continuum data, scaled from 0 to 1.67 K.

Table 5.1: Suzaku observation log of G166.0+4.3.

Target	Obs. ID	Obs. date	(R.A., Dec.)	Effective Exposure
G166.0+4.3 northeast	509022010	2014-09-19	($5^{\rm h}27^{\rm m}07^{\rm s}.7$, $42°58'52''.2$)	61 ks
G166.0+4.3 northeast	509022020	2014-09-22	($5^{\rm h}27^{\rm m}07^{\rm s}.7$, $42°58'52''.2$)	61 ks
G166.0+4.3 northwest	509023010	2014-09-20	($5^{\rm h}25^{\rm m}46^{\rm s}.8$, $42°54'01''.7$)	42 ks
G166.0+4.3 southeast	509024010	2014-09-21	($5^{\rm h}26^{\rm m}41^{\rm s}.2$, $42°39'06''.2$)	34 ks
G166.0+4.3 southeast	509024020	2015-03-13	($5^{\rm h}26^{\rm m}41^{\rm s}.2$, $42°39'06''.2$)	27 ks
IRAS 05262+4432 (Background)	703019010	2008-09-14	($5^{\rm h}29^{\rm m}56^{\rm s}.0$, $44°34'39''.2$)	82 ks

5.3 Analysis

5.3.1 Image

Figure 5.2 shows a mosaic image of G166.0+4.3 in the energy band of 0.5–2.0 keV. We subtracted the NXB from the image and corrected it for the vignetting effect of the XRT. The contours are a 325 MHz radio image from the Westerbord Northern Sky Survey (WENSS).

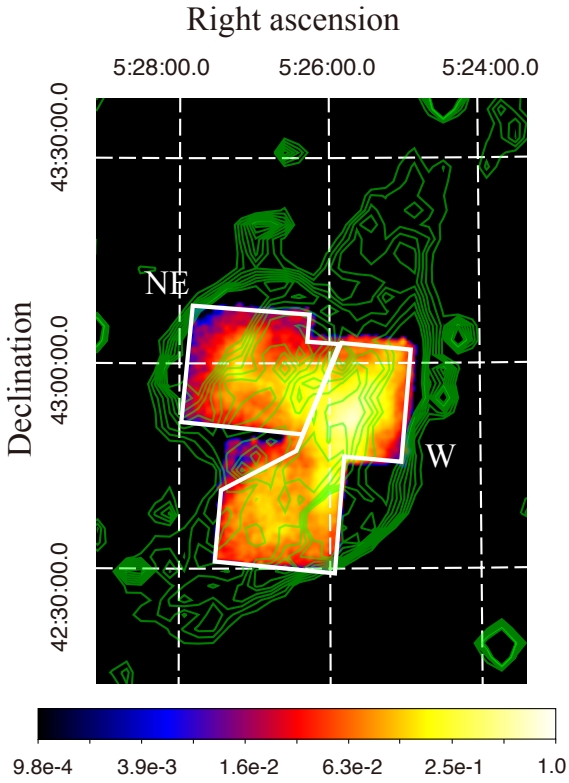

Figure 5.2: XIS image of G166.0+4.3 in the 0.5-2.0 keV band after the NXB subtraction and correction of the vignetting effect. The coordinates refer to the J2000.0 epoch. The X-ray count is normalized so that the peak becomes unity. We overlaid contours of the 325 MHz radio image from the WENSS.

5.3.2 X-ray background subtraction

For X-ray background estimation, we used Suzaku observational data of IRAS 05262+4432, which is located at $(l, b) = (165°.1, 5°.7)$. The observation log is shown in Table 5.1. We extracted a spectrum from a source-free region. In order to model the spectrum, we adopted a model by Masui et al. (2009). They observed the direction $(l, b) = (230°, 0°)$ with Suzaku in order to study the soft X-ray emission from the Galactic disk. Their model consists of four components: the cosmic X-ray background (CXB), the local hot bubble (LHB), and two thermal components for the Galactic halo (GH_{cold} and GH_{hot}).

We fit the X-ray background spectrum with the model after the NXB subtraction. We fixed the electron temperatures of the LHB, GH_{cold} and GH_{hot} at the values given

by Masui et al. (2009). The absorption column density ($N_{\rm H}$) of the CXB was fixed at 3.8×10^{21} cm^{-2}, the Galactic value in the line of sight toward IRAS 05262+4432 (Dickey & Lockman, 1990). The normalizations of all the components were allowed to vary. Figure 5.3 and Table 5.2 show the fitting result and the best-fit parameters, respectively.

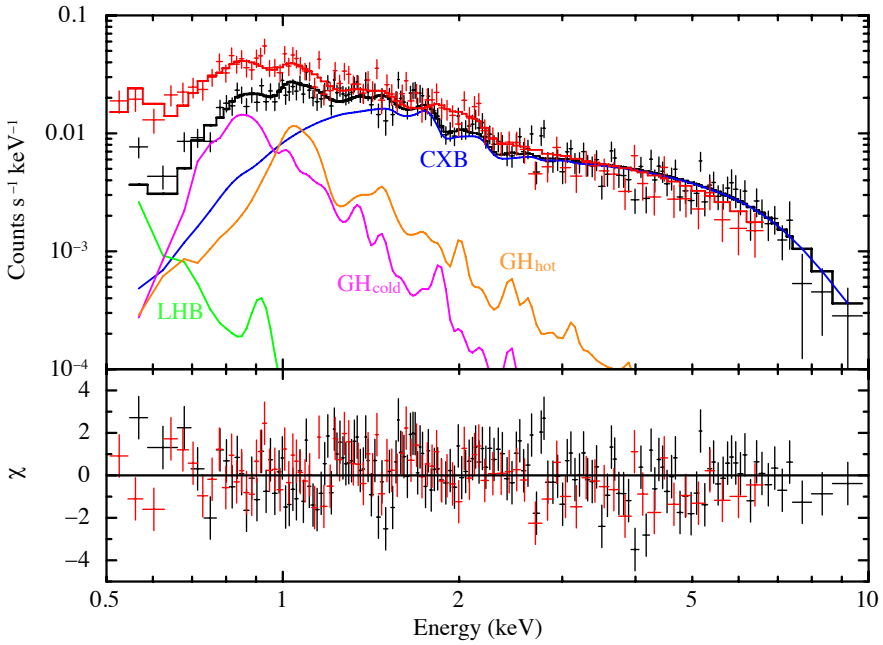

Figure 5.3: XIS0+3 (black crosses) and XIS1 (red crosses) spectra taken from the source-free region of the IRAS 05262+4432 data with the best-fit model. The solid lines show the model of XIS0+3. The blue, green, magenta and orange lines represent the CXB, LHB, GH$_{\rm cold}$ and GH$_{\rm hot}$ models, respectively. The bottom panel shows the data residuals from the best-fit model.

Table 5.2: Best-fit model parameters of the X-ray background spectra for G166.0+4.3.

Component	Model function	Parameter	Value
CXB	Wabs	$N_{\rm H}$ (10^{21}cm^{-2})	3.8 (fixed)
	Power law	Photon index	1.4 (fixed)
		Normalization*	10.7 ± 0.4
LHB	APEC	kT_e (keV)	0.105 (fixed)
		Normalization†	13.4 ± 3.2
GH$_{\rm cold}$	APEC	kT_e (keV)	0.658 (fixed)
		Normalization†	2.1 ± 0.2
GH$_{\rm hot}$	APEC	kT_e (keV)	1.50 (fixed)
		Normalization†	3.1 ± 0.5
		χ^2_ν (ν)	1.29 (234)

* The unit is photons s^{-1} cm^{-2} keV^{-1} sr^{-1} at 1 keV.
† The emission measure integrated over the line of sight, i.e., (1 / 4π) $\int n_e n_{\rm H} dl$ in units of 10^{14} cm^{-5} sr^{-1}.

5.3.3 SNR spectra

Considering the morphology of the radio shell, we extracted spectra from the northeast and west regions (named NE and W) indicated with the white solid lines in Figure 5.2. Figure 5.4 shows XIS0+3 spectra of W and NE after the NXB subtraction. One can clearly see Fe-L and Ni-L line complexes, and Si-K and S-K lines. The Fe-L and Ni-L line complexes are more prominent in W than those in NE.

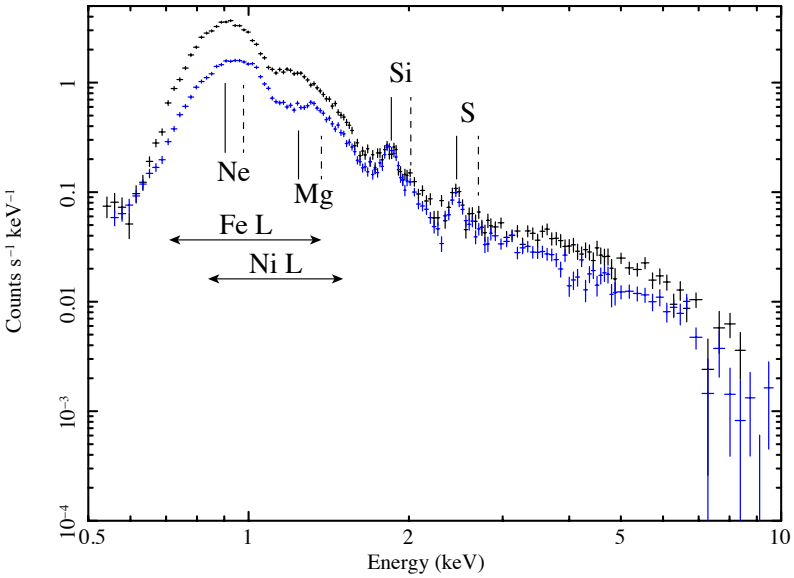

Figure 5.4: XIS0+3 spectra of the W (black) and NE (blue) regions. The vertical solid and dashed black lines show the center energies of the K lines from He-like and H-like ions, respectively. The arrows indicate the energy bands with Fe-L and Ni-L line complexes.

We fitted the spectra with the model consisting of the SNR component and the X-ray background (§5.3.2). The overall normalization of the X-ray background component was treated as a free parameter. The absorption column density of the CXB component was fixed at 3.6×10^{21} cm^{-2} which is the Galactic value in the line of sight toward G166.0+4.3.

We applied a one-component IP model to the W spectrum using the VVRNEI model in the XSPEC, which calculates the spectrum of a non-equilibrium ionization plasma after a rapid transition of the electron temperature from $kT_{\rm init}$ to kT_e. The initial temperature $kT_{\rm init}$ is fixed at 0.01 keV whereas the present electron temperature kT_e, ionization parameter n_et and normalization are free parameters. We used the Wisconsin absorption (Wabs) model (Morrison & McCammon, 1983) for the absorption, whose column density is a free parameter. The abundances of O, Ne, Mg, Si, S, and Fe are also free parameters. The Ar and Ca abundances are linked to S, and Ni is linked to Fe. The abundances of the other elements are fixed to the solar values. The energy band around the neutral Si K-edge (1.73–1.78 keV) is ignored because of the known calibration uncertainty. The fit left large residuals around 0.82 keV and 1.23 keV due to the lack of Fe-L lines in the model (e.g., Yamaguchi et al., 2011). Therefore, we added two narrow lines at 0.82 keV and 1.23 keV. The results are shown in Figure 5.6(w-i) and Table 5.3. We found that the spectrum is well reproduced by a one-component IP model with the electron temperature of 0.83 keV.

We applied the same IP model as W to the NE spectrum. Significant residuals are found at $\sim$ 2.0 keV and $\sim$ 2.6 keV which correspond to Si Lyα (2.0 keV) and the edge of the RRC of He-like Si (2.67 keV) + S Lyα (2.63 keV), respectively (Figure 5.6 (ne-i)). These spectral features, if confirmed, provide evidence that the plasma is in a recombination-dominant state. We tried a one-component RP model. However, a satisfactory fit was not obtained.

For a detailed investigation, we restricted the energy band to > 1.6 keV, where we found the large residuals, and tried one-component IP or RP models. The absorption column density is fixed to the best-fit value for W, $N_{\rm H} = 0.8 \times 10^{21}$ cm^{-2}, whereas kT_e and $n_e t$ are left free. The $kT_{\rm init}$ is a free parameter for the RP model, whereas it is fixed at 0.01 keV for the IP model. The abundances of Si and S are free parameters, and those of Ar and Ca are linked to S. The residuals were not improved with the IP model (Figure 5.6(ne-ii) and Table 5.3). On the other hand, we successfully fitted the spectrum with the RP model (Figure 5.6(ne-iii) and Table 5.3).

We extrapolated the above RP model down to 0.5 keV. Figure 5.6(ne-iv) shows the model and the full-band spectrum in the energy band of 0.5–10.0 keV. The spectral stru-

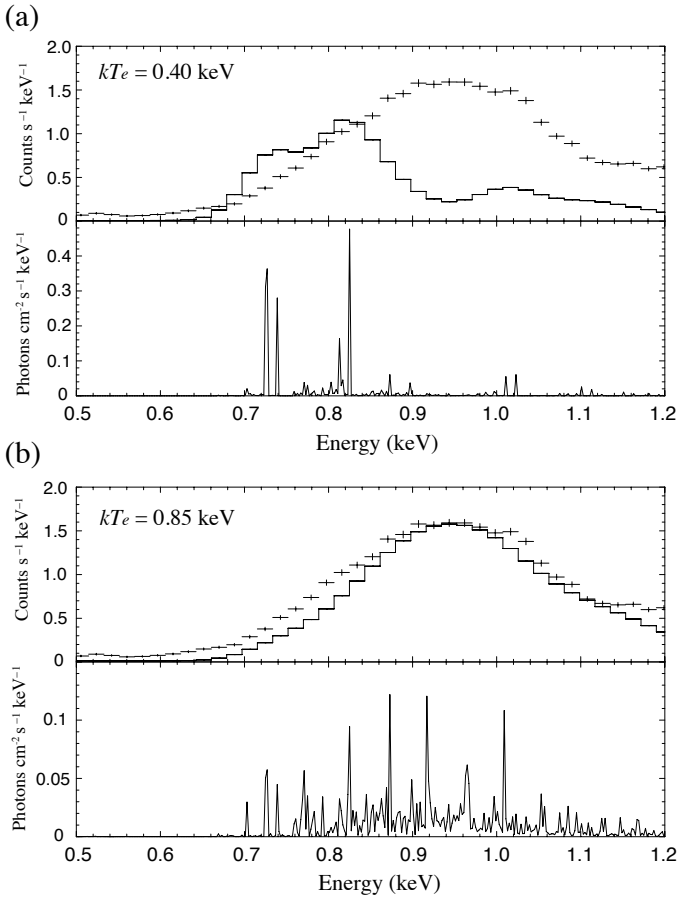

Figure 5.5: (a) NE spectrum of XIS0+3 (crosses) and the plasma model with (top) and without (bottom) response matrixes multiplied (solid lines) in the energy band of 0.5–1.2 keV. The plasma model consists only of Fe and Ni components with $N_{\rm H} = 1.7 \times 10^{21}$ cm^{-2}, $kT_e = 0.40$ keV, $kT_{\rm init} = 3.0$ keV and $n_e t = 6.0 \times 10^{11}$cm^{-3} s. (b) Same as (a) but with $kT_e = 0.85$ keV.

cture in the 0.7–1.1 keV band cannot be reproduced. With the electron temperature $kT_e = 0.37$ keV, the model predicts a peak energy of the Fe and Ni L line complexes at ~ 0.8 keV, which is significantly lower than the observed value of ~ 0.95 keV. Figure 5.5 shows the NE spectrum of XIS0+3 and the plasma model in the energy band of 0.5–1.2 keV. The model consists only of the Fe and Ni components with $N_{\rm H} = 1.7 \times 10^{21}$ cm^{-2}, $kT_{\rm init} = 3.0$ keV and $n_e t = 6.0 \times 10^{11}$ cm^{-3} s. The electron temperatures are 0.40 keV and 0.85 keV in Figures 5.5(a) and 5.5(b), respectively. The dominant emission lines of the Fe and Ni components are FeXVII 2p5 3s1→2p6 (0.725 keV and 0.739 keV) and FeXVII 2p5 3d1→2p6 (0.812 keV and 0.826 keV) with $kT_e = 0.40$ keV, and FeXIX 2p3 3s1→2p4 (0.822 keV), FeXVIII 2p4 3d1→2p5 (0.873 keV), FeXX 2p2 3d1→2p3 (0.965 keV) and FeXXI 2p1 3d1→2p2 (1.009 keV) with $kT_e = 0.85$ keV. The comparison between the data and the models indicates that the electron temperature of the Fe and Ni plasma should be ~ 0.85 keV in order to reproduce the observed structure. On the other hand, the Si and S plasma demands lower kT_e as we saw in the (ne-iii) fit.

The result indicates that the plasma has different kT_e between Fe (+Ni) and the other elements. Kamitsukasa et al. (2016) decomposed the ejecta of SNR G272.2−3.2 into components with different elements, considering that each element has different radial distributions. Following their idea, we adopted a two-component VVRNEI model: one for Fe and Ni, and the other for lighter elements. The spectra can be well fitted with the model comprising a CIE for Fe and Ni and an RP for the other elements. Figure 5.6(ne-v) shows the spectrum with the best-fit model. Although we tried IP and RP for the Fe and Ni component, the ionization parameter $n_e t$ cannot be constrained well. Therefore, we here assumed the CIE model for simplicity.

5.4 Discussion on G166.0+4.3

5.4.1 Spatial structure

The spectral analysis shows that the NE plasma contains two components; the low temperature RP component and the high temperature Fe-rich component. This suggests that the distributions of the two components are different from each other. In order to investigate the distribution, we made XIS images in the Si-K band (1.75–2.10 keV) and the Fe-L band (0.70–1.30 keV). We divided them by the corresponding underlying continuum image for which we selected the line-free band of 1.50–1.70 keV. We show the images in Figure 5.7, which indicates that Si distributes uniformly whereas the Fe distribution is more compact. In some SNRs, regardless of the type of the explosion, distributions of Fe are observed to be centered (e.g., Uchida et al., 2009; Hayato et al., 2010). The observed distributions are consistent with the widely believed picture of supernova nucleosynthesis that heavier elements tend to be produced closer to the center of the progenitor.

For a detailed analysis of the Fe distribution, we extracted spectra from the three regions (i)–(iii) in NE indicated by the white lines in the bottom panel of Figure 5.7. We fitted the spectra of each region with the same model as Figure 5.6(ne-v). We fixed kT_e of the RP component to the best-fit value, 0.46 keV. Figure 5.8 shows the resultant abundance ratios of Fe to Si. The ratio in the inner region is significantly higher and suggests the center-filled distribution of Fe.

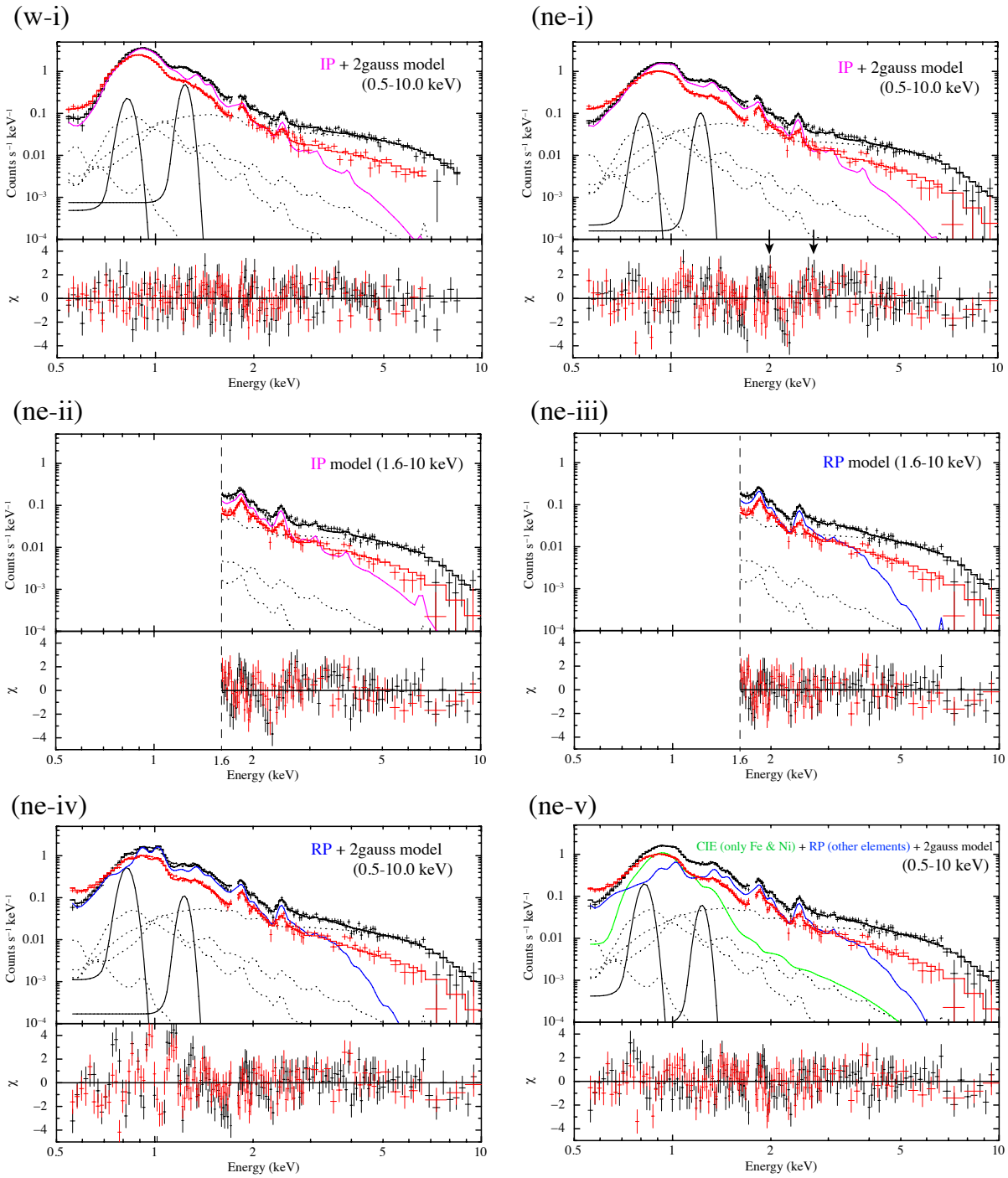

Figure 5.6: XIS0+3 (black crosses) and XIS1 (red crosses) spectra in the W and NE regions. Each spectrum is fitted with the model consisting of the SNR and background components. The solid and dotted lines show the SNR and background models of XIS0+3, respectively.

Table 5.3: Fit parameters of source regions.

Model function	Parameter	(w-i)	(ne-i)	(ne-ii)	(ne-iii)	(ne-v)
Wabs	$N_{\rm H}$ (10^{21}cm^{-2})	0.8 ± 0.1	0.3 ± 0.1	0.8 (fixed)	0.8 (fixed)	1.7 ± 0.1
VVRNEI1	kT_e (keV)	0.83 ± 0.01	$0.90^{+0.01}_{-0.02}$	$1.36^{+0.51}_{-0.27}$	0.37 ± 0.04	0.46 ± 0.03
	$kT_{\rm init}$ (keV)	0.01 (fixed)	0.01 (fixed)	0.01 (fixed)	≥ 2.98	3.0 (fixed)
	$Z_{\rm H}$ (solar)	1 (fixed)	1 (fixed)	1 (fixed)	1 (fixed)	1 (fixed)
	$Z_{\rm He}$ (solar)	1 (fixed)	1 (fixed)	1 (fixed)	1 (fixed)	1 (fixed)
	$Z_{\rm C}$ (solar)	1 (fixed)	1 (fixed)	1 (fixed)	1 (fixed)	1 (fixed)
	$Z_{\rm O}$ (solar)	$0.4^{+0.2}_{-0.1}$	$0.2^{+0.2}_{-0.1}$	1 (fixed)	1 (fixed)	$0.02^{+0.03}_{-0.01}$
	$Z_{\rm Ne}$ (solar)	$0.6^{+0.2}_{-0.1}$	$0.6^{+0.2}_{-0.1}$	1 (fixed)	1 (fixed)	0.4 ± 0.1
	$Z_{\rm Mg}$ (solar)	1.2 ± 0.2	0.6 ± 0.1	1 (fixed)	1 (fixed)	0.6 ± 0.1
	$Z_{\rm Si}$ (solar)	$0.7^{+0.1}_{-0.2}$	0.6 ± 0.1	$1.4^{+0.3}_{-0.1}$	2.3 ± 0.3	1.0 ± 0.1
	$Z_{\rm S} = Z_{\rm Ar} = Z_{\rm Ca}$ (solar)	1.2 ± 0.3	1.2 ± 0.2	1.8 ± 0.4	$3.3^{+0.7}_{-0.6}$	1.5 ± 0.2
	$Z_{\rm Fe} = Z_{\rm Ni}$ (solar)	1.2 ± 0.2	0.4 ± 0.1	1 (fixed)	1 (fixed)	0 (fixed)
	$n_e t$ (10^{11} cm^{-3}s)	$4.0^{+0.7}_{-0.5}$	3.1 ± 0.5	$1.6^{+1.7}_{-0.7}$	6.2 ± 0.6	$6.1^{+0.5}_{-0.4}$
	VEM (10^{57}cm^{-3})†	2.7 ± 0.2	$2.9^{+0.2}_{-0.3}$	$1.2^{+0.3}_{-0.2}$	$6.6^{+1.6}_{-1.3}$	$10.3^{+0.8}_{-1.0}$
VVRNEI2	kT_e (keV)	———	———	———	———	$0.87^{+0.02}_{-0.03}$
(only Fe & Ni comp.)	$kT_{\rm init}$ (keV)	———	———	———	———	$= kT_e$ (VVRNEI2)
	$Z_{\rm Fe} = Z_{\rm Ni}$ (solar)	———	———	———	———	0.14 ± 0.01
	$Z_{\rm others}$ (solar)	———	———	———	———	0 (fixed)
	$n_e t$ (10^{11} cm^{-3}s)	———	———	———	———	100 (fixed)
	VEM (10^{57}cm^{-3})†	———	———	———	———	$= VEM$ (VVRNEI1)
Gaussian	Centroid (keV)	0.82 (fixed)	0.82 (fixed)	———	———	0.82 (fixed)
	Normalization‡	$4.6^{+1.3}_{-0.7}$	$2.1^{+0.8}_{-0.7}$	———	———	$6.7^{+1.5}_{-1.3}$
Gaussian	Centroid (keV)	1.23 (fixed)	1.23 (fixed)	———	———	1.23 (fixed)
	Normalization‡	$3.4^{+1.3}_{-0.2}$	0.8 ± 0.1	———	———	0.7 ± 0.2
χ^2_ν (ν)		1.37 (247)	1.77 (251)	1.55 (150)	1.15 (150)	1.39 (250)

† Volume emission measure $VEM = \int n_e n_{\rm H} dV$, where n_e, $n_{\rm H}$, and V are the electron and hydrogen densities, and the emitting volume, respectively.

‡ The unit is photons s^{-1} cm^{-2} sr^{-1}.

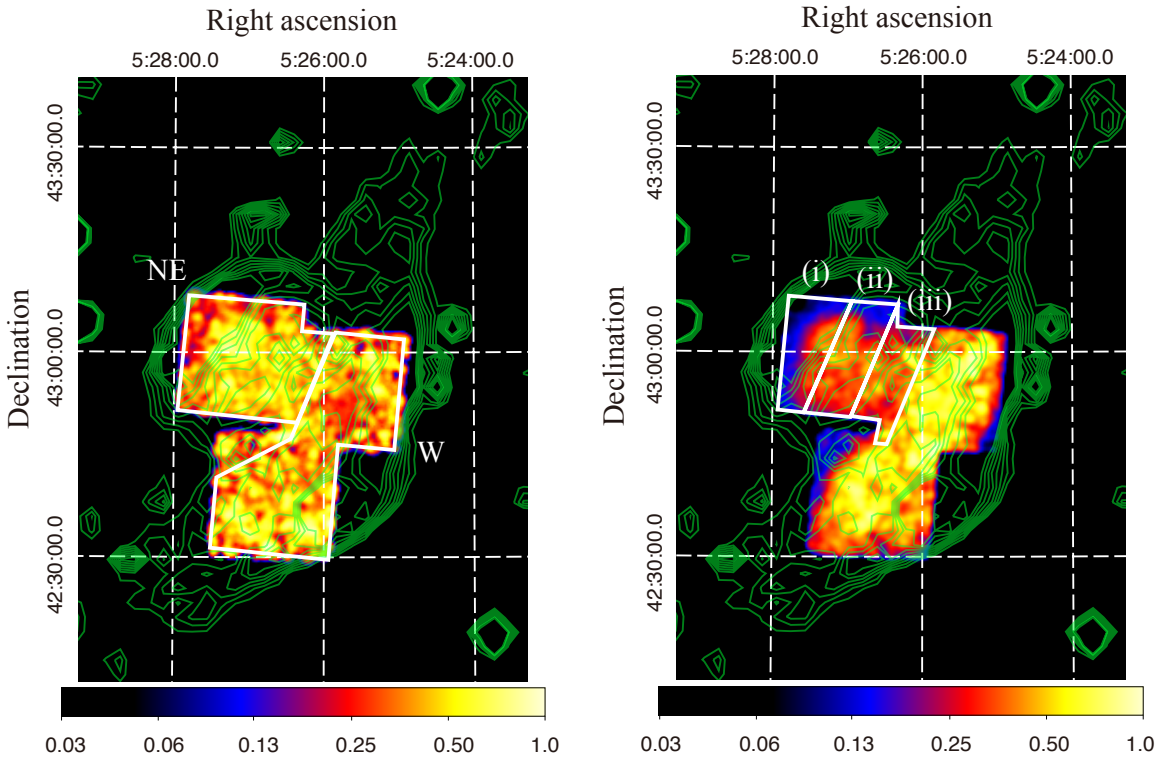

Figure 5.7: XIS images of G166.0+4.3 in 1.75–2.10 keV band (left: Si-K band) and the 0.70–1.30 keV band (right: Fe-L and Ni-L band) after subtraction of the NXB and correction of the vignetting effect. The images are divided by the corresponding underlying continuum image for which we selected the line-free band of 1.50–1.70 keV. The scale is normalized so that the peak becomes unity. The contours are a radio image of the WENSS at 325 MHz.

5.4.2 Ambient gas density and SNR age

In our spectral analysis, the volume emission measures are 2.7×10^{57} cm^{-3} and 1.0×10^{58} cm^{-3} in W and NE, respectively. The volumes are obtained to be 4.1×10^{59} f cm^3 and 1.8×10^{59} f cm^3 for the W and NE plasmas, respectively, where f is the filling factor, assuming the morphologies to be prisms whose bases are the W and NE regions and depths are 40 pc and 20 pc for W and NE, respectively. With the volume emission measures, we obtain the electron densities $n_{e,\mathrm{W}} = 0.1\ f^{-1/2}$ cm^{-3} and $n_{e,\mathrm{NE}} = 0.3\ f^{-1/2}$ cm^{-3} for W and NE, respectively. They suggest that the ambient gas is denser in NE than that in W. This is supported by the radio morphology, the smaller shell in the eastern side. Another clue of denser gas in NE is the GeV gamma-ray emission detected in the eastern part of the remnant by Fermi LAT observations (Figure 5.9: Araya, 2013). If π^0 decays are the main production process for the gamma rays, dense gas, which acts as targets for accelerated protons for π^0 production, would be in NE.

In the spectral analysis, we obtained $n_{e,\mathrm{W}}\ t = 4.0 \times 10^{11}$ cm^{-3} s and $n_{e,\mathrm{NE}}\ t = 6.1 \times 10^{11}$ cm^{-3} s for the W and NE plasmas, respectively. With $n_{e,\mathrm{W}}$ and $n_{e,\mathrm{NE}}$ calculated above based on the emission measures, the timescales are estimated to be $t = 1.4 \times 10^5\ f^{1/2}$ yr for W and $t = 7.1 \times 10^4\ f^{1/2}$ yr for NE. The ionization timescale for the W plasma, which

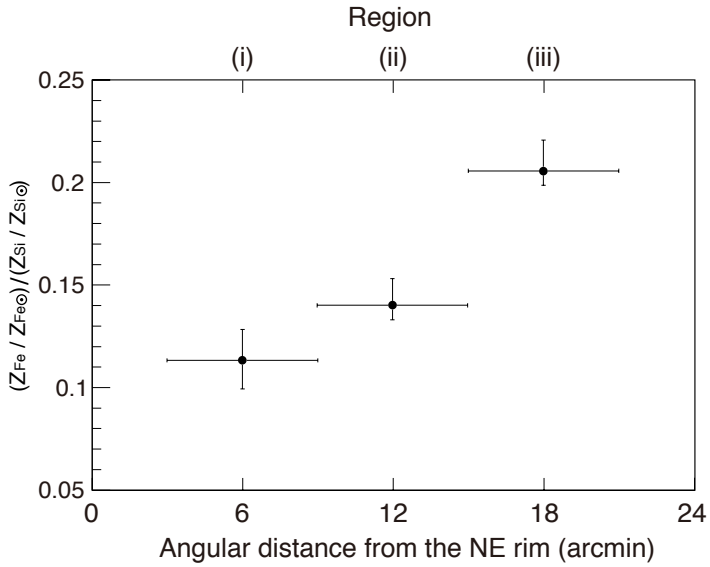

Figure 5.8: Abundance ratios of Fe to Si in the regions (i)–(iii) as a function of angular distances from the NE rim toward the center of the remnant.

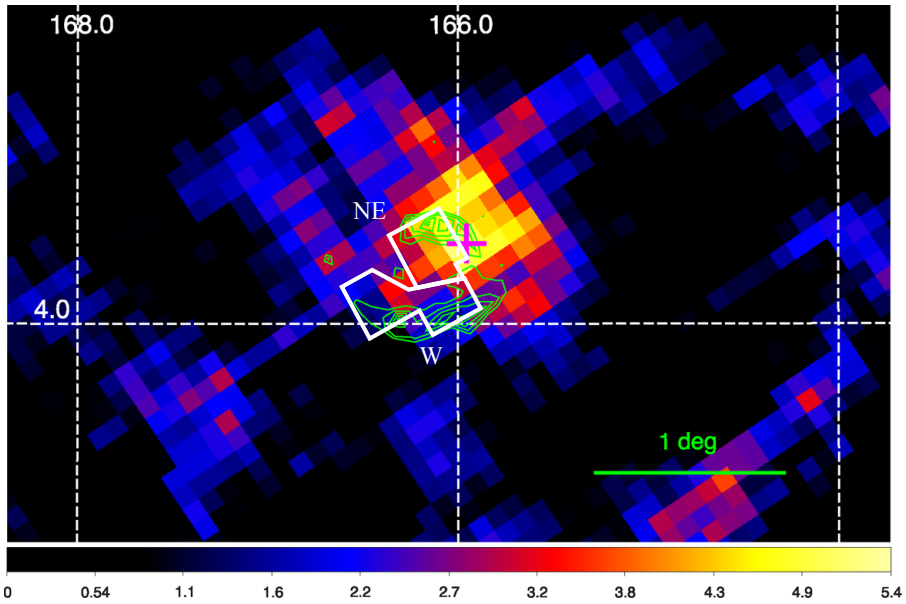

Figure 5.9: Signal-to-noise map in the G166.0+4.3 smoothed with a boxcar of length 0°.5 in the energy band of 0.5–2 GeV with Fermi (Araya, 2013). The green contours show the WENSS 325 MHz radio image. The while lines indicate the NE and W regions. The Galactic coordinates are referred.

is an IP, is expected to be almost the same as the age of the remnant, and, therefore, we estimate the age to be $t_{\rm age} = 1 \times 10^5 \ f^{1/2}$ yr. With $n_{e,\rm NE} \ t$, we can estimate the elapsed time since recombination started to dominate over ionization to be $t_{\rm rec} = 6 \times 10^4 \ f^{1/2}$ yr ($< t_{\rm age}$).

5.4.3 Origin of recombining plasma

As shown in §3.3, the rarefaction (Itoh & Masai, 1989) and thermal conduction (Kawasaki et al., 2002) scenarios have been considered for the formation process of RPs. In either case, the environment of the remnant is a key to the RP production process. We discovered an RP only in a part of G166.0+4.3, the outer part of the NE region, where the ambient gas is denser. In the W region, the spectrum is reproduced by the IP model. The different gas environments between the W and NE regions might actually be responsible for the difference of the plasma states.

In the rarefaction scenario, the electron temperature is decreased by adiabatic cooling when the blast wave breaks out of dense CSM into rarefied ISM. The lower the ISM density is, the more effective the adiabatic cooling must be (Shimizu et al., 2012). Therefore, in this scenario, we can naturally expect an RP in the W region whose ambient gas density would be lower. Our result, where we found an RP only in the NE region, is not simply explained by the rarefaction scenario.

In the thermal conduction scenario, an RP is anticipated in a part of the remnant where blast waves are in contact with cool dense gas. In the case of G166.0+4.3, the RP was indeed discovered in the denser NE region. In our results, the temperature of the inner Fe-rich plasma is higher ($kT_e = 0.87$ keV) than that of the outer RP ($kT_e = 0.46$ keV). In this scenario, the plasma is cooled from the outside layers. Therefore, it is possible that the plasma is cooled only in the outer part of the NE region.

Chapter 6

IC 443

6.1 Previous Works and Our Aims

IC 443 (G189.1+3.0) is a Galactic supernova remnant (SNR) at a distance of 1.5 kpc (Welsh & Sallmen, 2003). Its age is estimated to be in the range of 3–30 kyr (Petre et al., 1988; Olbert et al., 2001). Olbert et al. (2001) found a PWN in the southeastern part of the remnant, suggesting that IC 443 is a remnant of a core-collapse supernova. Seen in the radio and optical bands, IC 443 has two shells with different radii (e.g., Lee et al., 2008). The remnant is categorized as a mixed-morphology SNR since the X-ray emission has a center-filled morphology.

In X-rays, Kawasaki et al. (2002) measured the Lyα to Heα line intensity ratio of Si and S with ASCA, and found that the plasma in the northeastern part of the remnant is more ionized than expected in CIE. With Suzaku, Yamaguchi et al. (2009) discovered RRCs of Si and S in the northeastern region, which provided unambiguous evidence for an RP (Figure 6.1). Ohnishi et al. (2014) found RRCs of Ca and Fe in almost the same region as Yamaguchi et al. (2009) and indicated that heavier elements are also overionized.

IC 443 is interacting with both molecular and atomic gas (e.g., Lee et al., 2008). Cornett et al. (1977) discovered a dense molecular cloud associated with IC 443. CO line emissions in the southeastern part of the remnant suggest that the molecular cloud is interacting with IC 443 (e.g., Denoyer, 1979; Xu et al., 2011; Yoshiike, 2017). Measurements of the CO line velocity by Yoshiike (2017) suggest that the most part of the interacting molecular gas is located in front of IC 443. In the northeast, the SNR shock emits atomic lines expected from post-shock recombining gas (Fesen & Kirshner, 1980), and therefore, the shock is likely to be propagating into an atomic medium. Near-infrared observations also support the atomic gas in the northeast (e.g., Kokusho et al., 2013).

In this chapter, we perform spatially resolved X-ray spectroscopy of the SNR IC 443 with Suzaku and compare the results with the distribution of interstellar gas interacting with the remnant. We then discuss the implications particularly on the formation process of the RP. All spectral fits are performed with XSPEC version 12.9.0n. The plasma models are calculated with ATOMDB version 3.0.8. We used solar abundances given by Wilms et al. (2000).

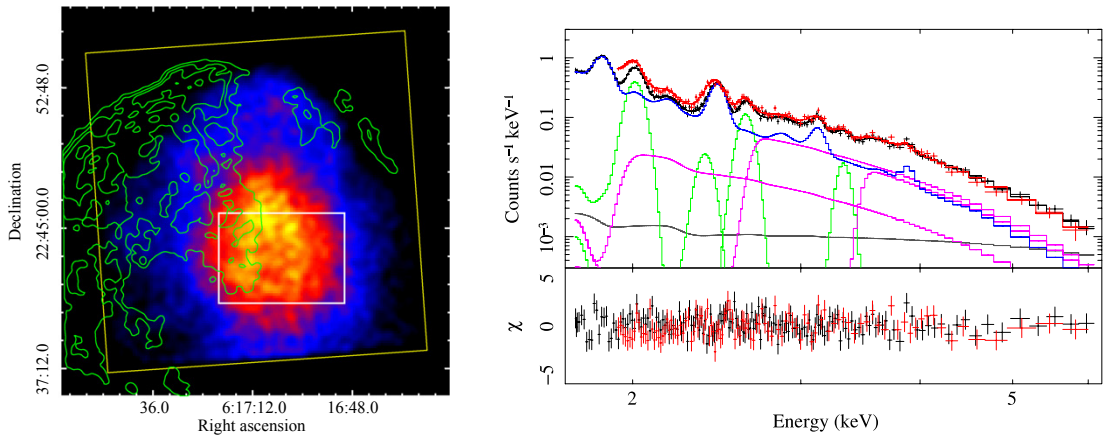

Figure 6.1: IC 443 image and spectrum taken from Yamaguchi et al. (2009). (left) Vignetting-corrected XIS image of the northern part of IC 443 in the 1.75–3.0 keV band. The optical Digitized Sky Survey image is overlapped in contours. (right) XIS spectrum in the 1.75-6.0 keV. Black and red represent FI and BI, respectively. Individual component of the best-fit model for the FI data are shown with solid lines; blue, green, and magenta are the VAPEC, Gaussians (Si Lyα, Si Lyβ, S Lyα and Ar Lyα), and RRC components of H-like Mg, Si and S, respectively.

6.2 Suzaku Observation and Data Reduction

Table 6.1 summarizes the Suzaku observation log of IC 443. We used the data from the XIS, which consists of four X-ray CCD cameras installed on the focal planes of the XRT. We do not use XIS2 and the part of XIS0 for the data acquired after November 2006 and June 2009, respectively, because they have not been functioning since these times (§4.3.1).

We reduced the data using the HEADAS software version 6.19. We used the calibration database released in April 2016 for processing the data. We removed flickering pixels by referring to the noisy pixel maps provided by the XIS team (§4.3.4). We also discarded pixels adjacent to the flickering pixels. NXBs were estimated by `xisnxbgen` (Tawa et al., 2008). Redistribution matrix files and ancillary response files were produced by `xisrmfgen` and `xissimarfgen` (Ishisaki et al., 2007), respectively.

Analyzing the XIS0 and 3 data taken in 2007, we noticed that the centroid energies of Lyα lines from IC 443, and Mn Kα and Kβ lines from the on-board calibration sources are shifted by 2–8 eV from the true values. We corrected the gain by using the Lyα lines of O, Mg, Si, S from IC 443, and Mn Kα and Kβ lines from the calibration sources as mentioned in §4.3.3.

Table 6.1: Suzaku observation log of IC 443.

Target	Obs. ID	Obs. date	(R.A., Dec.)	Exposure
IC 443 northeast	501006010	2007-03-06	($6^{\rm h}17^{\rm m}11^{\rm s}.4$, $22°46'32''.5$)	42 ks
IC 443 southeast	501006020	2007-03-07	($6^{\rm h}17^{\rm m}11^{\rm s}.3$, $22°28'46''.9$)	44 ks
IC 443 northwest	505001010	2010-09-17	($6^{\rm h}15^{\rm m}59^{\rm s}.4$, $22°45'18''.7$)	83 ks
IRAS 05262+4432 (Background)	703019010	2008-09-14	($5^{\rm h}29^{\rm m}56^{\rm s}.0$, $44°34'39''.2$)	82 ks

6.3 Analysis

6.3.1 Image

Figure 6.2a shows an XIS3 image of IC 443 in the energy band of 0.3–2.0 keV. We subtracted the NXB from the image and corrected for the vignetting effect of the XRT. The X-ray emissions in the east are center-filled as is previously known (e.g., Troja et al., 2006). In the northwest, the image shows a hint of a shell-like structure.

Figure 6.2b shows an XIS3 image in the 3.0–5.0 keV band. We found the PWN 1SAX J0617.1+2221 (region A) and the point
source U061530.75+224910.6 (region B) (Bocchino & Bykov, 2001, 2003). We found two additional point sources in the northwest and a source in the northeast which are already detected in XMM-Newton data by Bocchino & Bykov (2003). We excluded the PWN and the point sources for our spectral analysis of IC 443.

6.3.2 SNR spectra

Previous X-ray studies found that the spectra in the northeastern region can be reproduced with RP models (Yamaguchi et al., 2009; Ohnishi et al., 2014). In order to examine ionization states of the SNR plasmas in the other regions, we extracted spectra from the southeast (SE), northwest (NW) and northeast (NE) regions shown in Figure 6.2a. We used the spectrum of IRAS 05262+4432 (§5.3.2) for an X-ray background spectrum in this spectral analysis.

Figure 6.3 shows the XIS0+3 spectrum of the SE region after NXB subtraction. The characteristic structures of Si and S RRCs indicate that the plasma is in a recombination-dominant state. Following Yamaguchi et al. (2009), we first analyzed the spectrum in the energy band above 1.6 keV in order to quantify the ionization states of Si and S. We applied a model consisting of one RP component to the spectrum. We used the VVRNEI model in XSPEC. The initial plasma temperature $kT_{\rm init}$ was fixed at 5 keV, in which most Si and S ions become bare nuclei. The present electron temperature kT_e and ionization parameter $n_e t$ were allowed to vary. The abundances of Si, S, Ar, Ca and Fe were allowed to vary, whereas the Ni abundance was linked to Fe. The abundances of the other elements were fixed to solar. We used the Tuebingen-Boulder ISM absorption model (TBabs; Wilms et al., 2000), whose column density was fixed at 7.0×10^{21} cm^{-2} as determined by Kawasaki et al. (2002). For the XIS0+3 spectrum, we ignored the energy band of 1.78–1.92 keV because of the known calibration uncertainty around the neutral Si K-edge. Although we excluded the PWN from the spectrum extraction region, there is non-negligible leakage from the PWN due to the tail of the point spread function of the XRT. We, therefore, added a power law to account for the PWN emission. We fixed the photon index at 1.89 given by our spectral analysis of the PWN region (see Appendix A.1).

Figure 6.4a and Table 6.2 show the fitting results and the best-fit parameters, respectively. The spectrum is reproduced well by the model with $kT_e = 0.30 \pm 0.01$ keV and $n_e t = (4.6 \pm 0.1) \times 10^{11}$ s cm^{-3}. The electron temperature is significantly smaller than $0.61^{+0.03}_{-0.02}$ keV given by Yamaguchi et al. (2009). They fitted the spectrum with a phe-

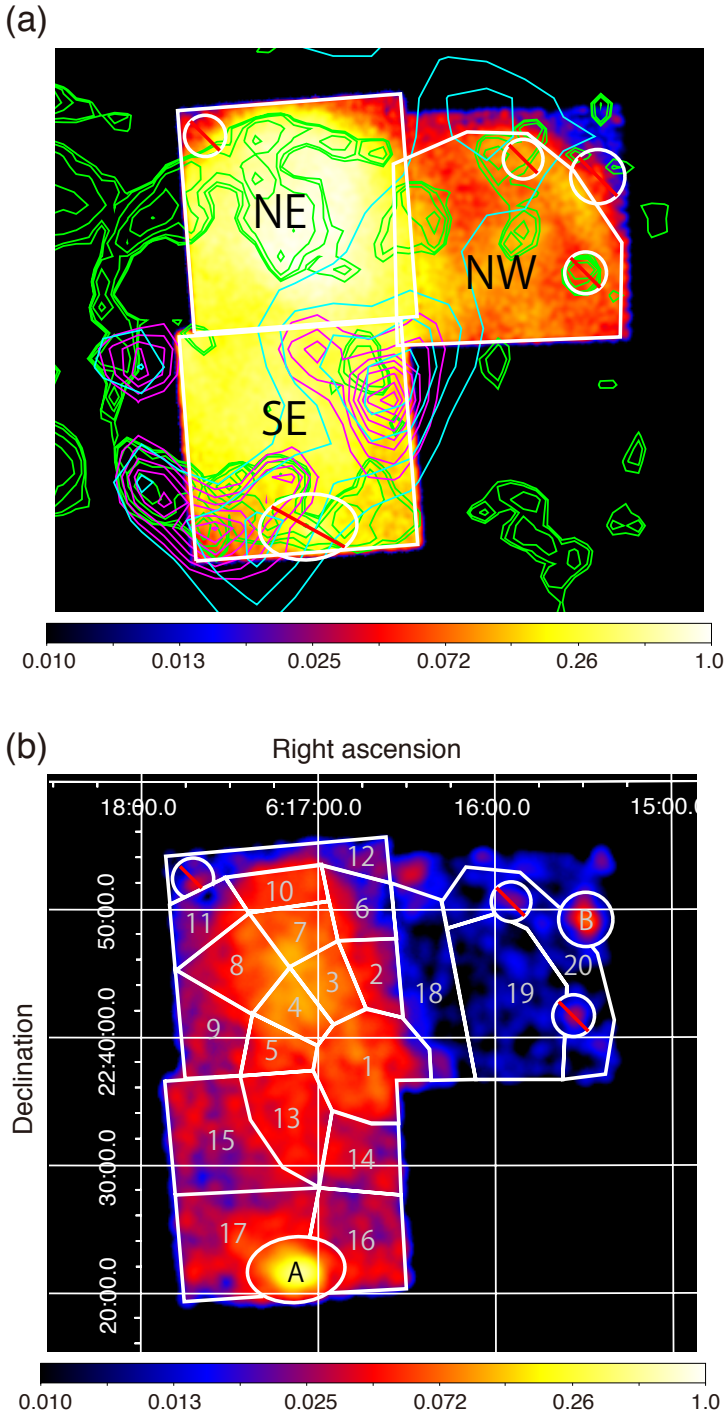

Figure 6.2: XIS3 images of IC 443 in the energy band of (a) 0.3–2.0 keV and (b) 3.0–5.0 keV after NXB subtraction and correction of the vignetting effect. In panel (a), we overlaid green contours of 1.4 GHz radio image which were obtained from the NRAO VLA Sky Survey (NVSS). The cyan and magenta contours are radio images of ^{12}CO($J = 1 - 0$) and ^{12}CO($J = 2 - 1$) obtained from the NANTEN2, respectively (Yoshiike, 2017). Sources in regions A and B in panel (b) are the PWN 1SAX J0617.1+2221 and the point source U061530.75+224910.6, respectively. The X-ray count rates are normalized so that the peaks become unity. The coordinate refers to the J2000.0 epoch.

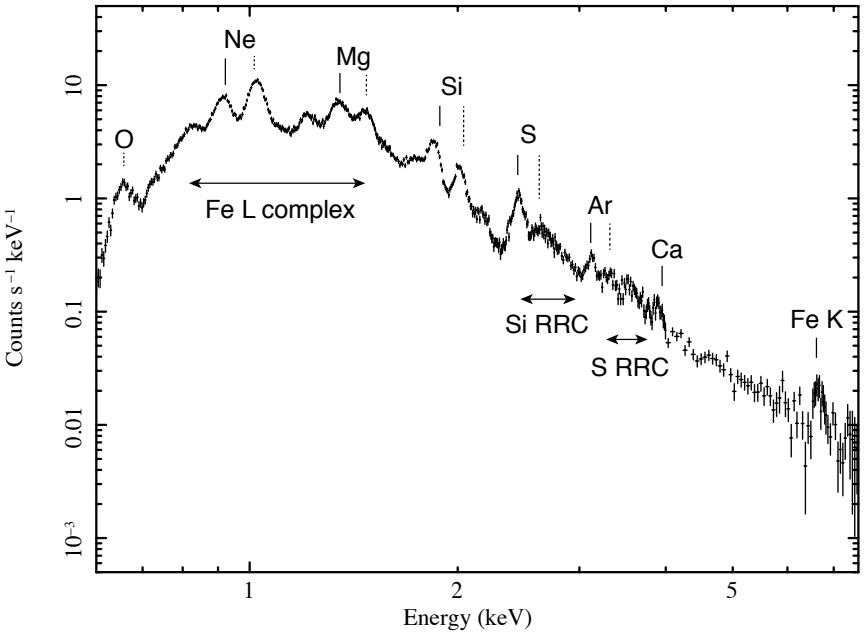

Figure 6.3: XIS0+3 spectrum of the SE region after NXB subtraction. The vertical solid and dashed black lines indicate the centroid-energies of Heα and Lyα lines, respectively. The arrows indicate the energy bands of the Fe-L complex and the radiative recombining continua of Si and S.

nomenological model consisting of a CIE component, Gaussians for Si, S and Ar Lyα lines and RRCs of Mg, Si and S. We here used a more physically oriented model that takes into account ion fractions and ionization timescales of all elements in the recombination-dominant state. In this model, RRCs of Ne and of lighter elements, which are not included in the model employed by Yamaguchi et al. (2009), extend up to the Si–S band. This difference would be the reason why we obtained lower kT_e.

We extrapolated the above model down to 0.6 keV, which results in large residuals in the soft band. We added a CIE component to the model following Kawasaki et al. (2002) and Bocchino et al. (2009), who modeled IC 443 spectra with two-component models with a CIE component for the soft band. The result is shown in Figure 6.4b and Table 6.2. Since we found the abundances of the CIE component are close to solar, we fixed them at solar values. The fit left residuals around 1.23 keV, most probably due to the lack of Fe-L lines in the model (e.g., Yamaguchi et al., 2011), and therefore, we added a Gaussian at 1.23 keV. The fit still left residuals at 0.87 keV, indicating a shortage of the emission line of FeXXVIII 1s2 2s2 2p4 3d1 $\rightarrow$ 1s2 2s2 2p5. To make the line stronger with $n_e t \sim 10^{11}$ s cm^{-3}, kT_e is required to be higher than ~ 0.5 keV.

We then fitted the spectrum with a model consisting of a power-law, a CIE, an RP and an additional higher kT_e components. We tried CIE, IP, and RP models as the high kT_e component, and found that the CIE and IP models fail to fit the spectrum. We applied a model consisting of a CIE and two RP components to the spectrum. The spectrum is well reproduced by the model with the significantly different kT_e between the two RP components whereas $n_e t$ and abundances of the two components are almost the same. Therefore, we linked $n_e t$ and the abundances of the components to each other.

The best-fit model and parameters are shown in Figure 6.4c and Table 6.2, respectively. The residuals at the FeXXVIII line was significantly improved. The electron temperatures of the CIE and two RP (named $\mathrm{RP_{cold}}$ and $\mathrm{RP_{hot}}$) components are 0.22 ± 0.01 keV, 0.19 ± 0.01 keV and $0.54^{+0.03}_{-0.01}$ keV, respectively. The ionization timescale of the RP components is $n_e t = (4.2^{+0.2}_{-0.1}) \times 10^{11}$ s cm^{-3}.

We performed spectral fitting of the NW and NE spectra in the same procedure as we did for the SE spectrum. We found that the model consisting of a CIE and two-RP components gives satisfactory fits to both spectra. The spectra with the best-fit models are plotted in Figures 6.4d and 6.4e and the best-fit parameters are again summarized in Table 6.2. The ionization parameter $n_e t$ of the NW spectrum is close to 2×10^{12} s cm^{-3}, which is a characteristic timescale for a plasma to reach CIE (Masai, 1994). Therefore, the RP in the NW is close to CIE. Since we cannot fit the spectrum in the energy band of the Fe-L complex of the NW spectrum, we allowed the Fe abundance of the CIE component to vary. The fit gave somewhat higher Fe abundance of 1.3 ± 0.1, but the abundance is still close to solar. Although kT_e and $n_e t$ of the NW and NE spectra are close to those of the SE spectrum, normalization ratios of the RP components are significantly different, indicating that the RP components have spatial variation.

In order to conduct spatially resolved spectroscopy in greater detail, we divided the remnant into 20 regions as shown in Figure 6.2b and extracted spectra from each region. We fitted the spectra with the above model, and found that it reproduces all the spectra well. The details of the fits are described in Appendix A.2. Since the leakage from the PWN and the point sources contaminate the spectra of regions 16, 17 and 20, we added a power law to the model for these spectra. The photon indices were fixed at 1.89 and 2.22, which are determined by our analysis in Appendix A.1, for the PWN and the point-source U061530.75+224910.6, respectively. The obtained ranges of kT_e are 0.19–0.28 keV, 0.16–0.28 keV and 0.48–0.67 keV for the CIE, $\mathrm{RP_{cold}}$ and $\mathrm{RP_{hot}}$ components, respectively. The electron temperature of the CIE component is uniform whereas those of the $\mathrm{RP_{cold}}$ and $\mathrm{RP_{hot}}$ components decrease toward the southeast as shown in Figures 6.5a–6.5c. Figures 6.5d and 6.5e show the map of N_{H} and $n_e t$, respectively. In the northwest, $n_e t$ is larger than those of the other regions.

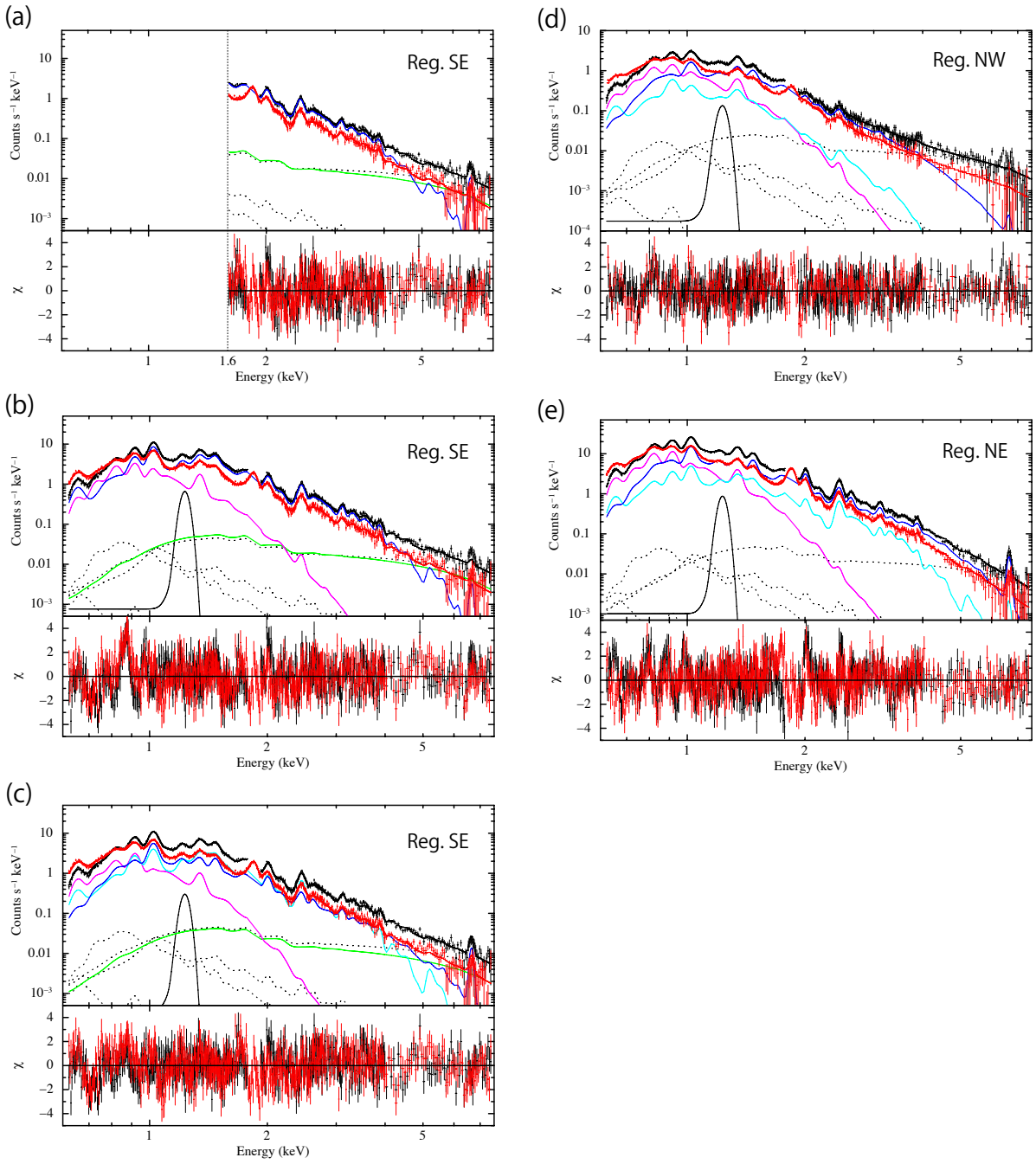

Figure 6.4: XIS0+3 (black crosses) and XIS1 (red crosses) spectra in the SE (a–c), NW (d), and NE (e) regions. Each spectrum is fitted with the model consisting of the SNR and background components. The solid and dotted lines show the SNR and background models of XIS0+3, respectively. The SNR model consists of power-law (green lines), CIE (magenta lines), $\mathrm{RP}_{\mathrm{cold}}$ (cyan lines) and $\mathrm{RP}_{\mathrm{hot}}$ (blue lines) components, respectively.

Table 6.2: Best-fit model parameters of the SE, NW, and NE spectra.

Model function	Parameter	SE 1.6–7.5 keV	SE 0.6–7.5 keV	SE 0.6–7.5 keV	NW 0.6–7.5 keV	NE 0.6–7.5 keV
TBabs	$N_{\rm H}$ (10^{22} cm^{-2})	0.70 (fixed)	$0.90^{+0.02}_{-0.01}$	$0.88^{+0.01}_{-0.02}$	$0.74^{+0.02}_{-0.03}$	$0.85^{+0.01}_{-0.01}$
VVRNEI1	kT_e (keV)	———	$0.28^{+0.01}_{-0.03}$	$0.22^{+0.01}_{-0.01}$	$0.26^{+0.02}_{-0.02}$	$0.23^{+0.01}_{-0.01}$
(CIE comp.)	$Z_{\rm Fe} = Z_{\rm Ni}$ (solar)	———	1 (fixed)	1 (fixed)	1 (fixed)	$1.3^{+0.1}_{-0.1}$
	$Z_{\rm other}$ (solar)	———	1 (fixed)	1 (fixed)	1 (fixed)	1 (fixed)
	VEM (10^{57} cm^{-3})†	———	$8.9^{+2.1}_{-0.6}$	$14.2^{+1.6}_{-1.9}$	$3.5^{+1.3}_{-1.0}$	$35.1^{+2.2}_{-3.9}$
VVRNEI2	kT_e (keV)	$0.30^{+0.01}_{-0.01}$	$0.26^{+0.01}_{-0.01}$	$0.19^{+0.01}_{-0.01}$	$0.22^{+0.06}_{-0.01}$	$0.24^{+0.01}_{-0.01}$
($\rm RP_{cold}$ comp.)	$kT_{\rm init}$ (keV)	5 (fixed)	5 (fixed)	5 (fixed)	5 (fixed)	5 (fixed)
	$Z_{\rm O}$ (solar)	1 (fixed)	1 (fixed)	1 (fixed)	1 (fixed)	$2.4^{+0.6}_{-0.3}$
	$Z_{\rm Ne}$ (solar)	1 (fixed)	$2.4^{+0.2}_{-0.1}$	$3.2^{+0.2}_{-0.2}$	$1.5^{+0.2}_{-0.2}$	$3.8^{+0.4}_{-0.3}$
	$Z_{\rm Mg}$ (solar)	1 (fixed)	$1.5^{+0.1}_{-0.1}$	$1.6^{+0.1}_{-0.1}$	$1.1^{+0.1}_{-0.1}$	$2.2^{+0.3}_{-0.1}$
	$Z_{\rm Si}$ (solar)	$1.1^{+0.1}_{-0.1}$	$1.5^{+0.1}_{-0.1}$	$1.8^{+0.1}_{-0.1}$	$0.8^{+0.1}_{-0.1}$	$3.9^{+0.4}_{-0.2}$
	$Z_{\rm S}$ (solar)	$0.6^{+0.1}_{-0.1}$	$0.9^{+0.1}_{-0.1}$	$1.2^{+0.1}_{-0.1}$	$0.5^{+0.1}_{-0.1}$	$2.6^{+0.4}_{-0.1}$
	$Z_{\rm Ar}$ (solar)	$0.6^{+0.1}_{-0.1}$	$0.8^{+0.1}_{-0.1}$	$1.2^{+0.1}_{-0.1}$	$= Z_{\rm S}$	$2.4^{+0.2}_{-0.2}$
	$Z_{\rm Ca}$ (solar)	$0.6^{+0.1}_{-0.1}$	$0.8^{+0.2}_{-0.1}$	$1.2^{+0.2}_{-0.2}$	$= Z_{\rm S}$	$2.2^{+0.3}_{-0.2}$
	$Z_{\rm Fe} = Z_{\rm Ni}$ (solar)	$0.2^{+0.1}_{-0.1}$	$0.1^{+0.1}_{-0.1}$	$0.5^{+0.1}_{-0.1}$	$0.2^{+0.1}_{-0.1}$	$0.8^{+0.1}_{-0.1}$
	$n_e t$ (10^{11} s cm^{-3})	$4.6^{+0.1}_{-0.1}$	$4.1^{+0.2}_{-0.1}$	$4.2^{+0.2}_{-0.1}$	$9.7^{+0.9}_{-1.1}$	$5.4^{+0.1}_{-0.1}$
	VEM (10^{57} cm^{-3})†	$30.5^{+1.4}_{-1.4}$	$21.7^{+0.5}_{-0.9}$	$12.6^{+0.7}_{-1.0}$	$2.4^{+0.8}_{-1.4}$	$7.0^{+0.4}_{-0.5}$
VVRNEI3	kT_e (keV)	———	———	$0.54^{+0.03}_{-0.01}$	$0.63^{+0.02}_{-0.01}$	$0.61^{+0.01}_{-0.01}$
($\rm RP_{hot}$ comp.)	$kT_{\rm init}$ (keV)	———	———	5 (fixed)	5 (fixed)	5 (fixed)
	$Z_{\rm all}$ (solar)	———	———	$= \rm RP_{cold}$	$= \rm RP_{cold}$	$= \rm RP_{cold}$
	$n_e t$ (10^{11} s cm^{-3})	———	———	$= \rm RP_{cold}$	$= \rm RP_{cold}$	$= \rm RP_{cold}$
	VEM (10^{57} cm^{-3})†	———	———	$4.1^{+0.2}_{-0.4}$	$1.8^{+0.1}_{-0.2}$	$6.8^{+0.4}_{-0.9}$
Gaussian	Centroid (keV)	———	1.23 (fixed)	1.23 (fixed)	1.23 (fixed)	1.23 (fixed)
	Normalization‡	———	132^{+15}_{-15}	56^{+8}_{-9}	49^{+16}_{-6}	142^{+18}_{-19}
Power law	Photon index	1.89 (fixed)	1.89 (fixed)	1.89 (fixed)	———	———
	Normalization*	151^{+23}_{-23}	171^{+22}_{-20}	130^{+12}_{-14}	———	———
	χ^2_ν (ν)	1.55 (594)	1.71 (1126)	1.47 (1124)	1.23 (838)	1.67 (1123)

† Volume emission measure at the distance of 1.5 kpc: $VEM = \int n_e n_{\rm H} dV$, where n_e, $n_{\rm H}$, and V are the electron and hydrogen densities, and the emitting volume, respectively.

‡ The unit is photons s^{-1} cm^{-2} sr^{-1}.

* The unit is photons s^{-1} cm^{-2} keV^{-1} sr^{-1} at 1 keV.

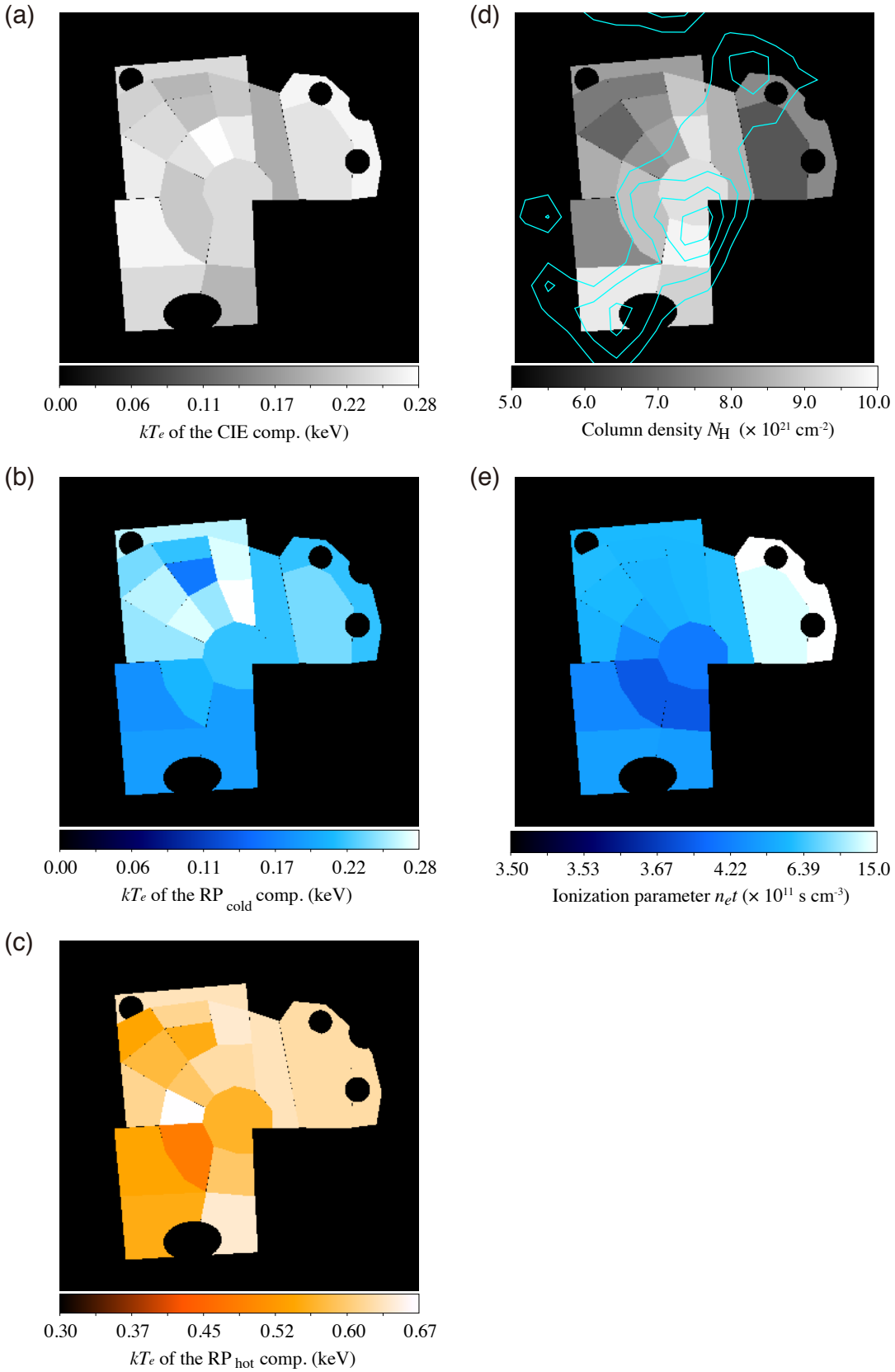

Figure 6.5: (a–c) Maps of the electron temperatures kT_e of the CIE, $\mathrm{RP_{cold}}$, $\mathrm{RP_{hot}}$ components. (d) Map of the column density N_H with the $^{12}\mathrm{CO}(J = 1-0)$ emissions (cyan contours; Yoshiike, 2017). (e) Map of the ionization parameters $n_e t$.

6.4 Discussion on IC 443

6.4.1 Absorption by the molecular cloud

Figure 6.5d shows the spatial distribution of the X-ray absorption column densities (hereafter $N_{\rm H,X}$). Since our analysis covers almost the whole remnant, we can perform a systematic comparison between $N_{\rm H,X}$ and the ambient gas distribution. Our spectral fits gave high $N_{\rm H,X}$ in regions 1, 2, 5, 6, 13, 14, 16, 17 and 18, which coincide with the locations of the molecular cloud traced by the ^{12}CO($J = 1$–0) line (e.g., Xu et al., 2011; Yoshiike, 2017). Our result indicates that the cloud is located in front of the remnant. If we subtract the lowest $N_{\rm H,X}$ (region 19) from the highest one (region 14), we obtain $(3.1 \pm 0.6) \times 10^{21}$ cm^{-2}, which can be attributed to the absorption by the molecular cloud.

Yoshiike (2017) observed the ^{12}CO($J = 1$–0) line with the NANTEN2 telescope, and concluded that the molecular cloud is located in front of IC 443 based on line velocity measurements. We note that Troja et al. (2006) also reached the same conclusion based on a comparison between XMM-Newton data and CO data. Yoshiike (2017) estimated the column density of the molecular cloud to be $N_{\rm H,CO} = (6.1 \pm 0.8) \times 10^{21}$ cm^{-2}. Although the estimate by Yoshiike (2017) is somewhat larger than ours, the two measurements can be regarded to be consistent with each other, considering the fact that the estimate by Yoshiike (2017) is obtained for the CO emission peak location and that our estimate is an average of a much larger region.

6.4.2 Origin of the CIE plasma

In the spectral analysis, we successfully reproduced the spectra from all the regions with the model consisting of the CIE, RP$_{\rm cold}$ and RP$_{\rm hot}$ components. The abundances of the CIE component are consistent with solar, suggesting that the component is of shocked ISM origin. The spatial distribution of the component also supports this picture. Figure 6.6a-1 shows the normalization ratios of the CIE component to the RP$_{\rm hot}$ component plotted as a function of the angular distance from the center of the remnant which we define as (R.A., Dec.) = ($6^{\rm h}17^{\rm m}40^{\rm s}.0$, $22^\circ38'00''.0$). The map of the normalization ratio is shown in Figure 6.6a-2. The normalization ratios tend to increase toward the outer regions, suggesting that the CIE plasma is concentrated in the rim as is generally expected for a shocked ISM emission.

6.4.3 Origin of the recombining plasmas

In section 6.3.2, we found that the emission is well reproduced by a model which includes two RP components with different kT_e. As shown in Figures 6.5a–6.5c, the electron temperatures of both components decrease toward the southeast. The southeastern region coincides with the locations where the molecular cloud is known to be interacting with the remnant based on the ^{12}CO($J = 2$–1) to ^{12}CO($J = 1$–0) intensity ratio (e.g., Xu et al., 2011; Yoshiike, 2017). The normalization ratio of the two RP components points to a similar tendency. Figures 6.6b-1 and 6.6b-2 show a radial profile and a map of the RP$_{\rm cold}$ to RP$_{\rm hot}$ normalization ratio, respectively. As opposed to Figure 6.6a-1, no clear correlation is seen in the radial profile. From the map, it is evident that the ratio is

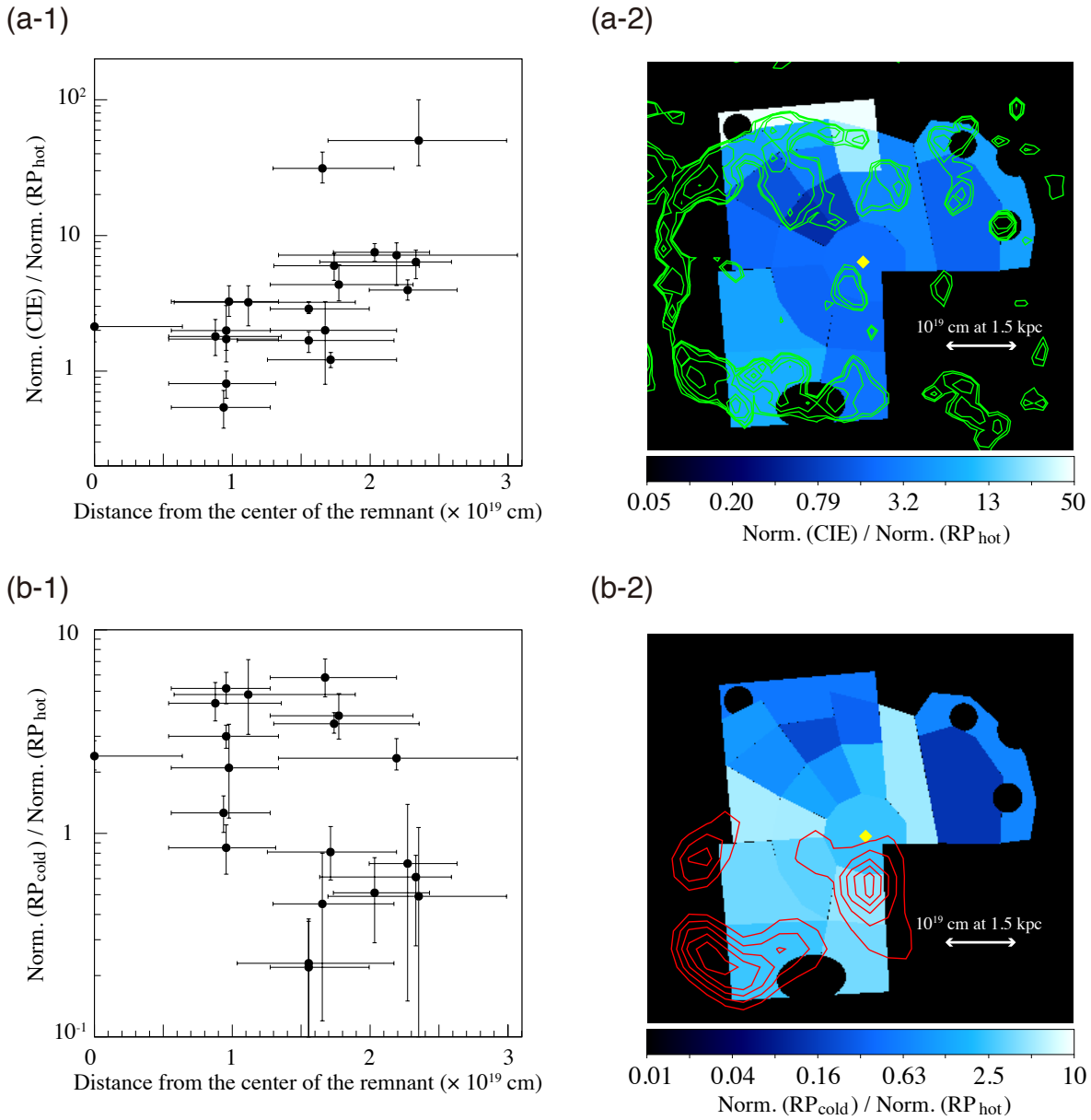

Figure 6.6: (a-1) Radial profile and (a-2) map of the CIE to $\mathrm{RP_{hot}}$ normalization ratio with the 1.4 GHz radio emissions (green contours). (b-1) Radial profile and (b-2) map of the $\mathrm{RP_{cold}}$ to $\mathrm{RP_{hot}}$ normalization ratio with a map of the $^{12}\mathrm{CO}(J=2-1)$ to $^{12}\mathrm{CO}(J=1-0)$ intensity ratio (red contours; Yoshiike, 2017). The yellow diamonds denote the center of the remnant (R.A., Dec.) = ($6^{\mathrm{h}}17^{\mathrm{m}}40^{\mathrm{s}}.0$, $22°38'00''.0$). The length of the white arrows correspond to 10^{19} cm at the distance of 1.5 kpc.

larger in the southeastern region, where kT_e is also lower than the other regions (see Figures 6.5a–6.5c). These results on kT_e and the normalization ratio together indicate that the SNR plasma is cooler in the region where the shock is in contact with the molecular cloud.

One of the plausible mechanisms to explain the cooler plasma in the southeastern region is cooling of the X-ray emitting plasma by the molecular cloud via thermal conduction. If the cooling proceeds faster than the recombination timescale of the plasma, the recombining plasma can also be explained by the thermal conduction. The thermal conduction scenario is proposed for the formation process of an RP in G166.0+4.3 (Chapter 5). We found kT_e of a high-density region of the SNR is significantly lower than that of a low-density region. The observational result is in fact similar to our findings on IC 443 reported in this chapter. It is interesting to point out that the plasma in the northwestern region is close to CIE with $n_e t \sim 10^{12}$ s cm^{-3}. A possible explanation is that the cooling of the plasma in this region is less efficient since the region is far away from the molecular cloud, which would be the major cooling source for IC 443. Lower ambient gas density, which is suggested by the large shell radius in the west (Lee et al., 2008), would also make the cooling less efficient.

Chapter 7

W44

7.1 Previous Works and Our Aims

W44 (G34.7−0.4) is a middle-aged SNR with an estimated age of $\sim$ 20 kyr (Wolszczan et al., 1991) and is located at a distance of $\sim$ 3 kpc (Claussen et al., 1997). W44 has a synchrotron radio shell (e.g., Kundu & Velusamy, 1972) and a center-filled X-ray emission (e.g., Rho et al., 1994), and thus it is classified into a mixed-morphology SNR. W44 is known to be interacting with molecular clouds from CO line (e.g., Seta et al., 2004) and 1720 MHz OH maser (e.g., Claussen et al., 1997) observations.

In the X-ray band, Rho et al. (1994) obtained spectra with ROSAT, EXOSAT and Einstein, and interpreted them as an IP emission (White & Long, 1991). Kawasaki et al. (2005) analyzed W44 spectra obtained with ASCA and measured ionization temperatures based on the Si Lyα to Heα intensity ratios. They claimed that the plasma is nearly in a CIE state because kT_z is almost equal to kT_e. In a Suzaku observation of the central region, Uchida et al. (2012) found RPs. The best-fit parameters indicate that the plasma was cooled down from $kT_{\rm init} \sim 1$ keV to $kT_e \sim 0.5$ keV. They also found hard X-ray emissions inside the SNR and interpreted them as a synchrotron enhancement in the vicinity of a molecular cloud.

After the work by Uchida et al. (2012), five more W44 observations with Suzaku were carried out to cover the whole remnant. In this chapter, we analyze data from the six Suzaku observations of W44 and perform spatially resolved X-ray spectroscopy to compare the results with the distribution of the ambient gas interacting with the remnant. We then discuss the implications particularly for the formation process of the RP. All spectral fits are performed with XSPEC version 12.9.0n. The plasma models are calculated with ATOMDB version 3.0.8. We used solar abundances given by Wilms et al. (2000).

7.2 Suzaku Observations and Data Reduction

We performed Suzaku deep observations of W44, whose log is summarized in Table 7.1. The total exposure time is about 335 ks. The XIS FOVs of each observation are shown in Figure 7.1a. In this analysis, we used XIS data excluding those from XIS2 and a part of XIS0 because they were not functioning at the time of the observations (§4.3.1). We reduced the data and estimated NXBs with the same method in Chapter 6.

Table 7.1: Suzaku observation log of W44.

Target	Obs. ID	Obs. date	(R.A., Dec.)	Effective Exposure
W44 center	505004010	2010-04-10	($18^{h}56^{m}08^{s}.4$, $1°23'19''.0$)	61 ks
W44 west	508002010	2013-10-24	($18^{h}55^{m}45^{s}.4$, $1°19'17''.8$)	61 ks
W44 south	508003010	2013-10-22	($18^{h}56^{m}14^{s}.7$, $1°12'36''.0$)	67 ks
W44 south	508003020	2014-04-09	($18^{h}56^{m}13^{s}.1$, $1°13'14''.9$)	32 ks
W44 east	508004010	2013-10-18	($18^{h}56^{m}35^{s}.0$, $1°17'56''.8$)	58 ks
W44 north	508005010	2013-10-19	($18^{h}55^{m}50^{s}.4$, $1°29'34''.1$)	56 ks
HESS J1857-A (Background)	506019010	2011-09-18	($18^{h}56^{m}51^{s}.0$, $2°45'06''.8$)	4 ks
HESS J1857-B (Background)	506020010	2011-11-01	($18^{h}58^{m}11^{s}.6$, $2°44'57''.8$)	4 ks

7.3 Analysis

7.3.1 Image

Figures 7.1a, 7.1b, 7.1c and 7.1d show XIS3 mosaic images of W44 in the energy bands of 0.3–10 keV, 0.3–10 keV, 3–7 keV and 0.3–2 keV, respectively. We subtracted NXB from the images and corrected for the vignetting effect of the XRT. As shown in Figure 7.1b, W44 has a center-filled X-ray emission with a radio shell as is previously known (e.g., Rho et al., 1994). In the hard band image of Figure 7.1c, we found three hard sources in regions A, B and C. The hard X-ray source in region A is the one discovered by Uchida et al. (2012). The hard source in region B is located at the position of the PWN (Petre et al., 2002).

7.3.2 X-ray background subtraction

In order to estimate X-ray background for the spectral analysis, we analyzed observation data of nearby targets (HESS J1857-A and HESS J1857-B; Table 7.1). We extracted spectra from source-free regions and merged the spectra from the two observations. We fitted the spectrum with a model by Uchiyama et al. (2013), who studied the X-ray emission from the Galactic plane. The model consists of three components; the Galactic ridge X-ray emission (GRXE), the CXB and the foreground emission (FE).

The GRXE model consists of low-kT_e thermal plasma (LP), high-kT_e thermal plasma (HP), an emission from cold neutral matter (cold matter: CM) expressed by a power law, and neutral Fe Kα (6.40 keV) and Kβ (7.06 keV) lines. We allowed the absorption column density of the GRXE and normalizations of the LP, HP and CM components to vary. The other parameters were fixed at the values given by Uchiyama et al. (2013). A normalization of the FE component was allowed to vary, whereas we fixed the other parameters of the FE at the values by Uchiyama et al. (2013). Figure 7.2 and Table 7.2 show the fitting result and the best-fit parameters, respectively.

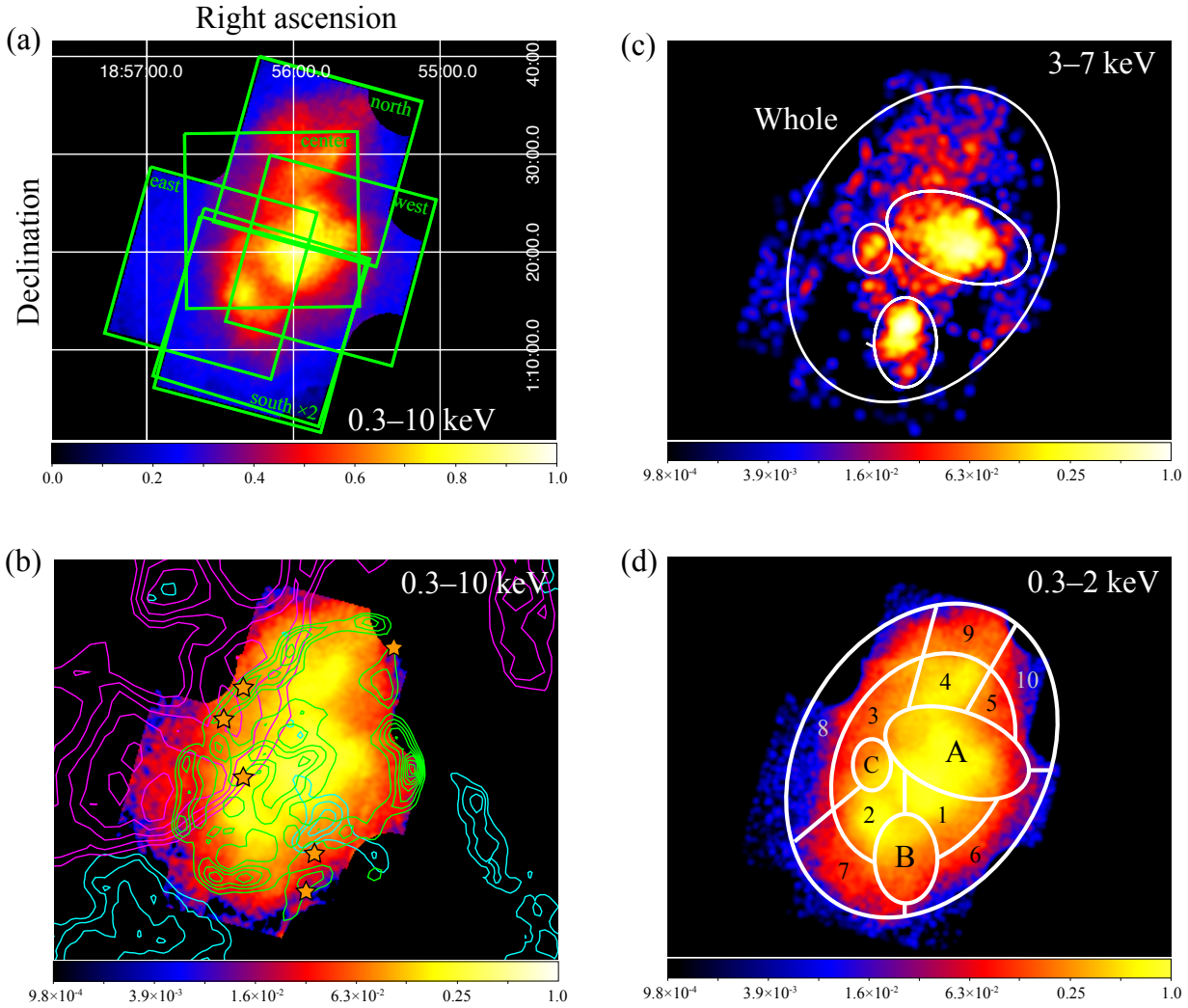

Figure 7.1: XIS3 images of W44 in the energy band of (a,b) 0.3–10 keV, (c) 3–7 keV and (d) 0.3–2 keV after the NXB subtraction and correction for the vignetting effect. The X–ray count rates are normalized so that the peaks become unity. In panel (a), the green squares are the FOVs of XIS3 in each observation. The coordinate refers to the J2000.0 epoch. In panel (b), the green contours are a radio image as seen in 20 cm wavelength by the Very Large Array (VLA) (Helfand et al., 2006). The magenta and cyan contours are the NANTEN2 ^{12}CO(J = 2–1) images in the velocity range of 40–50 km s^{-1} and 50–60 km s^{-1}, respectively (Uchida et al., 2012). The orange stars indicate the locations of the 1720 MHz OH maser emissions (Claussen et al., 1997). The white lines in panels (c) and (d) indicate regions for the spectral extraction.

Table 7.2: Best-fit model parameters of the background spectra for W44.

Component	Model function	Parameter	Value
Absorption $_{\rm GRXB}$	TBabs	$N_{\rm H}$ (10^{22}cm^{-2})	$2.7\ ^{+0.2}_{-0.3}$
LP	VAPEC	kT_e (keV)	1.33 (fixed)
		$Z_{\rm Ar}$ (solar)	1.07 (fixed)
		$Z_{\rm other}$ (solar)	0.81 (fixed)
		Normalization†	126 ± 30
HP	VAPEC	kT_e (keV)	6.64 (fixed)
		$Z_{\rm Ar}$ (solar)	1.07 (fixed)
		$Z_{\rm other}$ (solar)	0.81 (fixed)
		Normalization†	$98\ ^{+7}_{-16}$
CM	Power law	Photon index	2.13 (fixed)
		Normalization*	< 9.0
	Gaussian1	Centroid (keV)	6.4 (fixed)
		Normalization‡	= Norm $_{\rm Power\ law} \times 1.103$
	Gaussian2	Centroid (keV)	7.06 (fixed)
		Normalization‡	= Norm $_{\rm Gaussian1} \times 0.125$
Absorption $_{\rm CXB}$	TBabs	$N_{\rm H}$ (10^{22}cm^{-2})	= Absorption $_{\rm GRXB} \times 2$
CXB	Power law	Photon index	1.4 (fixed)
		Normalization*	9.9 (fixed)
Absorption $_{\rm FE}$	TBabs	$N_{\rm H}$ (10^{22}cm^{-2})	0.56 (fixed)
FE	APEC1	kT_e (keV)	0.59 (fixed)
		$Z_{\rm all}$ (solar)	0.05 (fixed)
		Normalization†	68 ± 8
	APEC2	kT_e (keV)	0.09 (fixed)
		$Z_{\rm all}$ (solar)	0.05 (fixed)
		Normalization†	= Norm $_{\rm APEC1} \times 261.5$
		χ^2_ν (ν)	1.37 (252)

* The unit is photons s^{-1} cm^{-2} keV^{-1} sr^{-1} at 1 keV.
† The emission measure integrated over the line of sight, i.e., (1 / 4π) $\int n_e n_{\rm H} dl$ in units of 10^{14} cm^{-5} sr^{-1}.
‡ The unit is photons s^{-1} cm^{-2} sr^{-1}.

7.3.3 SNR spectra

We extracted a spectrum from the Whole region indicated in Figure 7.1c. The regions A, B and C, where the hard X-ray emissions are located, are excluded from the Whole region. Figure 7.3 shows the XIS0+3 spectrum in the 0.6–5.0 keV band. Line emissions of Ne, Mg, Si, S and Ar are clearly seen. We also found Si and S RRCs, which provide clear evidence that the plasma is in a recombination-dominant state.

We fitted the spectrum with the model consisting of the SNR component and the background (§7.3.2). A previous X-ray study found that the W44 spectrum in the centeral region can be reproduced by an RP model with $kT_e \sim 0.5$ keV, $kT_{\rm init} \sim 1$ keV and $n_e t \sim 6 \times 10^{11}$ s cm^{-3} (Uchida et al., 2012). Following them, we first applied an RP model to the Whole spectrum, by using the VVRNEI model in XSPEC. We allowed $N_{\rm H}$, kT_e, $kT_{\rm init}$, $n_e t$ and the normalization of the RP component to vary. The abundances of Ne, Mg, Si, S, Ar, and Fe were also allowed to vary, whereas the O, Ca, and Ni abundances

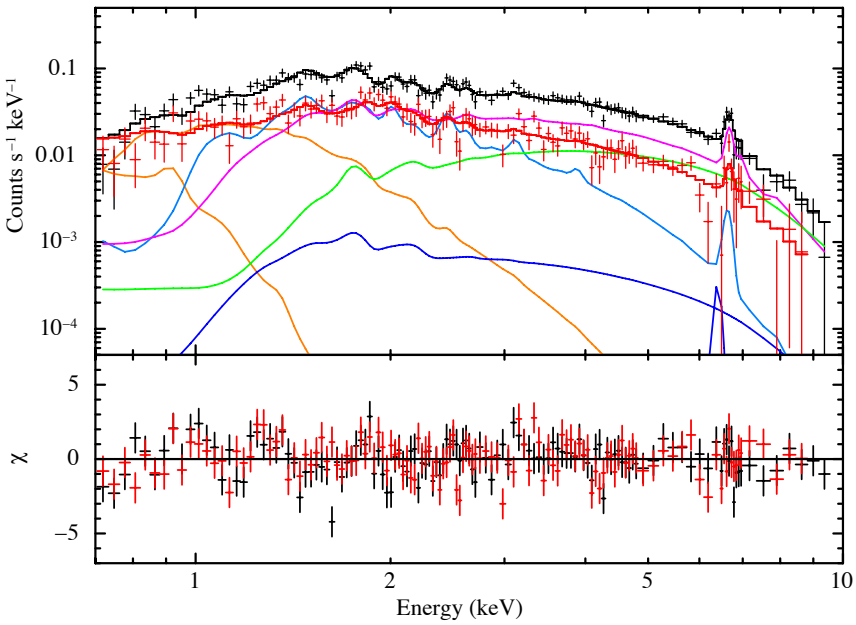

Figure 7.2: X-ray background spectra of XIS0+3 (black crosses) and XIS1 (red crosses) extracted from the source-free regions of HESS J1857-A and HESS J1857-B. The black and red solid lines indicate the best-fit models of XIS0+3 and XIS1, respectively. The LP, HP, CM, CXB, and FE components of XIS0+3 show the solid cyan, magenta, blue, green, and orange lines, respectively. The bottom panel shows the residuals from the best-fit model.

were linked to Ne, Ar, and Fe, respectively. The abundances of the other elements were fixed to solar. For the XIS0+3 spectrum, we ignored the 1.78-1.92 keV band because of the known calibration uncertainty around the neutral Si K-edge. The fit left residuals around 1.23 keV, most probably due to the lack of Fe-L lines in the model (e.g., Yamaguchi et al., 2011), and, therefore, we added a Gaussian at 1.23 keV. The result is shown in Figure 7.4a and Table 7.3. The spectrum in the high energy band above 1.7 keV is well reproduced by the RP model, indicating that the plasma has a component in a recombination-dominant state. On the other hand, the fit left residuals in the low energy band of 0.7–1.7 keV, suggesting that the plasma has an additional component in the soft band.

To account for the soft band residuals, we tried the CIE, IP and RP models. Abundances of Ne and Mg were allowed to vary, whereas that of O was linked to Ne. The other abundances were fixed to solar. We allowed kT_e and a normalization of the soft-band component to vary. The residuals in the soft band was significantly improved independent of the choice of the model. Nonetheless, we here chose to use the CIE model, following the IC 443 analysis in §6.4.2. We present the fitting result and the best-fit parameters in Figure 7.4b and Table 7.3, respectively. We found that kT_e of the CIE component is 0.22 ± 0.01 keV, which is almost the same as those of IC 443. The best-fit parameters of kT_e, $kT_{\rm init}$ and $n_e t$ of the RP component are 0.37 ± 0.01 keV, 0.93 ± 0.01 keV and $(3.5^{+0.2}_{-0.3}) \times 10^{11}$ s cm^{-3}, respectively. The obtained kT_e is lower than that given by Uchida et al. (2012), possibly indicating that the plasma in the Whole region on average is colder than the plasma in the central region, where Uchida et al. (2012) analyzed. The obtained $n_e t$ is smaller than that by Uchida et al. (2012), possibly indicating that the recombination timescale of the outer plasma is shorter than that of the central plasma. In order

to conduct spatially resolved spectroscopy, we divided the Whole region into 10 regions as shown in Figure 7.1d and extracted spectra from each region. We fitted the spectra with the above model but we fixed $kT_{\rm init}$ and the O, Ne, and Mg abundances of the CIE component and the O and Ne abundances of the RP component to the best-fit values in the Whole fit. In most of the regions, the spectra can be reproduced well by the model. The fit for the region 1 spectrum, however, left residuals in the high energy band above 4 keV, indicating that the spectrum has a hard X-ray component. An additional fit for the hard X-ray component is shown in the next subsection (§7.3.4). Each spectrum with the best-fit models is plotted in Appendix B.1.

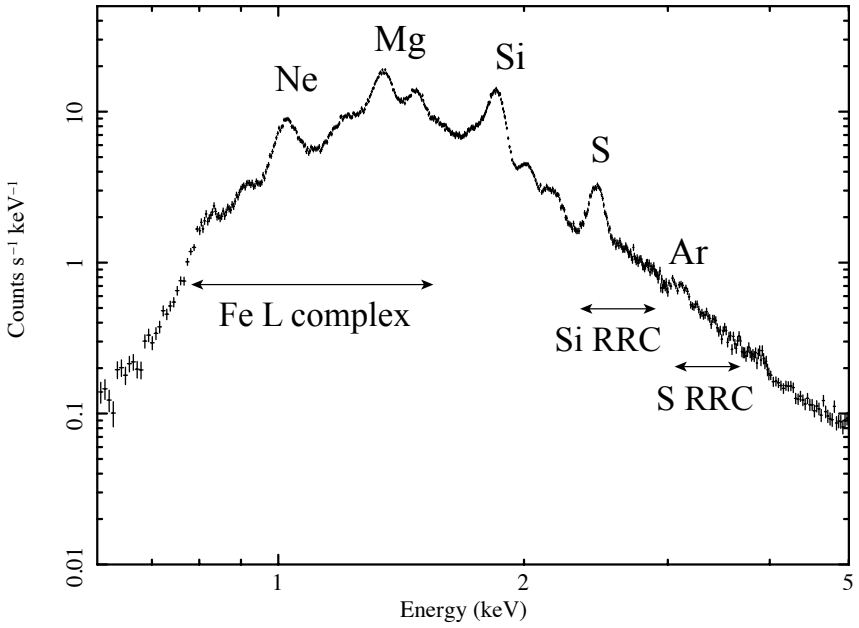

Figure 7.3: XIS0+3 spectra of the Whole region in the 0.6–10 keV band after NXB subtraction. Emission lines of Ne, Mg, Si, S and Ar can be seen in the spectrum. The arrows indicate the energy bands of the Fe L complex and the RRCs of Si and S.

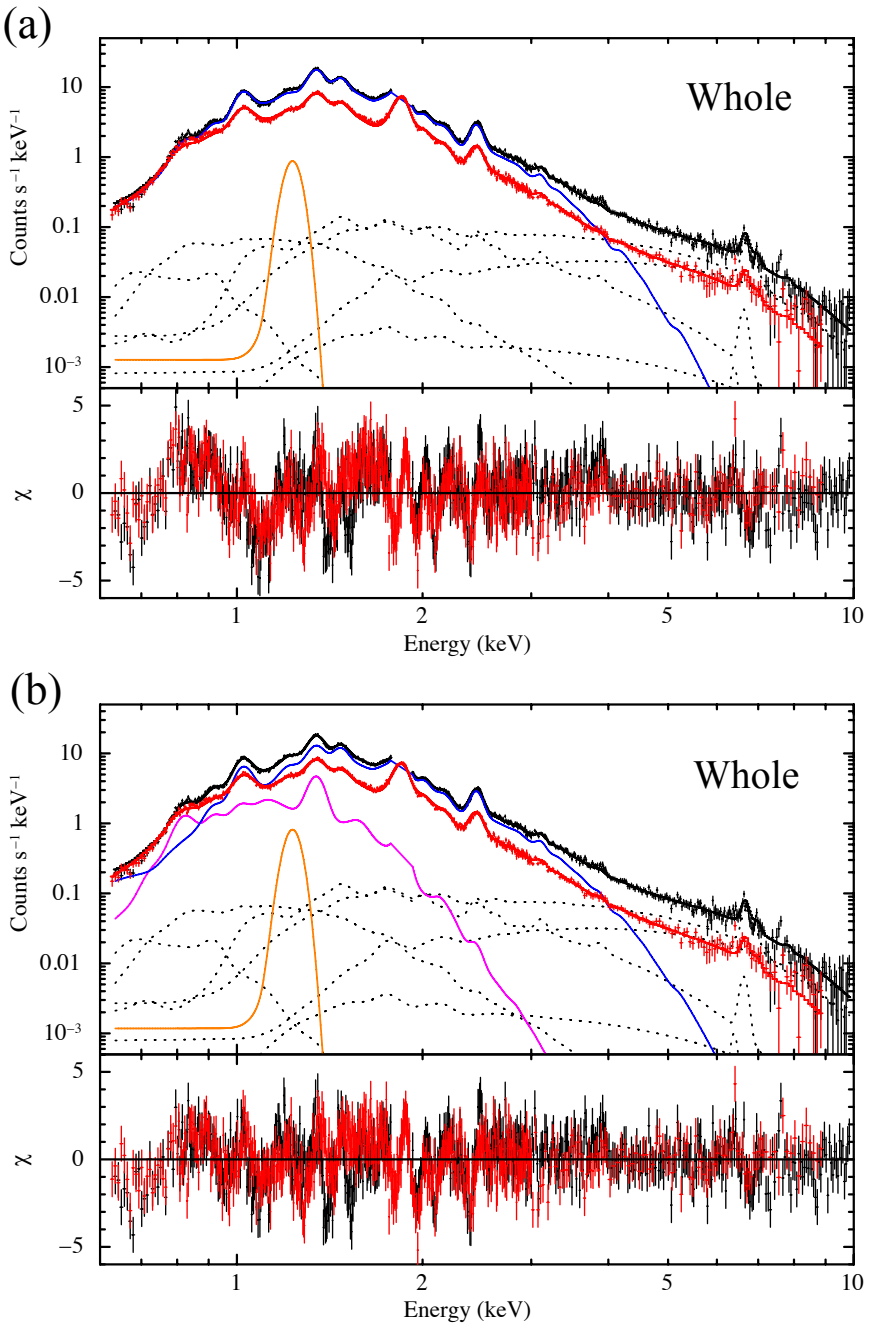

Figure 7.4: XIS0+3 (black crosses) and XIS1 (red crosses) spectra of the Whole region after NXB subtraction. The magenta, blue and orange solid lines denotes the SNR models for XIS0+3, consisting of the CIE, RP and Gaussian components, respectively. The dotted lines show the background model for XIS0+3.

Table 7.3: Best-fit model parameters of the spectrum in the Whole region.

Model function	Parameter	Whole (RP)	Whole (CIE+RP)
TBabs	$N_{\rm H}$ (10^{22} cm^{-2})	1.92 ± 0.01	$2.00\ ^{+0.02}_{-0.01}$
VVRNEI1	kT_e (keV)	————	0.22 ± 0.01
(CIE comp.)	$Z_{\rm O} = Z_{\rm Ne}$ (solar)	————	$0.26\ ^{+0.14}_{-0.12}$
	$Z_{\rm Mg}$ (solar)	————	$0.94\ ^{+0.10}_{-0.13}$
	Normalization†	————	$6.61^{+0.80}_{-1.42}$
VVRNEI2	kT_e (keV)	0.34 ± 0.01	0.37 ± 0.01
(RP comp.)	$kT_{\rm init}$ (keV)	0.97 ± 0.01	0.93 ± 0.02
	$Z_{\rm O} = Z_{\rm Ne}$ (solar)	1.3 ± 0.1	$3.6\ ^{+0.3}_{-0.2}$
	$Z_{\rm Mg}$ (solar)	1.6 ± 0.1	2.8 ± 0.1
	$Z_{\rm Si}$ (solar)	2.4 ± 0.1	$4.5\ ^{+0.2}_{-0.1}$
	$Z_{\rm S}$ (solar)	2.7 ± 0.2	$4.3\ ^{+0.2}_{-0.1}$
	$Z_{\rm Ar} = Z_{\rm Ca}$ (solar)	7.9 ± 0.9	$8.1\ ^{+1.2}_{-1.1}$
	$Z_{\rm Fe} = Z_{\rm Ni}$ (solar)	0.31 ± 0.31	< 0.19
	$n_e t$ (10^{11} s cm^{-3})	4.9 ± 0.1	$3.5\ ^{+0.2}_{-0.3}$
	Normalization†	3.14 ± 0.13	$1.23\ ^{+0.02}_{-0.04}$
Gaussian	Centroid (keV)	1.23 (fixed)	1.23 (fixed)
	Normalization‡	26 ± 2	$26\ ^{+2}_{-3}$
	χ^2_ν (ν)	2.31 (1227)	1.92 (1223)

† The emission measure integrated over the line of sight, i.e., $(1\ /\ 4\pi) \int n_e n_{\rm H} dl$ in units of 10^{18} cm^{-5} sr^{-1}.

‡ The unit is photons s^{-1} cm^{-2} sr^{-1}.

7.3.4 Hard X-ray sources

In the imaging analysis, we found the hard X-ray sources in regions A, B and C. For spectral analyses of the regions, we extracted spectra from each region and fitted them with the model accounting for the sum of the emissions from the hard X-ray source, SNR plasma, and X-ray background. Models for the hard X-ray sources are chosen based on the characteristics of their emissions as described below. We applied the models obtained in §7.3.2 for the X-ray background. For the SNR component, we used the best-fit model of the Whole spectrum in §7.3.3 but we allowed kT_e, $n_e t$, the Mg, Si, S, Ar and Fe abundances of the RP component, and the normalization to vary. In the spectral analysis of region 1 (§7.3.3), we found the residuals in the hard band so that we refitted the spectrum with the model including a hard component.

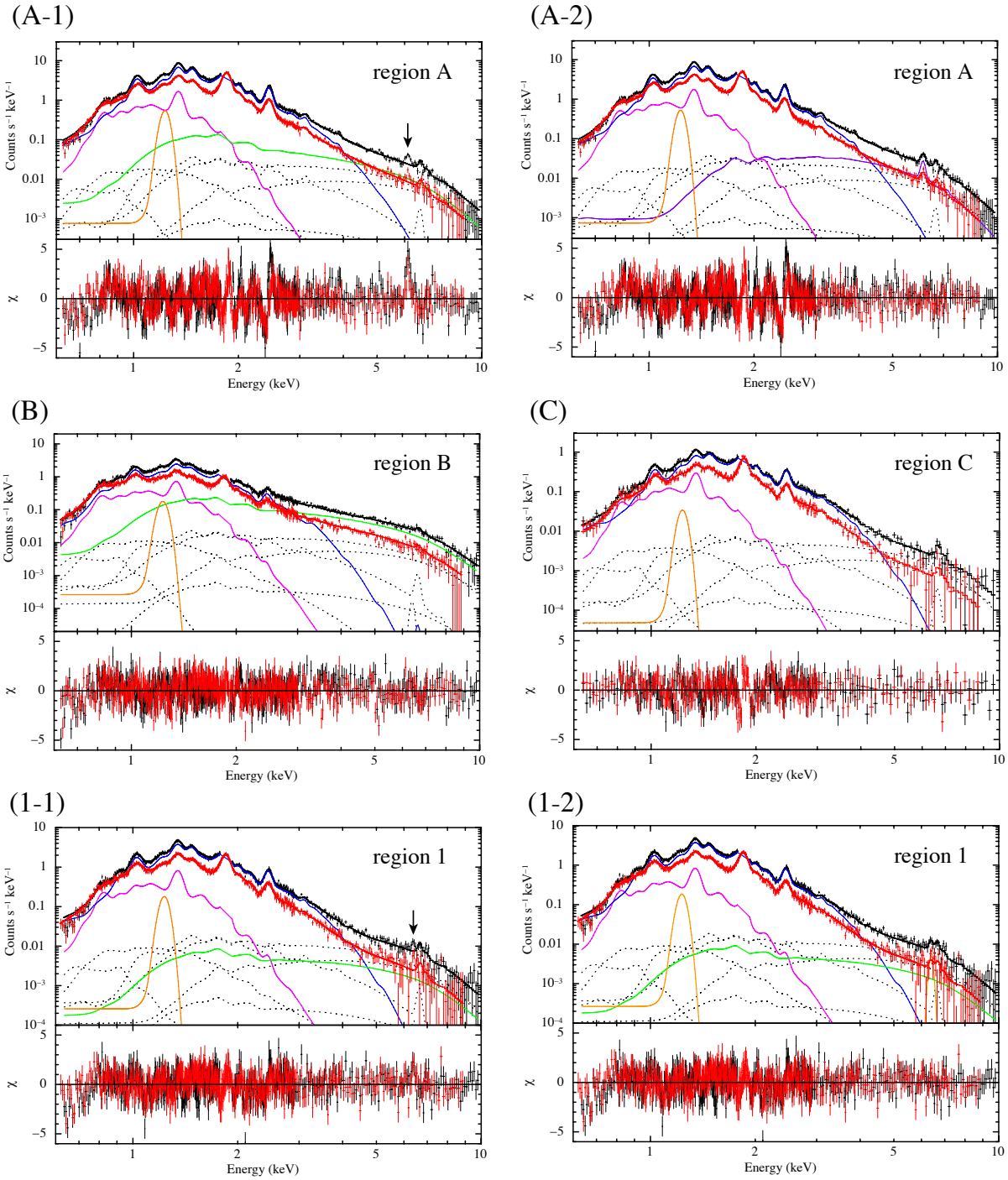

Figure 7.5: XIS0+3 (black crosses) and XIS1 (red crosses) spectra in the regions A, B, C and 1 of W44. Each spectrum is fitted with the model consisting of the SNR and background components. The solid and dotted lines show the SNR and background models of XIS0+3, respectively. The SNR model consists of CIE (magenta lines), RP (blue lines), power-law (green lines), APEC (purple line), and Gaussian (orange lines) components, respectively.

Table 7.4: Best-fit model parameters of the spectrum in the regions A, B, C and 1.

	Model function	Parameter	Region A (SNR+PL)	Region A (SNR+APEC)	Region B (SNR+PL)	Region C (SNR)	Region 1 (SNR+PL)	Region 1 (SNR+PL+Gauss)
SNR comp.	TBabs	$N_{\rm H}$ (10^{22} cm^{-2})	1.92 ± 0.01	1.94 ± 0.02	1.83 ± 0.03	$2.21^{+0.05}_{-0.04}$	1.97 ± 0.02	1.97 ± 0.02
	VVRNEI1	kT_e (keV)	0.21 ± 0.01	0.21 ± 0.01	0.22 ± 0.02	$0.22^{+0.01}_{-0.02}$	$0.23^{+0.02}_{-0.01}$	$0.23^{+0.02}_{-0.01}$
	(CIE comp.)	$Z_{\rm all}$ (solar)	$= Z_{\rm all,Whole}$	$= Z_{\rm all,Whole}$	$= Z_{\rm all,Whole}$	$= Z_{\rm all,Whole}$	$= Z_{\rm all,Whole}$	$= Z_{\rm all,Whole}$
		Normalization†	8.35 ± 1.04	$9.77^{+1.77}_{-1.56}$	$5.92^{+2.51}_{-2.40}$	$8.61^{+2.82}_{-3.16}$	$5.60^{+1.97}_{-1.51}$	$5.59^{1.99}_{-1.53}$
	VVRNEI2	kT_e (keV)	0.44 ± 0.01	0.45 ± 0.01	0.28 ± 0.01	$0.38^{+0.01}_{-0.02}$	$0.35^{+0.01}_{-0.02}$	$0.35^{+0.01}_{-0.02}$
	(RP comp.)	$kT_{\rm init}$ (keV)	0.93 (fixed)	0.93 (fixed)	0.93 (fixed)	0.93 (fixed)	0.93 (fixed)	0.93 (fixed)
		$Z_{\rm O} = Z_{\rm Ne}$ (solar)	3.6 (fixed)	3.6 (fixed)	3.6 (fixed)	3.6 (fixed)	3.6 (fixed)	3.6 (fixed)
		$Z_{\rm Mg}$ (solar)	3.1 ± 0.1	3.0 ± 0.1	$2.8^{+0.1}_{-0.2}$	$2.4^{+0.3}_{-0.2}$	3.4 ± 0.1	$3.4^{+0.1}_{-0.2}$
		$Z_{\rm Si}$ (solar)	5.9 ± 0.2	$5.7^{+0.2}_{-0.3}$	5.1 ± 0.3	$6.6^{+0.5}_{-0.3}$	$6.1^{+0.4}_{-0.3}$	$6.1^{+0.4}_{-0.3}$
		$Z_{\rm S}$ (solar)	5.4 ± 0.2	$5.1^{+0.4}_{-0.3}$	$5.3^{+0.8}_{-0.6}$	$5.8^{+0.6}_{-0.5}$	$6.5^{+0.6}_{-0.8}$	$6.5^{+0.6}_{-0.8}$
		$Z_{\rm Ar} = Z_{\rm Ca}$ (solar)	7.4 ± 0.7	$7.0^{+1.1}_{-1.0}$	$= Z_{\rm S}$	$10.0^{+3.2}_{-2.6}$	$14.6^{+5.4}_{-3.4}$	$14.8^{+5.8}_{-3.4}$
		$Z_{\rm Fe} = Z_{\rm Ni}$ (solar)	0.23 ± 0.03	$0.21^{+0.05}_{-0.06}$	$1.0^{+0.3}_{-0.2}$	< 0.19	< 0.06	< 0.05
		$n_e t$ (10^{11} s cm^{-3})	3.4 ± 0.1	3.3 ± 0.1	$4.9^{+0.3}_{-0.2}$	$2.4^{+0.2}_{-0.1}$	$4.0^{+0.3}_{-0.1}$	$4.0^{+0.2}_{-0.1}$
		Normalization†	1.65 ± 0.03	$1.73^{+0.03}_{-0.04}$	$1.73^{+0.14}_{-0.10}$	1.80 ± 0.09	2.29 ± 0.10	$2.29^{+0.15}_{-0.08}$
	Gaussian	Centroid (keV)	1.23 (fixed)	1.23 (fixed)	1.23 (fixed)	1.23 (fixed)	1.23 (fixed)	1.23 (fixed)
		Normalization‡	58 ± 4	57 ± 6	32 ± 7	23^{+16}_{-15}	39 ± 9	40^{+8}_{-10}
Hard X-ray comp.	TBabs	$N_{\rm H}$ (10^{22} cm^{-2})	$= N_{\rm H,\ SNR}$	$= N_{\rm H,\ CXB}$	$= N_{\rm H,\ SNR}$	———	$= N_{\rm H,\ SNR}$	$= N_{\rm H,\ SNR}$
	Power law	Photon index	2.48 ± 0.15	———	2.34 ± 0.08	———	$1.69^{+0.66}_{-0.88}$	$1.74^{+0.79}_{-0.74}$
		Normalization*	152 ± 37	———	405^{+52}_{-47}	———	12^{+18}_{-9}	11^{+31}_{-8}
	Gaussian	Centroid (keV)	———	———	———	———	———	6.40 (fixed)
		Normalization‡	———	———	———	———	———	$0.38^{+0.17}_{-0.18}$
	APEC	kT_e (keV)	———	$3.67^{+0.67}_{-0.46}$	———	———	———	———
		$Z_{\rm all}$ (solar)	———	$0.41^{+0.10}_{-0.07}$	———	———	———	———
		Redshift (z)	———	0.091 (fixed)	———	———	———	———
		Normalization†	———	$0.034^{+0.006}_{-0.007}$	———	———	———	———
		χ^2_ν (ν)	2.01 (1116)	1.93 (1115)	1.19 (1117)	1.26 (549)	1.37 (1098)	1.36 (1097)

† The emission measure integrated over the line of sight, i.e., $(1\ /\ 4\pi) \int n_e n_{\rm H} dl$ in units of 10^{18} cm^{-5} sr^{-1}.

‡ The unit is photons s^{-1} cm^{-2} sr^{-1}.

* The unit is photons s^{-1} cm^{-2} keV^{-1} sr^{-1} at 1 keV.

Region A

We first used a power-law model for the hard X-ray component. The fitting results are shown in Figure 7.5 (A-1) and the best-fit parameters are summarized in Table 7.4. The model gives a satisfactory fit in the 0.6–10 keV band except for the line-like residuals around 6.1 keV. We, therefore, added a Gaussian with its centroid energy treated as a free parameter. The fit with the Gaussian significantly improved the fitting and the centroid energy was determined to be 6.14 ± 0.02 keV. There are major atomic lines at this energy in the rest frame. The most probable explanation would be a redshifted Fe line. A promising candidate of a redshifted Fe line emitter is an active galactic nucleus or a galaxy cluster. The hard X-ray source (Figure 7.1c) is clearly extended, and therefore, most likely is a galaxy cluster. Considering of the typical temperature and ionization state of a plasma in a galaxy cluster, the line should be Fe Heα at 6.70 keV. Then, the redshift is estimated to be $z = 0.091$ which is consistent with the galaxy cluster explanation.

An X-ray emission from a galaxy cluster is generally reproduced by a CIE model. Therefore, we adopted the APEC model as the hard component. The absorption column density was fixed at the total Galactic absorption in the line of sight toward W44. The model gave a satisfactory fit (Figure 7.5 (A-2) and Table 7.4). The abundance and kT_e of the galaxy cluster were determined to be $0.41^{+0.10}_{-0.07}$ and $3.67^{+0.67}_{-0.46}$ keV, respectively. The flux is 1.6×10^{-12} ergs cm^{-2} s^{-1} at 0.5–2.0 keV. By systematically analyzing of ROSAT data of a number of galaxy clusters, Fairley et al. (2000) reported relationship between the bolometric luminosity (L) and electron temperature (kT_e). The obtained flux of the hard X-ray source can be translated into a luminosity of 5.6×10^{43} erg s^{-1} with the Hubble constant of 50 km s^{-1} Mpc^{-1} assumed by Fairley et al. (2000). We converted the 0.5–2.0 keV flux to the bolometric luminosity by multiplying a factor of 2–3 (Fairley et al., 2000), and obtained $L = (1.1\text{–}1.7) \times 10^{43}$ erg s^{-1}. The obtained L and kT_e are consistent with the L-kT_e relationship by Fairley et al. (2000) as shown in Figure 7.6. We, therefore, conclude that the hard X-ray source in region A is a background galaxy cluster.

Region B

We fitted the spectrum in region B with the model composed of the SNR, background and power-law components. The spectrum can be reproduced well by the model as in Figure 7.5 (B) and Table 7.4. The photon index and flux at 2–10 keV are 2.34 ± 0.08 and 4.0×10^{-12} ergs cm^{-2} s^{-1}, respectively. The photon index is consistent with that of the PWN measured by Chandra (Petre et al., 2002), whereas the flux is an order of magnitude higher than their measurement. The Suzaku image of the hard emission spreads more than the PWN image with Chandra. Our result suggests that the PWN is spatially extended more than previously known through the Chandra observation (Petre et al., 2002).

Region C

We performed a spectral analysis of region C and found that the spectrum can be well reproduced by a model composed of the SNR and background components (Figure 7.5 (C) and Table 7.4). Therefore, we conclude that no additional hard X-ray component is necessary for this region.

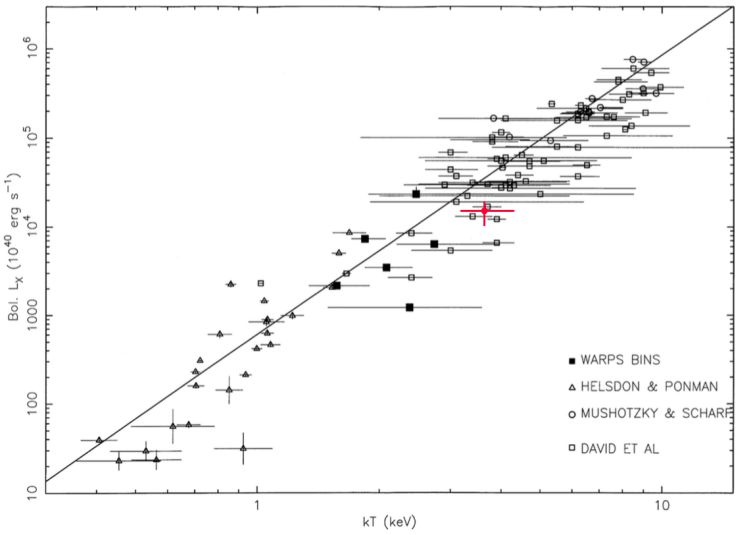

Figure 7.6: L–kT_e relation for $z < 0.2$ (Fairley et al., 2000). The black plots represent groups of galaxy clusters from the Wide Angle ROSAT Pointed Survey (WARPS) bins, Helsdon & Ponman (2000), Mushotzky & Scharf (1997) and David et al. (1993). The line shown is the best-fitting line to clusters with $kT_e > 1$ keV, $L \propto {kT_e}^{3.15}$. The red plot indicate the galaxy cluster discovered by us.

Region 1

The spectrum of region 1 was refit with a model with a power-law component in addition to the SNR and background components. Figure 7.5 (1-1) and Table 7.4 show the fitting results. The spectra can be mostly reproduced by the model but residuals around 6.4 keV are evident (see Figure 7.7). The residuals was improved by the Gaussian whose centroid energy is 6.38±0.04 keV, which corresponds to the energy of the neutral or low ionized Fe Kα line. However, a low-ionized Fe line is unlikely since Fe ions in middle-aged SNRs such as W44 are expected to be highly ionized. The line is most probably from neutral Fe. One of the plausible processes to emit the line is K-shell ionization of Fe atoms in dense cloud by electrons or protons accelerated in the SNR. Such scenarios are proposed to explain the neutral Fe Kα line from the Galactic ridge (Nobukawa et al., 2015) as well as from the SNR 3C391 (Sato et al., 2014) and Kes 79 (Sato et al., 2016). Following them, we fitted the spectrum with the model consisting of the SNR, background, power-law components and a Gaussian whose centroid energy was fixed at the line energy of the neutral Fe (6.40 keV). The fit improved the residuals around 6.4 keV as shown in Table 7.4 and Figures 7.5 (1-2) and 7.7. The improvement is significant with the F-test null probability of 1.9×10^{-3}.

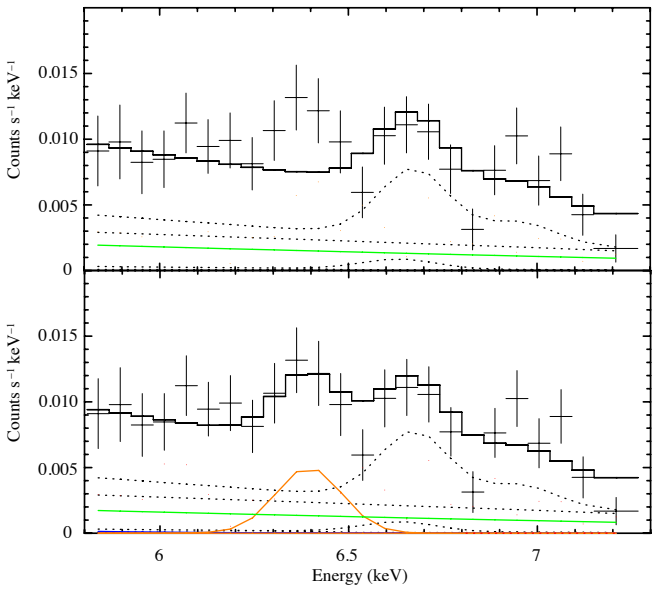

Figure 7.7: XIS0+3 spectra from region 1 in the energy band of 5.8–7.3 keV with the model same as that in (Top) Figure 7.5 (1-1) and (Bottom) Figure 7.5 (1-2).

7.4 Discussion on W44

In Figure 7.8, we show the maps of $N_{\rm H}$, kT_e of the CIE component, kT_e and $n_e t$ of the RP component, and normalization ratio of the CIE to the RP components in each region. We also show the synchrotron and CO radio images and the locations of the 1720 MHz OH maser emissions in the figure.

7.4.1 Ambient gas and X-ray absorption

As shown in Figure 7.8a, our spectral analysis has revealed the spatial distribution of the X-ray absorption column densities ($N_{\rm H,X}$). We compare the $N_{\rm H,X}$ distribution with that of the ambient gas traced by radio line emissions. The location with higher $N_{\rm H,X}$ coincides with the ^{12}CO(J = 2–1) line in the 40–50 km s^{-1} range, indicating that the cloud is located in front of the remnant. The area-weighted average of $N_{\rm H,X}$ of regions 3, 8, and C, where the ^{12}CO(J = 2–1) line emission is detected, is calculated to be 2.18×10^{22} cm^{-2}. On the other hand, the average across the other regions is 1.96×10^{22} cm^{-2}. The difference of the two should correspond to the column density of the cloud responsible for the ^{12}CO(J = 2–1) line. The column density of the molecular cloud was estimated by Seta et al. (2004) at $\sim 4 \times 10^{21}$ cm^{-2} with the Nobeyama 45m radio telescope. It is almost the same as the $N_{\rm H,X}$ difference, supporting the suggestion that the cloud is located in front of the remnant.

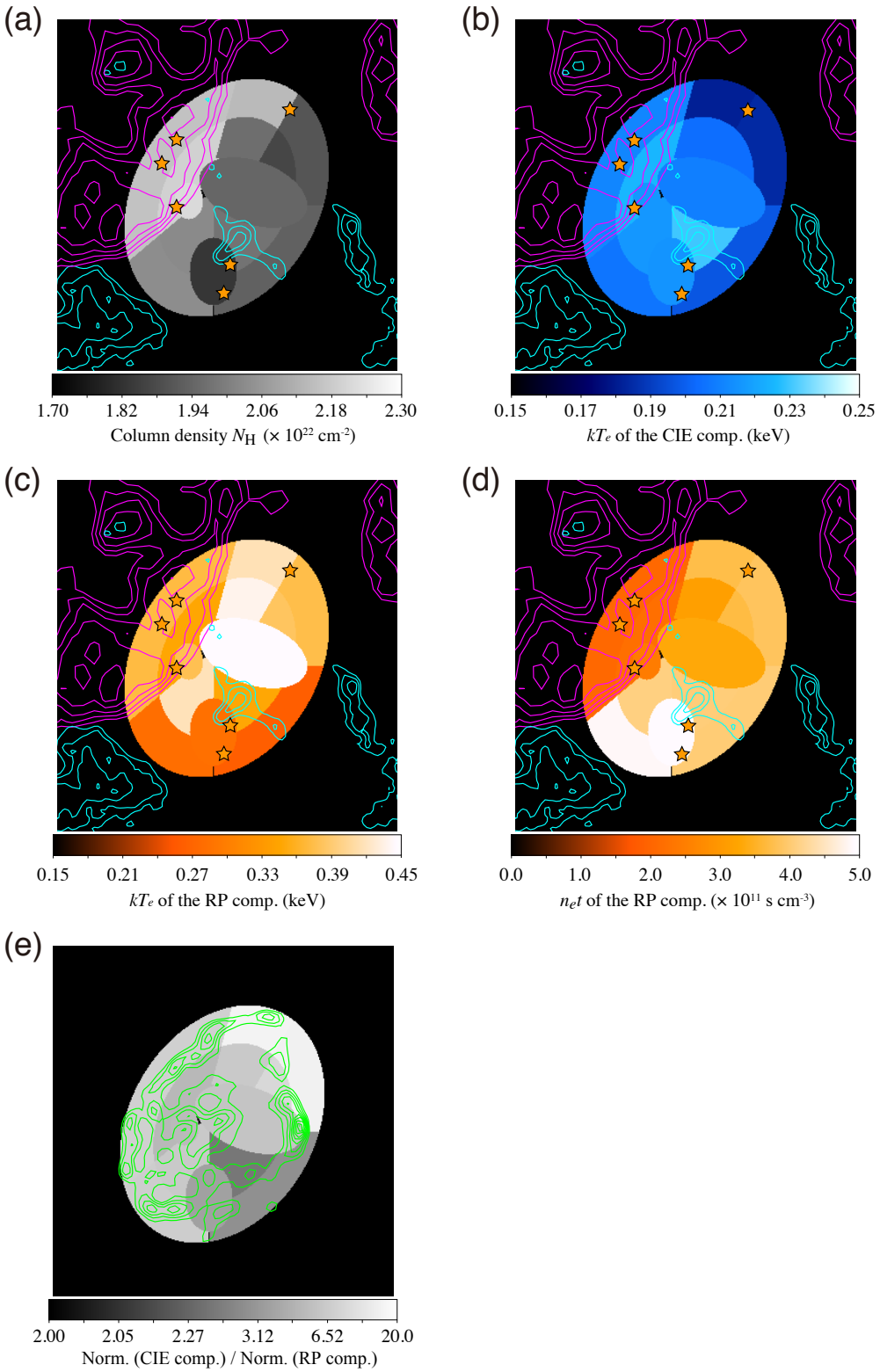

Figure 7.8: Maps of (a) $N_{\rm H}$, (b) kT_e of the CIE component, (c) kT_e of the RP component, (d) $n_e t$ of of the RP component and (e) the normalization ratio of the CIE to RP components, respectively. In panel (a–d), we overlaid the ^{12}CO($J = 2$–1) images in the velocity range of 40–50 km s^{-1} (magenta contours) and 50–60 km s^{-1} (cyan contours) obtained with the NANTEN2 (Uchida et al., 2012). The orange stars indicates the locations of the 1720 MHz OH maser emissions (Claussen et al., 1997). The green contours in panel (e) are a radio image as seen in 20 cm wavelength by the VLA (Helfand et al., 2006).

7.4.2 Origin of the CIE plasma

In the spectral analysis, we found that the SNR plasma emissions in the whole remnant are well reproduced by the model consisting of the CIE and RP components. Most of the abundances of the CIE component are close to solar (0.9–1.0), suggesting that the origin is a shocked ISM. Figure 7.8e shows the distribution of the normalization ratios of the CIE to RP components. At each azimuthal direction, the ratio is higher in the outer regions, indicating that the CIE plasma dominants in the rim. The results of W44 are the same as those of IC 443 (Chapter 6), and further support the shocked ISM origin for the CIE component.

7.4.3 Origin of the recombining plasma

In the spectral analysis, we found that the electron temperatures of the RPs in the central part of the remnant (regions A and 4) are higher than those in the other regions (Figure 7.8c). In the thermal conduction scenario, the SNR plasma is cooled by a molecular cloud as already discussed in Chapters 5 and 6. The intensity ratio of the ^{12}CO($J = 2$–1) to ^{12}CO($J = 1$–0) emissions (Figure 7.9: Yoshiike, 2017) is distributed in regions excluding these central regions, implying the interaction between the SNR shock and the molecular cloud only in the outer regions. The OH maser emissions (Claussen et al., 1997) also support the picture. The lower kT_e in the outer regions than those in regions A and 4 can be explained by the thermal conduction between the plasma and the interacting molecular cloud if the plasmas in the central regions are not cooled completely until the conduction.

The spectral analysis also revealed that $n_e t$ of the eastern part of the remnant is lower than those of the other regions (Figure 7.8d). The regions with the lower $n_e t$ coincides with the location of the molecular cloud indicated by the ^{12}CO($J = 2$–1) emission. Assuming that the electron density of the RP is uniform, we consider that the SNR shock recently started to interact with the molecular cloud. In the southern part of W44, $n_e t$ is higher than those of the plasma in the other regions (Figure 7.8d), suggesting that the shock-cloud interaction started in the early phase of the SNR evolution. If this is the case, the lower kT_e of the RP in the south can be explained as well. On the other hand, Uchida et al. (2012) claimed that a conduction timescale is much longer than the SNR age, and thus the thermal conduction scenario is unlikely. We discuss the conduction timescale later in §9.3.

Let us try to explain the observed $n_e t$ distribution in the context of the alternative scenario, the rarefaction scenario. Shimizu et al. (2012) carried out 3D-hydrodynamical calculations for the interaction of expanding supernova ejecta with the CSM and the ISM outside and concluded that the CSM radius needs to be smaller than 1 pc. Since the W44 radius of ~ 10 pc is much larger than 1 pc, we suppose that the shock broke out of the CSM in the early phase of the SNR evolution. Since the time before the break from the CSM is much shorter than that after the break, we can regard that the rarefaction occurred almost at the same time independent of the location. It is not easy to explain the spatial dependence of $n_e t$ in W44.

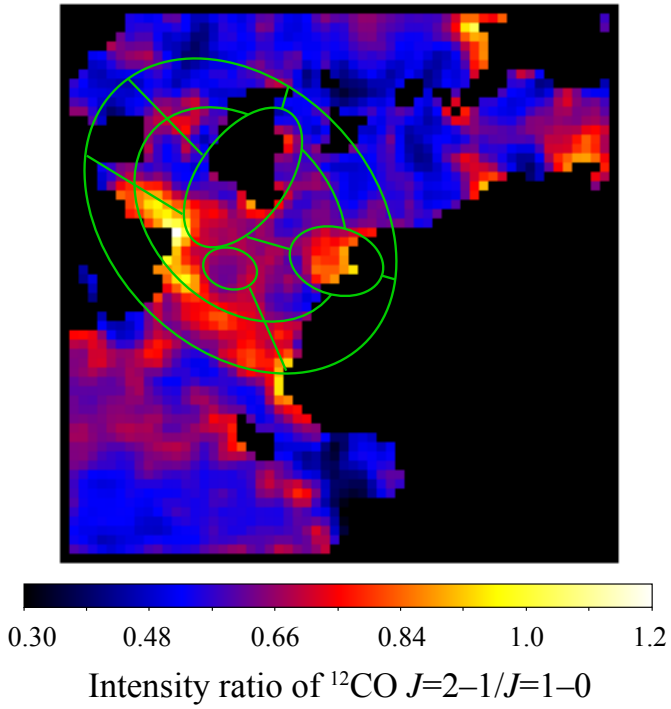

Figure 7.9: Spatial distribution of the intensity ratio of the ^{12}CO(J = 2–1) to ^{12}CO(J = 1–0) emissions in the velocity range of 30–40 km s^{-1} with the NANTEN2 observations (Yoshiike, 2017). The solid green lines show the regions used for the spectral analysis.

Chapter 8

W49B

8.1 Previous Works and Our Aims

W49B (G43.3−0.2) is a mixed-morphology SNR with center-filled X-ray emissions and a radio shell (Pye et al., 1984) and is located at $\sim$ 8 kpc (Radhakrishnan et al., 1972; Moffett & Reynolds, 1994). The age was estimated at $\sim$ 6000 yr (Smith et al., 1985), which is one of the youngest mixed-morphology SNRs. Most of the mixed-morphology SNRs are interacting with atomic or molecular gas. W49B is one of such remnants. Based on infrared observations, Keohane et al. (2007) claimed that shocked molecular hydrogens are associated with eastern and southwestern parts of W49B (Figure 8.1). A CO observation revealed a molecular cloud in the southwest (Figure 8.2: Simon et al., 2001). In the western part of the remnant, GeV gamma rays were found by Abdo et al. (2010) and H. E. S. S. Collaboration et al. (2016) with Fermi-LAT as shown in Figure 8.3. TeV gamma rays were also detected in W49B by H. E. S. S. Collaboration et al. (2016). If the origin of the gamma-ray emissions is π^0 decays, the results also provide a hint of the shell-cloud interaction.

Kawasaki et al. (2005) observed W49B with ASCA and measured ionization temperatures. They found that kT_z of $\sim$ 2.5 keV is higher than kT_e of $\sim$ 1.8 keV, indicating that the W49B plasma is overionized. Ozawa et al. (2009b) analyzed Suzaku data and found a strong Fe RRC and cascade lines which is robust evidence for the presence of RP in W49B. Lopez et al. (2013b) performed a spatially resolved spectroscopy with Chandra and measured intensity ratios of Si Lyα/Si Heα and Ar Lyα/Ar Heα in each region. They claimed that the degree of ionization becomes higher from east to west, with more ionized plasma toward the west of the remnant.

The previous X-ray studies applied phenomenological models consisting of a CIE component, Gaussians and RRCs for spectral fits (Kawasaki et al., 2005; Ozawa et al., 2009b; Lopez et al., 2013b). We here adopted a more realistic model, VVRNEI, in order to extract more accurate physical parameters. All spectral fits are performed with XSPEC version 12.9.0n and the plasma models are calculated with ATOMDB version 3.0.8. We used solar abundances given by Wilms et al. (2000).

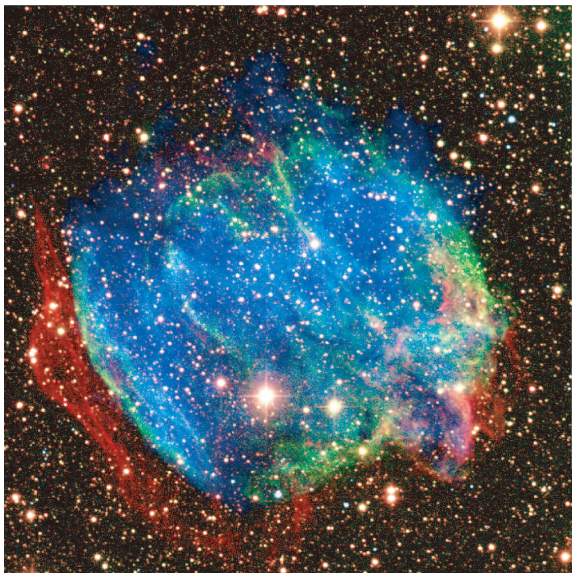

Figure 8.1: X-ray emission (blue), 2.12 μm shocked molecular hydrogen (red) and 1.64 μm [FeII] (green) images of W49B. The K_s-band image of foreground and background stars is overlaid in white. The figure is taken from Keohane et al. (2007).

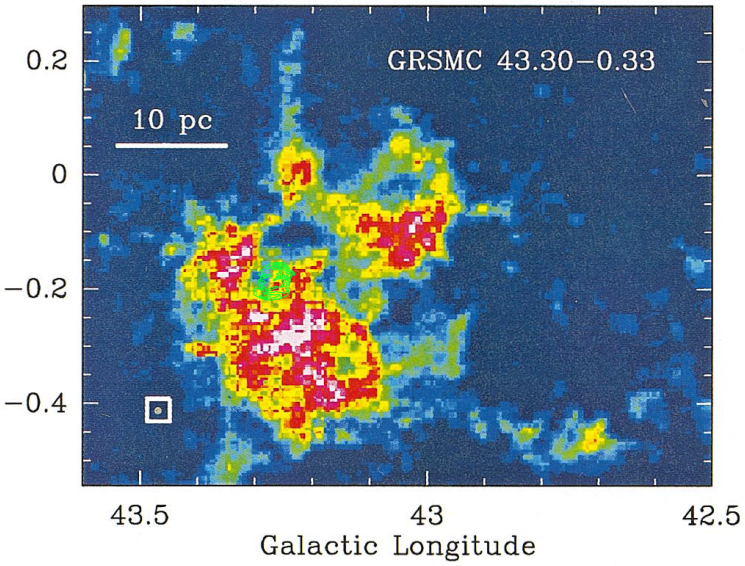

Figure 8.2: ^{13}CO(J = 1–0) integration intensity from 0.5 to 9.7 K km s^{-1} with the Milky Way Galactic Ring Survey, a Boston University and Five College Radio Astronomy Observatory collaboration (Simon et al., 2001). The green contours indicate the radio intensity of W49B obtained at a wavelength of 20 cm with the Multi-Array Galactic Plane Imaging Survey (MAGPIS; Helfand et al., 2006).

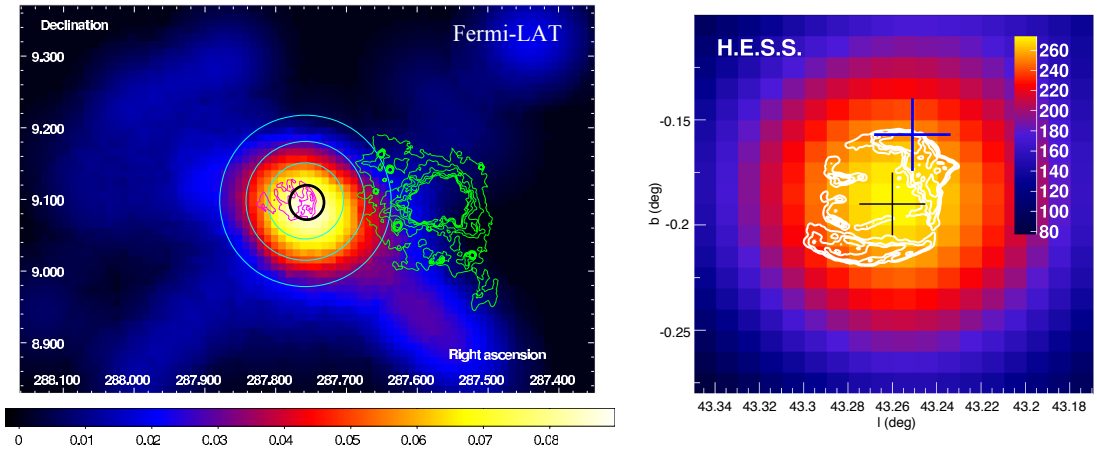

Figure 8.3: (Left) Fermi-LAT counts map in units of counts per pixel in the 6–30 GeV band taken from Abdo et al. (2010). The LAT localization is represented by a black circle with a radius of $0°.024$ (90% confidence level) centered at $(\alpha, \delta) = (287°.756, 9°.096)$. The magenta and green contours indicate W49B and W49A in the Spizer IRAC 5.8 μm, respectively. (Right) Gamma-ray excess map of W49B with the H.E.S.S. taken from H. E. S. S. Collaboration et al. (2016). The crosses show the best-fit centroid positions of gamma-ray signal with the H.E.S.S. ($\geq$ 600 GeV; black) and Fermi-LAT ($\geq$ 1 GeV; blue). The size of the crosses represents the size of the 95% confidence level contours, including systematic uncertainties. The while contours show the radio intensity obtained at a wavelength of 20 cm with the MAGPIS.

8.2 Suzaku Observations and Data Reduction

Table 8.1 summarizes the Suzaku observation log of W49B. We used data from the XIS excluding XIS2 because of the malfunction described in §4.3.1. We reduced the data and estimated NXBs with the same method in Chapter 6. As already explained in §4.3.3, we corrected the gains of each sensor.

Table 8.1: Suzaku observation log of W49B.

Target	Obs. ID	Obs. date	(R.A., Dec.)	Exposure
W49B	503084010	2009-03-29	($19^{\rm h}11^{\rm m}08^{\rm s}.3$, $9°06'56''.5$)	52 ks
W49B	504035010	2009-03-31	($19^{\rm h}11^{\rm m}08^{\rm s}.3$, $9°06'55''.8$)	62 ks

8.3 Analysis

8.3.1 Image

Figure 8.4 shows an XIS3 image of W49B in the energy band of 0.3–10.0 keV. We subtracted the NXB from the image and corrected for the vignetting effect of the XRT. The image shows a center-filled morphology, where the peak of the X-ray emission is offset toward the east.

As shown in Figure 8.5, we present XIS3 images of W49B in the soft band (0.3–5.0 keV) and the hard band (5.0–10.0 keV), which cover emission lines of Ne to Ca and Cr to Ni, respectively. We found that the hard band image is more compact than the soft band one. If the images reflect the distribution of the elements, the result suggests that the distribution of the heavier element is center-filled whereas that of the lighter elements is more extended. The distributions are consistent with the onion-like structure (§2.1) that heavier elements tend to be produced closer to the center of the progenitor.

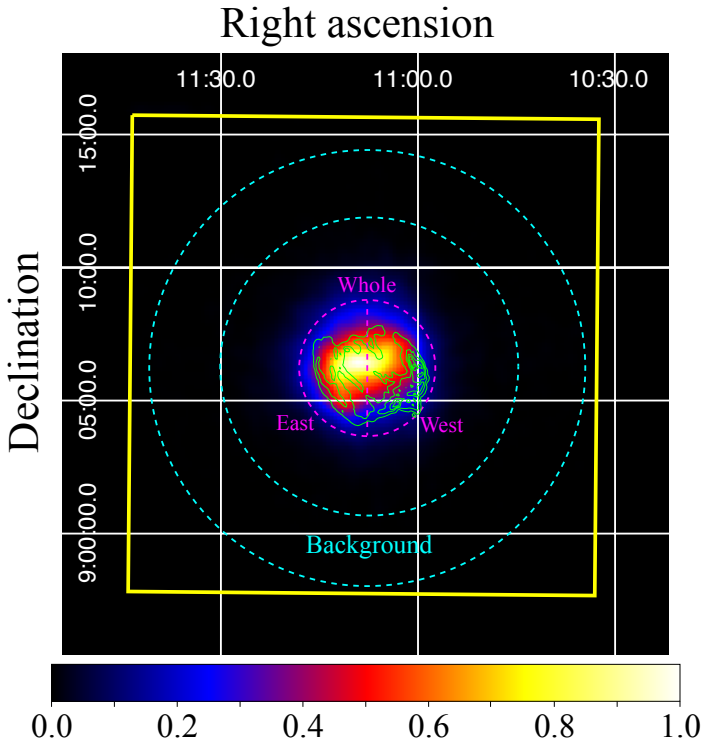

Figure 8.4: XIS3 image of W49B in the 0.3–10 keV band after NXB subtraction and correction of the vignetting effect. The yellow square indicates the FOV of the XIS. The magenta and cyan dotted lines show the source and background regions for the spectral analysis, respectively. The X-ray count rates are normalized so that the peaks become unity. The green contours are the radio intensity obtained at a wavelength of 20 cm with the MAGPIS. The coordinate refers to the J2000.0 epoch.

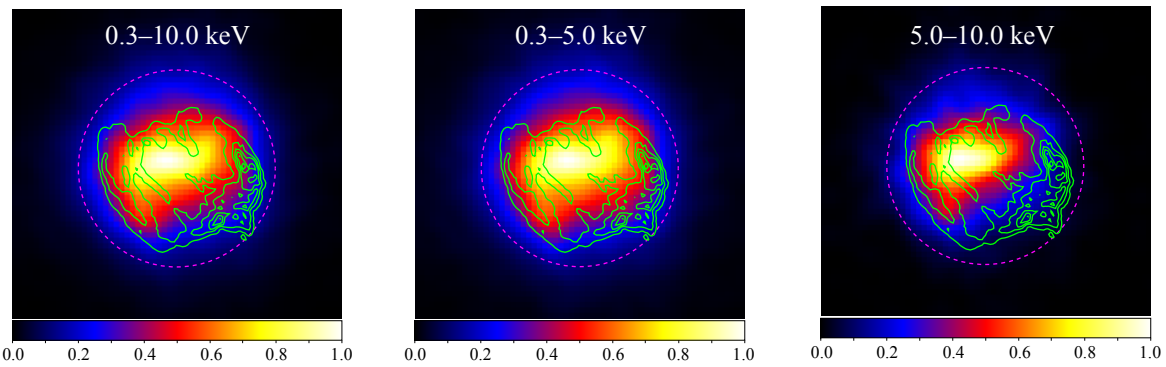

Figure 8.5: Same as Figure 8.4 but in the energy bands of 0.3–5.0 keV (Left) and 5.0–10.0 keV (Right).

8.3.2 SNR spectra

For the spectral analysis, we extracted source and background spectra from the Whole and Background regions shown in Figure 8.4. We subtracted the background spectrum from the source spectrum. Figure 8.6 shows the XIS0+3 spectrum. One can clearly see the emission lines of Mg, Si, S, Ar, Ca, Cr, Mn, Fe and Ni. The strong cascade lines and RRC of Fe are also detected, suggesting that the plasma is in a recombination-dominant state.

We first applied an RP model for the spectrum by using the VVRNEI model multiplied by the absorption model, TBabs. The abundances of Mg, Si, S, Ar, Ca, Cr, Mn, Fe, and Ni were allowed to vary, whereas the others were fixed to solar. We also allowed kT_e, $kT_{\rm init}$, n_et and the normalization to vary. For the XIS0+3 spectrum, we ignored the energy band around Si K-edge because of the known calibration uncertainty. We used the XIS1 spectrum in the energy band below 6.8 keV because of the higher NXB level. Figure 8.7a and Table 8.2 show the fitting results. The fit left residuals around the low-energy band of $\lesssim 2$ keV, indicating that the ionization degree of Si is significantly lower than the other elements. Therefore, we tried a CIE component for the low-energy band as we did for the spectral analyses of IC 443 and W44 in Chapters 6 and 7. For the CIE component, the normalization and kT_e were free parameters. We first fixed the abundances of all the elements to solar, but residuals around the Mg Kα line appeared. Thus, we allowed the Mg abundance to vary. The best-fit model and parameters are presented in Figure 8.7b and Table 8.2, respectively. The additional CIE component improved the residuals due to the discrepancy of the ionization degrees between Si and the other elements. However, residuals in the hard band above 6 keV are still significant, which implies even higher ionization degree for the plasma emitting the Fe lines and RRC.

We, therefore, divided the RP into two components ($\rm RP_L$ and $\rm RP_H$). For the $\rm RP_L$ model, we allowed the abundances of Mg, Si, S, Ar, and Ca to vary. The abundances of the heavier elements ($\geq$ Cr) were fixed at zero. The other abundances were fixed to solar. We also allowed kT_e, $kT_{\rm init}$, n_et and the normalization to vary. For the $\rm RP_H$ model, the abundances of Cr, Mn, Fe, and Ni were allowed to vary. The abundances of the lighter elements were fixed at zero, and those of the other abundances were fixed to solar. The normalization of $\rm RP_H$ was linked to that of $\rm RP_L$, whereas kT_e, $kT_{\rm init}$ and n_et were allowed

to vary. We fitted the Whole spectrum with the model consisting of the CIE and two RP components, and found that the spectrum can be reproduced by the model as shown in Figure 8.7c and Table 8.2.

Considering of the shell-cloud interaction suggested by the infrared 2.12 μm line emission (Figure 8.1), we extracted spectra from the East and West regions shown in Figure 8.4 in order to examine possible influences of the interaction on the characteristics of the X-ray emitting plasma. We adopted the same model as the Whole fit with $kT_{\rm init}$ of the $\rm RP_L$ component fixed at the best-fit value of the Whole fit. The model well fitted the spectra (Figures 8.7d and 8.7e; Table 8.2).

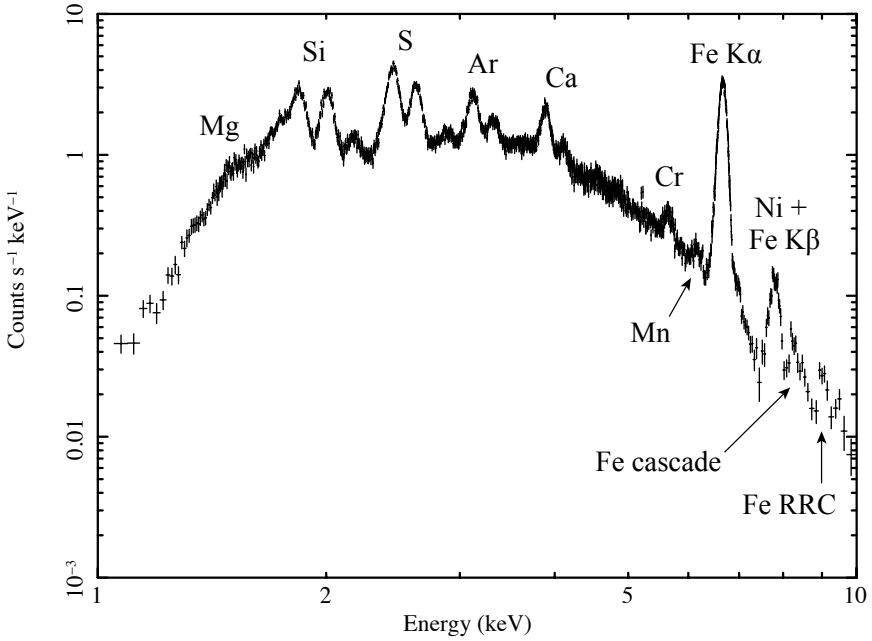

Figure 8.6: XIS0+3 spectrum of the Whole region after subtracting the background and NXB spectra.

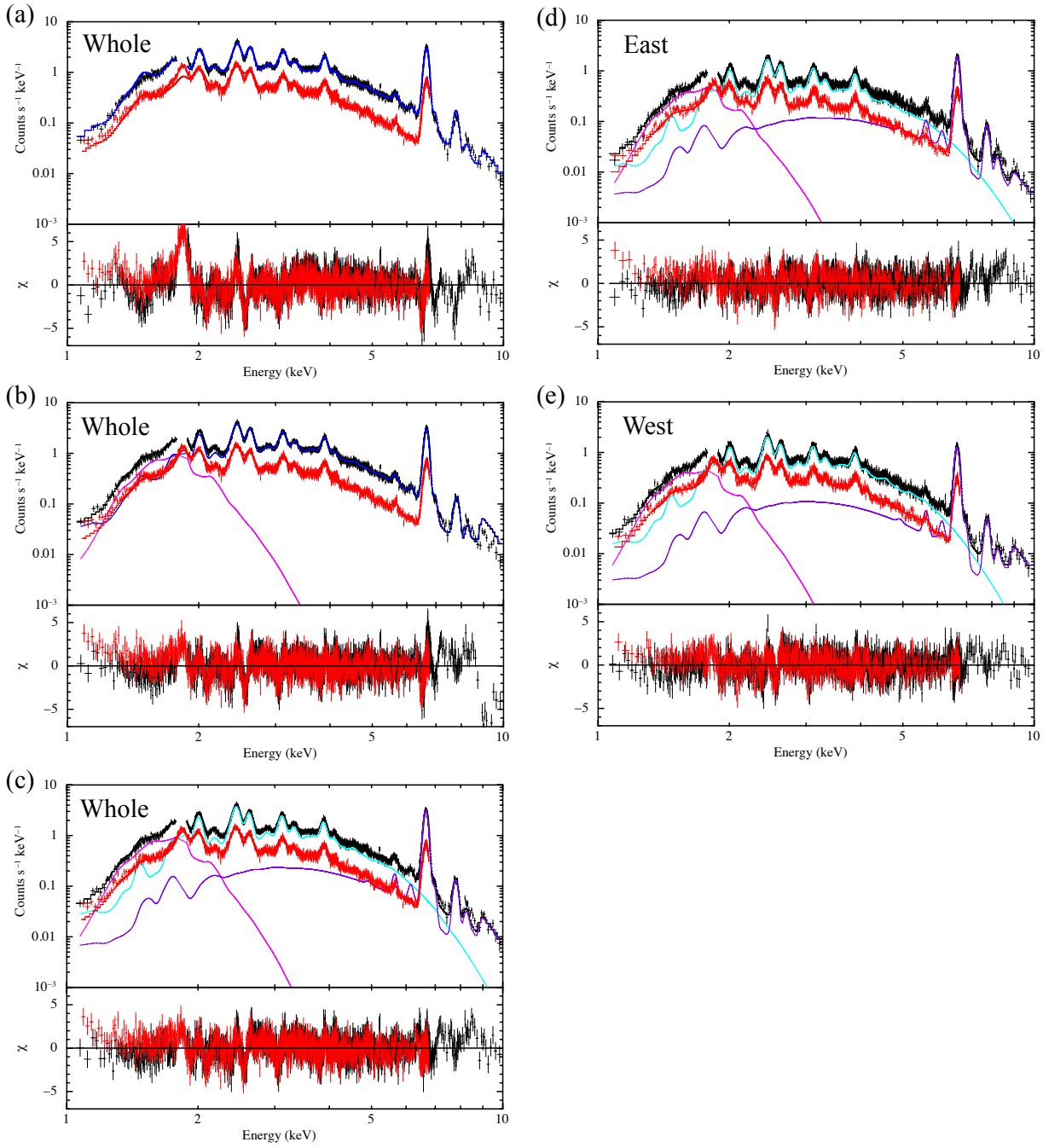

Figure 8.7: XIS0+3 (black crosses) and XIS1 (red crosses) spectra extracted from the Whole (a–c), East (d) and West (e) regions. The magenta, blue, cyan and purple lines indicate the models of CIE, RP (all elements), RP (light elements) and RP (heavy elements), respectively.

Table 8.2: Best-fit model parameters of the W49B spectrum.

Model function	Parameter	Whole (RP)	Whole (CIE+RP)	Whole (CIE+2RP)	East (CIE+2RP)	West (CIE+2RP)
TBabs	$N_{\rm H}$ (10^{22} cm^{-2})	7.34 ± 0.05	9.68 ± 0.07	$9.22^{+0.10}_{-0.12}$	$9.23^{+0.20}_{-0.15}$	$9.25^{+0.07}_{-0.16}$
VVRNEI1	kT_e (keV)	————	0.174 ± 0.001	$0.170^{+0.003}_{-0.004}$	$0.175^{+0.002}_{-0.007}$	$0.161^{+0.007}_{-0.005}$
(CIE comp.)	$Z_{\rm Mg}$ (solar)	————	0.20 ± 0.07	$0.17^{+0.09}_{-0.08}$	0.17 ± 0.12	$0.16^{+0.10}_{-0.09}$
	$Z_{\rm other}$ (solar)	————	1 (fixed)	1 (fixed)	1 (fixed)	1 (fixed)
	Normalization[‡]	————	1.1 ± 0.1	$1.1^{+0.3}_{-0.1}$	$0.9^{+0.2}_{-0.1}$	1.7 ± 0.5
VVRNEI2	kT_e (keV)	1.36 ± 0.02	1.00 ± 0.01	0.94 ± 0.02	$1.05^{+0.04}_{-0.07}$	$0.81^{+0.02}_{-0.01}$
(RP$_{\rm L}$ comp.)	$kT_{\rm init}$ (keV)	8.3 ± 0.4	6.2 ± 0.1	$5.9^{+1.4}_{-0.9}$	5.9 (fixed)	5.9 (fixed)
	$Z_{\rm Mg}$ (solar)	3.6 ± 0.4	16 ± 4	6.1 ± 1.4	$8.0^{+3.1}_{-2.4}$	4.6 ± 1.5
	$Z_{\rm Si}$ (solar)	5.4 ± 0.2	21 ± 4	$7.0^{+0.8}_{-0.7}$	$7.7^{+1.3}_{-1.0}$	$6.6^{+1.0}_{-0.9}$
	$Z_{\rm S}$ (solar)	5.2 ± 0.2	19 ± 3	$6.8^{+0.7}_{-0.5}$	$7.7^{+1.1}_{-0.8}$	6.3 ± 0.8
	$Z_{\rm Ar}$ (solar)	6.4 ± 0.2	20 ± 3	$7.5^{+0.7}_{-0.6}$	$8.3^{+1.3}_{-1.0}$	$6.8^{+0.9}_{-0.8}$
	$Z_{\rm Ca}$ (solar)	9.6 ± 0.3	24 ± 4	$9.1^{+0.6}_{-0.8}$	$10.7^{+1.3}_{-1.1}$	$8.1^{+1.1}_{-1.0}$
	$n_e t$ (10^{11} s cm^{-3})	7.7 ± 0.2	5.3 ± 0.2	4.4 ± 0.1	$5.6^{+0.5}_{-0.3}$	5.1 ± 0.1
	Normalization[†]	0.6 ± 0.1	0.4 ± 0.1	1.1 ± 0.1	0.8 ± 0.1	1.4 ± 0.2
VVRNEI3	kT_e (keV)	$= kT_{e,\ \rm VVRNEI2}$	$= kT_{e,\ \rm VVRNEI2}$	$1.46^{+0.01}_{-0.08}$	$1.66^{+0.07}_{-0.11}$	$1.26^{+0.02}_{-0.09}$
(RP$_{\rm H}$ comp.)	$kT_{\rm init}$ (keV)	$= kT_{\rm init,\ \rm VVRNEI2}$	$= kT_{\rm init,\ \rm VVRNEI2}$	$3.26^{+0.01}_{-0.10}$	$3.15^{+0.02}_{-0.12}$	3.37 ± 0.11
	$Z_{\rm Cr}$ (solar)	20 ± 1	40 ± 7	7.7 ± 1.2	$10.7^{+2.5}_{-2.0}$	5.2 ± 1.1
	$Z_{\rm Mn}$ (solar)	13 ± 2	35 ± 7	7.6 ± 1.4	$11.4^{+3.6}_{-1.6}$	$4.6^{+1.0}_{-1.1}$
	$Z_{\rm Fe}$ (solar)	7.7 ± 0.3	23 ± 4	3.0 ± 0.3	$4.2^{+0.8}_{-0.4}$	$1.9^{+0.3}_{-0.2}$
	$Z_{\rm Ni}$ (solar)	49 ± 3	85 ± 18	$5.3^{+1.2}_{-1.0}$	$7.1^{+1.8}_{-1.2}$	$3.6^{+1.1}_{-1.0}$
	$n_e t$ (10^{11} s cm^{-3})	$= n_e t$ VVRNEI2	$= n_e t$ VVRNEI2	< 0.9	< 0.2	< 0.4
	Normalization[†]	= Norm. VVRNEI2	= Norm. VVRNEI2	= Norm. VVRNEI2	= Norm. VVRNEI2	= Norm. VVRNEI2
	χ^2_ν (ν)	2.63 (2357)	1.96 (2354)	1.59 (2351)	1.33 (2028)	1.35 (2043)

[‡] The emission measure integrated over the line of sight, i.e., $(1\ /\ 4\pi) \int n_e n_{\rm H} dl$ in units of 10^{22} cm^{-5} sr^{-1}.

[†] The emission measure integrated over the line of sight, i.e., $(1\ /\ 4\pi) \int n_e n_{\rm H} dl$ in units of 10^{19} cm^{-5} sr^{-1}.

8.4 Discussion on W49B

We fitted the wide band spectra (1–10 keV band) and found the ejecta consisting of the two components; the cold RP_L component with $kT_e \sim 0.9$ keV and the hot RP_H one with $kT_e \sim 1.5$ keV. Ozawa et al. (2009b), who analyzed the same Suzaku data, did not reach this conclusion since they performed a spectral analysis only in the limited energy band of 5–12 keV. With Chandra imaging analyses, the Fe band image is more compact than those of the Si, S, Ar and Ca bands (Lopez et al., 2013a). The fact that the Suzaku hard-band image is more compact than the soft band image (Figure 8.5) is consistent with the Chandra result. The RP_H component would be concentrated in the central region of the remnant compared to RP_L. If so, the plasma close to the rim would have lower kT_e than the plasma in the central region. This can be interpreted as the result of thermal conduction between the SNR shock and the surrounding dense molecular gas.

In the spectral analysis of the East and West regions, we found that kT_e of the western plasma is lower than the eastern plasma, which is consistent with the results of the spatially resolved spectral analysis with Chandra by Lopez et al. (2013b). Lopez et al. (2013b) claimed that the rarefaction scenario is likely to explain it. They claimed that the shock is interacting with a cloud only in the east, and that the ambient gas density outside the western shell should be lower. They then concluded that the dominant cooling process is adiabatic expansion since the lower density plasma has lower temperature. This interpretation, however, seems questionable to us. Since the 2.12 μm line was detected both on the eastern and western sides (Figures 8.1), the western shell should also be interacting with a cloud. Gamma-ray data provide another clue of the interaction. Abdo et al. (2010) and H. E. S. S. Collaboration et al. (2016) detected a GeV gamma-ray emission on the western side of the remnant. According to H. E. S. S. Collaboration et al. (2016), the gamma rays are most probably interpreted as π^0-decay emission. Therefore, the gamma-ray results indicate that dense gas is present also on the eastern side otherwise the bright gamma-ray emission would not be detected there.

Chapter 9

Discussion

9.1 Summary of the Results

We analyzed the Suzaku data of four Galactic SNRs: G166.0+4.3, IC 443, W44, and W49B. We obtained $N_{\rm H}$, kT_e, $kT_{\rm init}$ and n_et of each component of the thermal plasma in these remnants. Table 9.1 presents a summary of the parameters in the NE region of G166.0+4.3 and the SE region of IC 443 which correspond to the locations where the SNR shock is interacting with the molecular cloud, and the Whole regions of W44 and W49B. In the following, we determine electron densities, recombination timescales, and progenitor masses which are key parameters to discuss the physical origin of the RPs.

Table 9.1: Summary of the fitting results.

SNR	Region	ISM	Ejecta1			Ejecta2		
		kT_e (keV)	kT_e (keV)	$kT_{\rm init}$ (keV)	n_et (10^{11} s cm^{-3})	kT_e (keV)	$kT_{\rm init}$ (keV)	n_et (10^{11} s cm^{-3})
G166.0+4.3	NE	–	0.46 ± 0.03	3 (fixed)	$6.1^{+0.5}_{-0.4}$	$0.87^{+0.02}_{-0.03}$	–	–
IC 443	SE	0.22 ± 0.01	$0.54^{+0.03}_{-0.01}$	5 (fixed)	$4.2^{+0.2}_{-0.1}$	0.19 ± 0.01	5 (fixed)	$= n_et$ (Ejecta1)
W44	Whole	0.22 ± 0.01	0.37 ± 0.01	0.93 ± 0.02	$3.5^{+0.2}_{-0.3}$	–	–	–
W49B	Whole	$0.170^{+0.003}_{-0.004}$	0.94 ± 0.02	$5.9^{+1.4}_{-0.9}$	5.3 ± 0.2	$1.46^{+0.10}_{-0.08}$	$3.26^{+0.01}_{-0.10}$	< 0.9

Ejecta1 and Ejecta2 indicate RP$_{\rm (H-Ca)}$ and CIE$_{\rm (Fe\&Ni)}$ for G166.0+4.3, RP$_{\rm hot}$ and RP$_{\rm cold}$ for IC 443, and RP$_{\rm L}$ and RP$_{\rm H}$ for W49B, respectively. For W44, Ejecta1 indicates the RP component.

9.1.1 Electron densities and recombination timescales

We estimate electron densities (n_e) and recombination timescales ($t_{\rm rec}$) of the RP components in each remnant. In §5.4.2, we estimated n_e of the RP component in G166.0+4.3 from the volume emission measure. On the other hand, spectral fits directly give n_et of each remnant. By dividing the latter parameter by the former, we can obtain $t_{\rm rec}$, which we refer to as recombination timescale. In the same manner, we obtained n_e and $t_{\rm rec}$ of the plasmas in IC 443, W44, and W49B as listed in Table 9.2. In all the remnants, $t_{\rm rec}$ is shorter than $t_{\rm age}$, which is consistent with a picture that the plasmas become to be in a recombination-dominant state at some point of the SNR evolution most probably either by rarefaction or thermal conduction. We will discuss each possibility in §9.2 and §9.3.

Table 9.2: Summary of n_e and $t_{\rm rec}$.

SNR	Region	Ejecta1		Ejecta2		Distance	Radius	$t_{\rm age}$
		n_e ($\rm cm^{-3}$)	$t_{\rm rec}$ (kyr)	n_e ($\rm cm^{-3}$)	$t_{\rm rec}$ (kyr)	(kpc)	(pc)	(kyr)
G166.0+4.3	NE	$0.3f^{-1/2}$	$71f^{1/2}$	$0.3f^{-1/2}$	–	5†	20	$140f^{1/2}$
IC 443	SE	$0.9f^{-1/2}$	$15f^{1/2}$	$1.6f^{-1/2}$	$8.3f^{1/2}$	1.5†	10	30‡
W44	Whole	$0.7f^{-1/2}$	$16f^{1/2}$	–	–	3†	10	20‡
W49B	Whole	$2.7f^{-1/2}$	$6.0f^{1/2}$	$2.7f^{-1/2}$	$< 0.1f^{1/2}$	8†	5	6‡

A filling factor is denoted by f.
†Estimated distances to G166.0+4.3 (White & Long, 1991), IC 443 (Welsh & Sallmen, 2003), W44 (Claussen et al., 1997), and W49B (Moffett & Reynolds, 1994).
‡ Estimated ages of IC 443 (Olbert et al., 2001), W44 (Wolszczan et al., 1991), and W49B (Smith et al., 1985).

9.1.2 Abundance patterns and progenitor masses

X-ray spectral analyses of SNRs can be used to identify their SN types based on abundance patterns of their ejecta components. In our spectral analyses explained above, we obtained the abundances of each element in each remnant (G166.0+4.3: Table 5.3; IC 443: Tabale 6.2; W44: Table 7.3; W49B: Table 8.2). We here discuss SN types of G166.0+4.3, IC 443, W44, and W49B by comparing the obtained abundances with those of theoretical predictions for core-collapse (Woosley & Weaver, 1995) and Type Ia (Maeda et al., 2010) SNe.

Figure 9.1 shows abundance patterns normalized by Si in the NE and W regions of G166.0+4.3, the NE, NW, and SE regions of IC 443, and the Whole regions of W44 and W49B. From our results of IC 443, W44, and W49B, we interpreted the CIE components as the shocked ISM, whereas the RPs are attributed to the reverse-shock-heated ejecta. We therefore compare the abundance patterns of the RP components to those of the theoretical models. On the other hand, in the case of G166.0+4.3, we cannot distinguish the ISM component from the ejecta component, and, therefore, the obtained abundances may be a mixture of the ISM and ejecta. Even if this is the case, the contamination of the ISM decreases the ratios of O/Si, Ne/Si, Mg/Si, Fe/Si, and Ni/Si in the NE region but it does not affect the determination of the SN types.

G166.0+4.3 The abundance pattern of the NE region roughly agrees with that of a core-collapse SNe model with a progenitor mass of 20–30 $M_\odot$. On the other hand, the abundance pattern in the W region favors a core-collapse SN with 11 $M_\odot$. In either case, these results indicate a core-collapse origin rather than that of Type Ia.

IC 443 The abundances pattern of IC 443 in all the regions are similar to each other. They are consistent with those of core-collapse SNe with a progenitor mass of 20–30 $M_\odot$. The core-collapse origin is supported by the presence of the associated pulsar, CXOU J061705.3 +222127 (§A.1; Bocchino & Bykov, 2003; Swartz et al., 2015).

W44 The abundance pattern of W44 indicates a core-collapse SN origin since the Fe group elements (Fe and Ni) are less abundant than the intermediate mass elements (O, Ne, Mg, Si), which is typical for a nucleosynthesis model of core-collapse SNe. The estimated abundances with O/Si, Ne/Si, and Mg/Si $\sim$ 1, and Fe/Si and Ni/Si $<$ 1 exclude the models with $\leq$ 11 $M_\odot$ and $\geq$ 40 $M_\odot$. We therefore conclude that the progenitor mass is likely in the range of 20–30 $M_\odot$. The associated pulser PSR B1853+01 is detected in the

central region of W44 (Chapter 7; Petre et al., 2002), which is supportive evidence for our conclusion.

W49B The Mg/Si ratio of ~ 1 strongly favors the core-collapse origin. However, the Type Ia origin cannot be ruled out by the Fe/Si and Ni/Si ratios of ~ 1. The progenitor type of W49B is still under debate: Lopez et al. (2013a) found an asymmetric distribution of emissions from Fexxv lines with the Chandra imaging analysis. They claimed that the distribution suggests a Type Ib/c bipolar explosion. On the other hand, based on deep Chandra observations of W49B, Zhou & Vink (2017) claimed the abundance pattern is consistent with a Type Ia SN of a Chandrasekhar-mass white dwarf. They also reported candidate point sources inside W49B, which may conflict with a picture of the Type Ia SN if one of them is a neutron star.

We conclude that the origins of IC 443 and W44 are core-collapse SNe with progenitor masses of 20–30 $M_{\odot}$. G166.0+4.3 and W49B are also likely core-collapse SNe but their progenitor masses have large uncertainties.

9.1.3 Spatial variation of kT_e

In G166.0+4.3, we discovered an RP only in the outer part of the remnant in the dense NE region whereas the plasma in the lower-density W region is an IP. The temperature of the outer RP is lower than that of the inner Fe-rich plasma in the NE region and that of the IP in the W region. In IC 443, kT_e of both the RP components decrease toward the southeast where the remnant is interacting with the molecular cloud. In W44, kT_e of the RP in the center of the remnant is higher than that of the outer RP, suggesting that the SNR plasma is cooled sequentially from the rim to the center by the cool surrounding cloud. In W49B, the central plasma is hotter than the plasma in the rim, which is similarly seen in G166.0+4.3 and W44. In the spectral analysis of W49B, we also found that kT_e of the western plasma is lower than that of the eastern plasma. Since the gamma-ray emission is detected in the western side of the remnant, the western shell should be interacting with a cloud.

All the results above point to the same tendency that the electron temperature kT_e is lower at the locations with shell-cloud interactions. This is qualitatively consistent with the picture that the RPs are generated by rapid cooling of the plasmas through thermal conduction with the molecular clouds. More quantitatively, however, the cooling must proceed fast enough compared to the recombination of ions to realize RPs. We thus estimate the cooling timescale in the following section (§9.3).

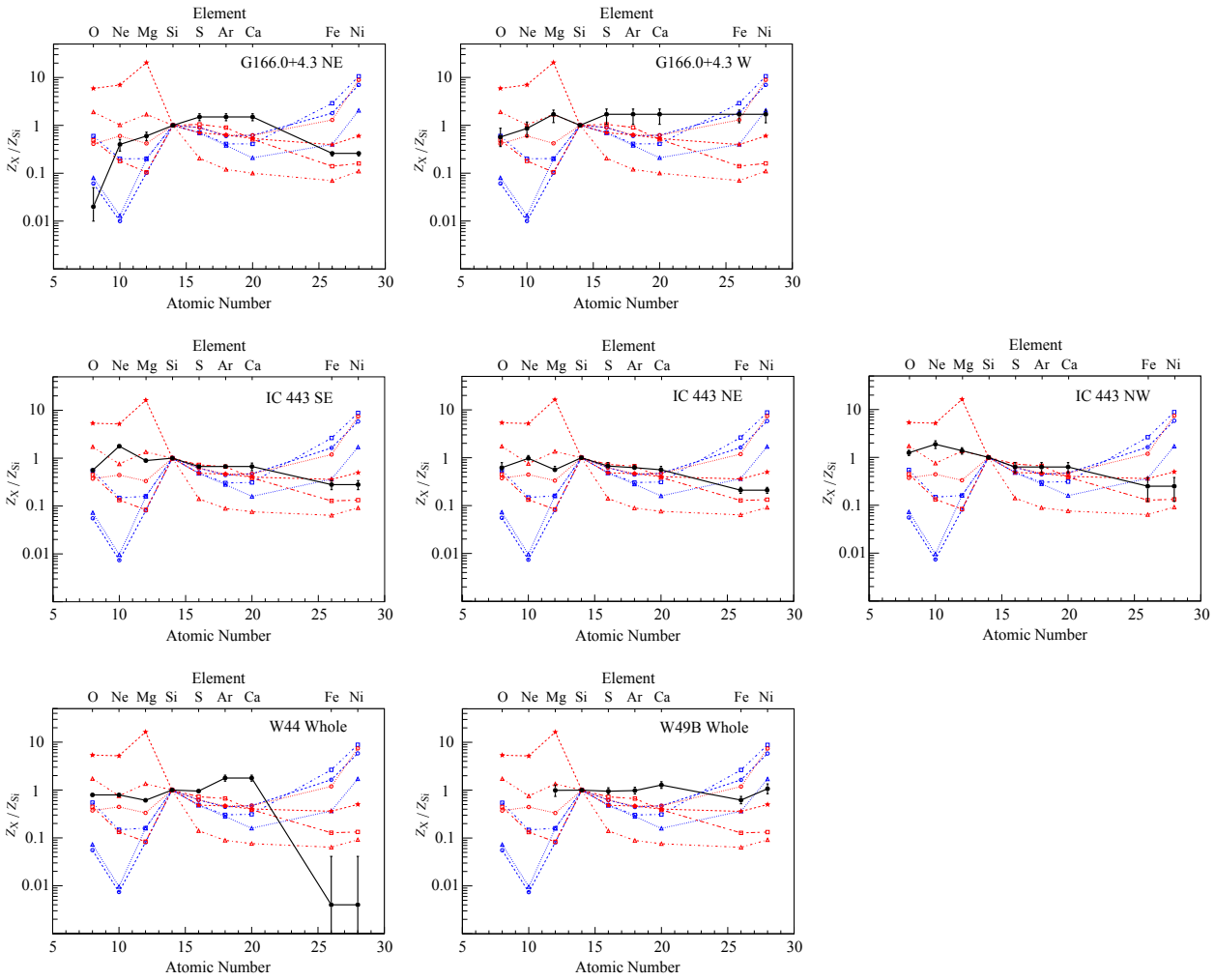

Figure 9.1: Abundance ratios of each element to Si in the NE and W regions of G166.0+4.3, the NE, NW, and SE regions of IC 443, and the Whole regions of W44 and W49B. The red points indicate several nucleosynthesis models for core-collapse SNe with different progenitor masses of 11 $M_\odot$ (red circle), 20 $M_\odot$ (red square), 30 $M_\odot$ (red traiangle), and 40 $M_\odot$ (red star) from Woosley & Weaver (1995). For Type Ia SNe, the blue points show W7 (blue circle) model from Nomoto et al. (1984), C-DEF (blue square), and C-DDT (blue triangle) models from Maeda et al. (2010).

9.1.4 Spatial variation of $n_e t$

The spectral analyses of IC 443, W44, and W49B revealed the spatial variation of $n_e t$ of the RPs, which can be translated into the spatial variation of the recombination timescales ($t_{\rm rec}$) once the electron density (n_e) is determined. For simplicity, we assume that n_e of the RP is uniform at the value listed in Table 9.2.

We note that, in G166.0+4.3, an RP is detected only in the NE region so that we cannot obtain the $n_e t$ distribution of this remnant. In the case of W44, $n_e t$ of the southern part of the remnant is higher than those of the other regions. It suggests that the shock-cloud interaction started in the early phase of the SNR evolution. We obtained similar results for W49B as well. We found that $n_e t$ of the inner plasma is lower than that of the outer part of the remnant (inner plasma: $n_e t < 0.9 \times 10^{11}$ s cm^{-3}; outer plasma: $n_e t = 4.4 \times 10^{11}$ s cm^{-3}), indicating that the inner plasma started to be cooled later than the outer plasma. These results on W44 and W49B are explained by the thermal conduction scenario, in which molecular clouds first cool the plasmas in the rim regions, and then the inner plasmas via the outer plasmas.

In the case of IC 443, interestingly, a different tendency was observed. The RP in the southeast, where the shock-cloud interaction occurs, has a lower ionization timescale $n_e t = 4.2 \times 10^{11}$ s cm^{-3} than those of the northwestern parts of the remnant $n_e t \sim 10^{12}$ s cm^{-3}. Nevertheless, several possibilities can be considered in the thermal conduction scenario. One possibility would be that the dense molecular in the southeastern region recently collided with the shell and cooled the plasma rapidly, and that the plasma in the northwestern region has been cooled by other lower density gas for a longer time since an earlier phase. The other possibility is that IC 443 has the same $n_e t$ variation only in the line-of-sight direction, which cannot be measured in our spectral analysis.

9.2 Rarefaction

As discussed in §9.3, the rarefaction scenario is unlikely to explain the kT_e spatial variation we observed. Nevertheless, we discuss the formation process of RPs in the context of the rarefaction scenario by using the progenitor masses given in §9.1.2. Itoh & Masai (1989) proposed the rarefaction scenario, in which RPs are realized by adiabatic cooling when the SNR shock breaks out of a dense CSM into a lower density ISM. Shimizu et al. (2012) carried out 3D-hydrodynamical calculations of the interaction between the expanding supernova ejecta and the CSM. They concluded that the CSM radius needs to be a sub-pc scale ($\lesssim 1$ pc) in order for the adiabatic expansion significantly cools the plasma. Chen et al. (2013) found a linear relationship between the radius of a massive star's main-sequence bubble ($R_{\rm b}$) in a molecular environment and the star's initial mass: $R_{\rm b} \approx 1.22 M/M_{\odot} - 9.16$ pc (Figure 9.2). In this case, the upper limit to the progenitor mass is $\sim 8.3\ M_{\odot}$ to realize the rarefaction if we accept the requirement of the CSM size < 1 pc given by Shimizu et al. (2012) as mentioned above. As described in §9.1.2, the estimated progenitor masses of IC 443 and W44 are 20–30 $M_{\odot}$, which are much larger than the upper limit; we therefore rule out the possibility of the rarefaction scenario. On the other hand, since we cannot determine the progenitor masses of G166.0+4.3 and W49B, the rarefaction scenario is still possible for these remnants in terms of the CSM size.

Our result is consistent with the conclusion by Moriya (2012). They studied the CSM around several supernova progenitors and discussed which progenitors can have a CSM dense enough to establish CIE soon after the explosion. They suggested that the CSM around supergiants can establish CIE and can evolve to become recombining SNRs, but massive progenitors of Wolf-Rayet stars are unlikely.

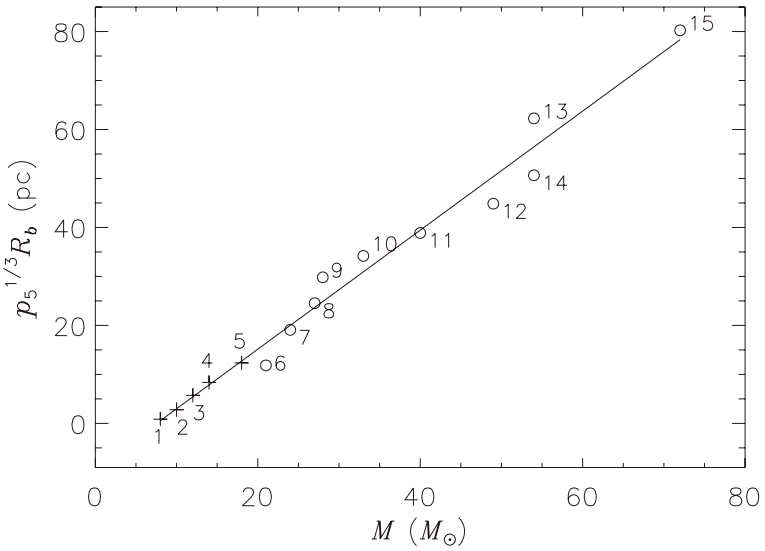

Figure 9.2: Relationship between radii of the wind-blown bubbles and the stellar masses for OB stars (Chen et al., 2013). The plus and circle signs indicate the B and O stars, respectively. The solid line represents a linear regression, $p_5^{1/3} R_{\rm b} = 1.22 M/M_{\odot} - 9.16$ pc, where $R_{\rm b}$ and p_5 are the maximum size of the bubbles and normalized pressure $p_5 \equiv (p/k)(10^5\ {\rm cm}^{-3}\ {\rm K})$, respectively.

9.3 Thermal Conduction

If the scale length of the temperature gradient $l_{\rm T} \equiv T_e/|\nabla T_e|$ is much longer than the mean free path of electrons $\lambda_e \approx 10^{18}(T_e/10^7\ {\rm K})^2(n_e/1\ {\rm cm}^{-3})^{-1}$ cm, the heat flux is calculated by the classical formula,

$$Q_{\rm class} = -\kappa \nabla T_e. \tag{9.1}$$

Spitzer (1956) gave the thermal conductivity as

$$\kappa = 1.31 n_e \lambda_e k \left(\frac{kT_e}{m_e}\right)^{1/2} \approx 4.6 \times 10^{13} \left(\frac{T_e}{10^8\ {\rm K}}\right)^{5/2} \left(\frac{\ln\Lambda}{40}\right)^{-1}\ {\rm ergs}^{-1}{\rm cm}^{-1}{\rm K}^{-1}, \tag{9.2}$$

where the plasma parameter is described as

$$\Lambda = \frac{4}{3}\pi \left(\frac{\epsilon_0 k T_e}{n_e e^2}\right)^{3/2} n_e. \tag{9.3}$$

If $l_{\rm T}$ is comparable to or less than λ_e, the electrons diffuse at a speed greater than their average thermal speed, and the conduction is in a "saturation" regime. The heat flux approaches a limited value given by Cowie & McKee (1977),

$$Q_{\rm sat} = 0.4 n_e k T_e \left(\frac{2kT_e}{\pi m_e}\right)^{1/2}. \tag{9.4}$$

We divide the SNR plasma into 10 layers with the same thickness (d), and calculate heat flows between each layer at each time step (see a schematic picture shown in Figure 9.3). The heat flow into and out of the i-th layer ($\Delta E_{\rm cond}$) can be calculated as

$$\Delta E_{\rm cond} \simeq (Q_{i,i-1}S_{i,i-1} - Q_{i+1,i}S_{i+1,i})\Delta t \tag{9.5}$$

$$k\Delta T_e = \frac{2\Delta E_{\rm cond}}{3 n_e V_i}, \tag{9.6}$$

where $Q_{i,j}$, $S_{i,j}$, and V_i are the heat flux and the contact area between the layers i and j, and the volume of the layer i, respectively. We adopt the heat flux of

$$Q_{i,j} = \begin{cases} Q_{\rm class} & (l_{\rm T}/\lambda_e > 10) \\ (Q_{\rm class}^{-1} + Q_{\rm sat}^{-1})^{-1} & (1 \le l_{\rm T}/\lambda_e \le 10) \\ Q_{\rm sat} & (l_{\rm T}/\lambda_e < 1). \end{cases} \tag{9.7}$$

In the intermediate regime of $1 \le l_{\rm T}/\lambda_e \le 10$, we smoothly connect them between the classical and saturated conduction regime by following Dalton & Balbus (1993).

Table 9.3 and Figure 9.4 show the initial parameters and the results in each remnant. We assumed $kT_{\rm init}$ of the RP component determined by the spectral fitting as the initial temperature of the plasma. We assumed that the temperature of the outer cool gas is constant at zero. The thickness of the layers are one tenth of the SNR radius. As the initial electron density, we adopted n_e obtained by the spectral analyses when the filling factors were assumed to be 1 (see Table 9.2). We also assumed that heat flows only between adjacent layers. For simplicity, we assumed that a volume of the plasma and

n_e are constant at their initial values. This assumption is justified as explained below. According to McKee & Cowie (1975), a ratio of the expansion velocity propagating into the molecular cloud to that before the shock-cloud interaction is described as,

$$\frac{v_{\rm MC}}{v_{\rm ISM}} = k \left(\frac{n_{\rm MC}}{n_{\rm ISM}} \right)^{-1/2}, \tag{9.8}$$

where k is a factor which depends weakly on the density ratio of ISM to a molecular cloud ($n_{\rm MC}/n_{\rm ISM}$), ranging k = 1–1.5. If we adopt the densities of ISM and a molecular cloud as ~ 1 cm^{-3} and 10^2–10^3 cm^{-3}, respectively, $v_{\rm MC}/v_{\rm ISM}$ would be $\lesssim 0.15$.

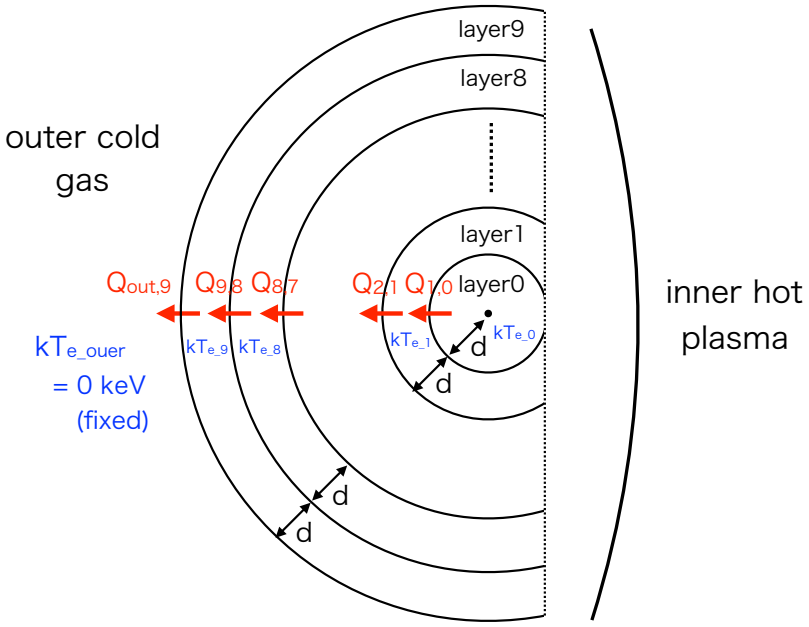

Figure 9.3: Schema of the plasma structure in our calculation of the time development of kT_e with the thermal conduction between the inner hot plasma and the outer cold gas.

Table 9.3: Initial parameters for the calculation of the time evolution of kT_e.

SNR	$kT_{\rm outer}$ (keV)	$kT_{\rm inner}$ (keV)	d (pc)	n_e (cm^{-3})
G166.0+4.3	0	3.0	2	0.3
IC 443	0	5.0	1	0.9
W44	0	0.93	1	0.7
W49B	0	5.9	0.5	2.7

From Figure 9.4, we confirm that the cooling timescale of kT_e of the inner plasma is much longer than that of the outer plasma. The results reproduce the observed distributions of kT_e in G166.0+4.3 and W49B. Here we define a conduction timescale $t_{\rm cond}$ as a time when the calculations reach the observed temperatures kT_e of the RP components in the innermost layer (see Table 9.4). From Figure 9.4, we estimated $t_{\rm cond}$ of G166.0+4.3, IC 443, W44 and W49B at $\sim$ 40 kyr, $\sim$ 20 kyr, $\sim$ 35 kyr and $\sim$ 4 kyr, respectively.

Kawasaki et al. (2002) estimated a conduction timescale of the plasma in IC 443 with a different assumption from us. They found that the plasma is composed of the outer cold CIE with $kT_e \sim 0.2$ keV and the inner hot RP with $kT_e \sim 1.0$ keV with ASCA, and calculated the timescale to equilibrate the temperatures of the two components. They compared the conduction timescale of ~ 6 kyr with $t_{\rm CIE} \sim 63\ (n_e/1\ {\rm cm}^{-3})^{-1}$ kyr which is a characteristic timescale for a plasma to reach CIE (Masai, 1994). They concluded that the thermal conduction can realize RPs because the conduction timescale is shorter than $t_{\rm CIE}$.

To investigate whether the RPs can be realized with the conduction timescales estimated by us under the different assumption from Kawasaki et al. (2002), we compare $t_{\rm cond}$ with $t_{\rm CIE}$. Table 9.4 lists $t_{\rm cond}$ and $t_{\rm CIE}$ of each remnant. We confirmed that the conduction timescales are shorter than $t_{\rm CIE}$ for all the remnants, indicating that the plasmas can become RPs with the thermal conduction between the plasma and the molecular cloud. The result contradicts with conclusions by other authors that the thermal conduction timescale is too long to realize RPs in some SNRs. Uchida et al. (2012) analyzed the Suzaku data of W44 and interpreted that the temperatures of the inner and outer plasmas are 0.48 keV and 0.40 keV, respectively. They estimated the conduction timescale of $\sim$ 10000 kyr with the same method as presented by Kawasaki et al. (2002). They claimed that the thermal conduction scenario is unlikely because of the longer conduction timescale than $t_{\rm CIE}$. We reached a different conclusion from theirs because of the different definitions of the timescale as mentioned above.

If the thermal conduction is a cause of the RPs, it is also required that $t_{\rm cond}$ should be shorter than the SNR age, $t_{\rm age}$. Table 9.4 lists $t_{\rm cond}$ and $t_{\rm age}$ of each remnant. For G166.0+4.3, we estimated the age at $\sim 130\ (n_e/0.3\ {\rm cm}^{-3})^{-1}$ kyr (§5.4.2). We adopted 30 kyr, 20 kyr and 6 kyr given by Olbert et al. (2001), Wolszczan et al. (1991), and Smith et al. (1985) as the ages of IC 443, W44 and W49B, respectively. The requirement of $t_{\rm cond} \leq t_{\rm age}$ is satisfied for G166.0+4.3, IC 443, and W49B, whereas $t_{\rm cond}$ of W44 is longer than its age. The calculations of $t_{\rm cond}$, however, highly depend on n_e which has large uncertainties with the assumed volumes of the plasma and the distance to the remnant.

We then calculated $t_{\rm cond}$ as a function of electron density n_e as plotted in Figure 9.5. Under the condition of $t_{\rm cond} < t_{\rm age}$, the electron densities are limited to $n_e \lesssim 0.55\ {\rm cm}^{-3}$ for G166.0+4.3, $n_e \lesssim 1.4\ {\rm cm}^{-3}$ for IC 443, $n_e \lesssim 0.40\ {\rm cm}^{-3}$ for W44, and $n_e \lesssim 4.5\ {\rm cm}^{-3}$ for W49B. If the electron densities of the SNR plasmas satisfy these requirements, the RPs can be explained by the thermal conduction scenario.

Table 9.4: List of timescales in each remnants.

SNR	n_e ($\rm cm^{-3}$)	kT_e (keV)	$t_{\rm cond}$ (kyr)	$t_{\rm CIE}$ (kyr)	$t_{\rm age}$ (kyr)
G166.0+4.3	0.3	0.46	40	200	130
IC 443	0.9	0.54	20	70	30
W44	0.7	0.37	35	90	20
W49B	2.7	0.94	4	20	6

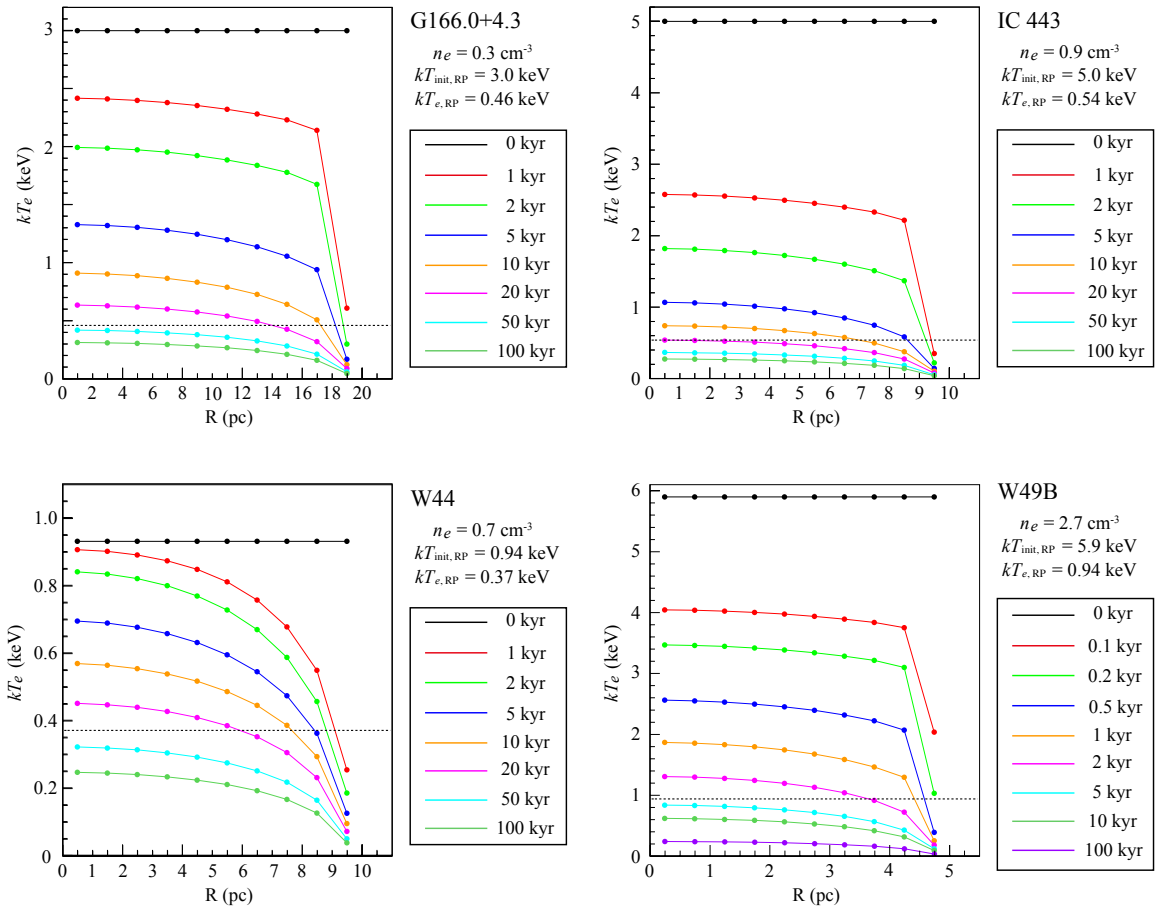

Figure 9.4: Time evolution of the electron temperatures of the RPs in G166.0+4.3 (top left), IC 443 (top right), W44 (bottom left), and W49B (bottom right) as a function of distances from the center of the remnant. The dotted lines indicate kT_e of the RPs obtained by the spectral analyses.

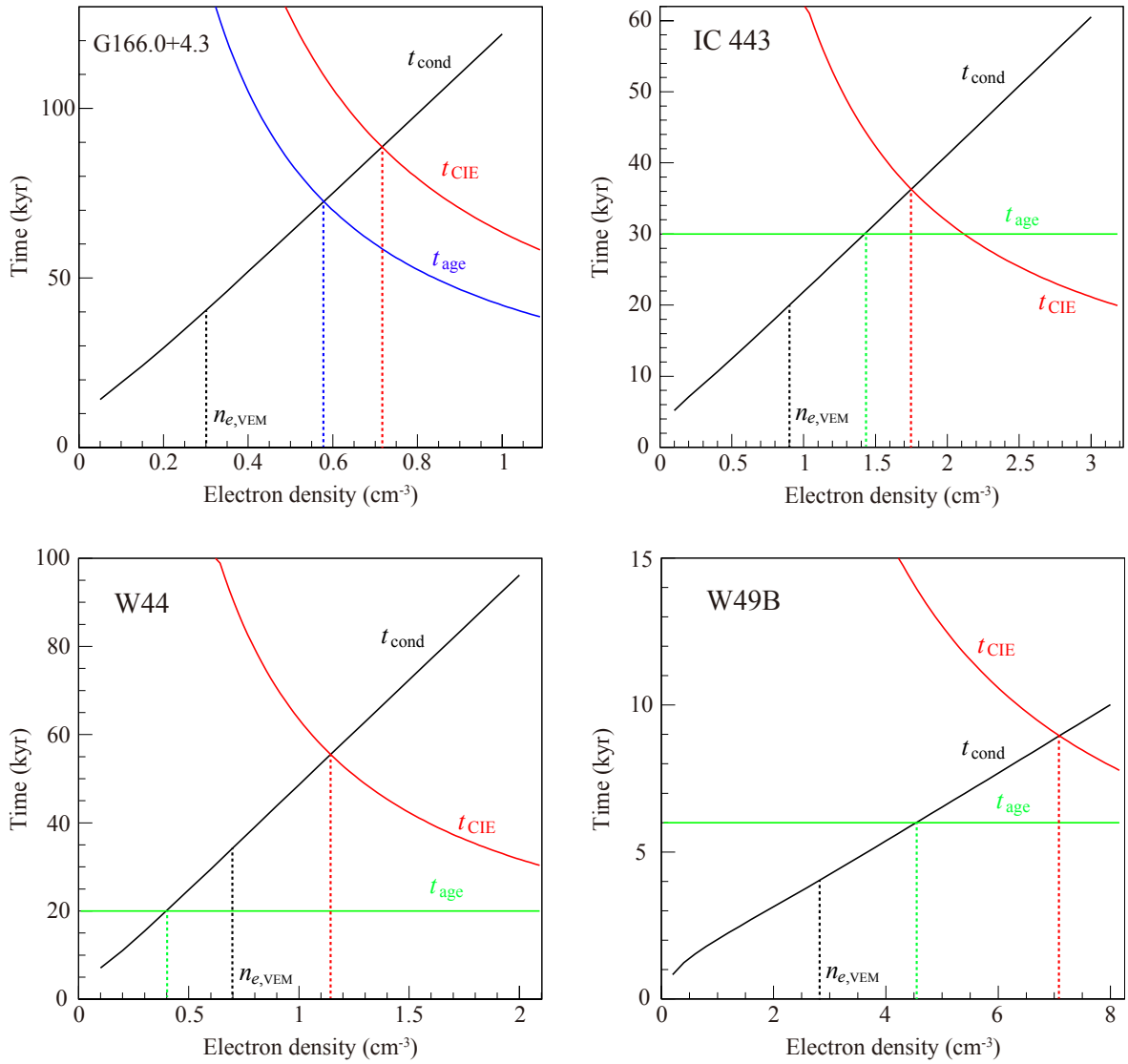

Figure 9.5: Conduction timescales of G166.0+4.3 (top left), IC 443 (top right), W44 (bottom left), and W49B (bottom right) as a function of the electron densities denoted by the black solid lines. The red solid lines indicate the characteristic timescale of 63 $(n_e/1\ \mathrm{cm}^{-3})^{-1}$ kyr for a plasma to reach CIE (Masai, 1994). The blue and green solid lines show the age of G166.0+4.3, IC 443, W44, and W49B estimated by us (§5.4.2), Olbert et al. (2001), Wolszczan et al. (1991), and Smith et al. (1985), respectively. The electron density obtained from a volume emission measure ($n_{e,\mathrm{VEM}}$) is denoted by the black dotted lines.

Chapter 10

Conclusions

We studied the RPs in the four Galactic SNRs, G166.0+4.3, IC 443, W44, and W49B with Suzaku. The results are summarized as follows:

1. The spectrum of the W region in G166.0+4.3 is well fitted with a one-component IP model, whereas the plasma in the dense NE region consists of the Fe-rich plasma and RP components. The Fe-rich plasma is concentrated near the center of the remnant whereas the other elements are distributed in the outer region. The electron temperature of the RP is lower than those of the inner Fe-rich plasma and the IP in the W region. The results of the spectral analysis are simply explained by the thermal conduction with the cool dense gas in the northeastern part of the remnant.

2. We performed spatially resolved spectroscopy of X-ray emissions from IC 443. The spectra extracted from each region of the remnant are all fitted well with a model consisting of CIE and two RP components. The electron temperature of one of the RP component ranges from 0.16 keV to 0.28 keV whereas that of the other RP component is in the range of 0.48–0.67 keV. The electron temperatures of both RP components decrease toward the southeast, where the remnant is interacting with the molecular cloud. Also, the normalization ratio of the lower-kT_e RP to higher-kT_e RP components increases toward the southeast. The two findings may be a result of cooling of the X-ray emitting plasma by the interacting molecular cloud via thermal conduction.

3. The spectra extracted from 13 regions in W44 are well reproduced by a model consisting of CIE and RP components. We found that the electron temperatures of the RPs in the central part of the remnant are higher than those in the other regions. The intensity ratios of the ^{12}CO($J = 2$–1) to ^{12}CO($J = 1$–0) emissions are higher in the outer regions, suggesting the interaction between the SNR shock and the molecular cloud there. The lower kT_e in the outer regions can be explained by the thermal conduction between the plasma and the interacting molecular cloud.

4. In W49B, we found that the spectra are well fitted with a model consisting of CIE and two RPs ($\mathrm{RP_L}$ for the lighter elements and $\mathrm{RP_H}$ for the heavier elements). $\mathrm{RP_H}$, which is in the central region as indicated by our imaging analysis, is hotter than the $\mathrm{RP_L}$ in the rim, which is similarly seen in G166.0+4.3 and W44. We also found that kT_e of the western plasma is lower than that of the eastern plasma. The western

shell should be interacting with a cloud from the gamma-ray emission, suggesting cooling by the thermal conduction there.

In all the remnants, the spectral analyses revealed good correlations between the electron temperatures and locations of the surrounding molecular clouds. For a more quantitatively investigation, we estimated the cooling timescale by the thermal conductions in each remnant. The conduction timescales $t_{\rm cond}$ of G166.0+4.3, IC 443, W44 and W49B are estimated at $\sim$ 40 kyr, $\sim$ 20 kyr, $\sim$ 35 kyr and $\sim$ 4 kyr, respectively. These are shorter than a characteristic timescale for a plasma to reach CIE, indicating that that the plasmas can become RPs with the thermal conduction between the shock and the molecular cloud. On the other hand, the requirement of $t_{\rm cond} \leq t_{\rm age}$ is also satisfied for all the remnants but W44. The calculations of $t_{\rm cond}$, however, highly depend on an electron density n_e which has large uncertainties depending on the assumptions about the volumes of the plasma and the distance to the remnant. We, therefore, calculated $t_{\rm cond}$ as a function of electron density n_e. We found that the electron densities are limited to $n_e \lesssim 0.55$ cm^{-3} for G166.0+4.3, $n_e \lesssim 1.4$ cm^{-3} for IC 443, $n_e \lesssim 0.40$ cm^{-3} for W44, and $n_e \lesssim 4.5$ cm^{-3} for W49B. If the electron densities of the SNR plasmas satisfy these requirements, the RPs can be explained by the thermal conduction scenario.

Appendix A

Spatially resolved spectroscopy of IC 443

A.1 Fitting results of the spectra in the regions A and B

Figure A.1 shows spectra of the PWN 1SAX J0617.1+2221 in region A and the point source U061530.75+224910.6 in region B in the 1.6-10.0 keV band after NXB subtraction. We fitted the spectra with a model consisting of a power law and an RP component for the sources and the SNR plasma, respectively. The X-ray absorption was fixed at 7.0×10^{21} cm^{-2} as determined by Kawasaki et al. (2002). We fixed $kT_{\rm init}$ at 5 keV, whereas kT_e and $n_e t$ were allowed to vary. The abundances of Si and S were allowed to vary, whereas those of Ar and Ca were linked to S. The abundances of the other elements were fixed to solar. The spectra can be reproduced well by the model (Table A.1). The photon indices of PWN 1SAX J0617.1+2221 and U061530.75+224910.6 are $1.89^{+0.08}_{-0.07}$ and $2.22^{+0.15}_{-0.16}$, respectively, which we used in the SNR emission analysis (see §6.3.2). The photon indices and the fluxes of the power-law components are consistent with the results by Bocchino & Bykov (2003), who analyzed XMM-Newton data.

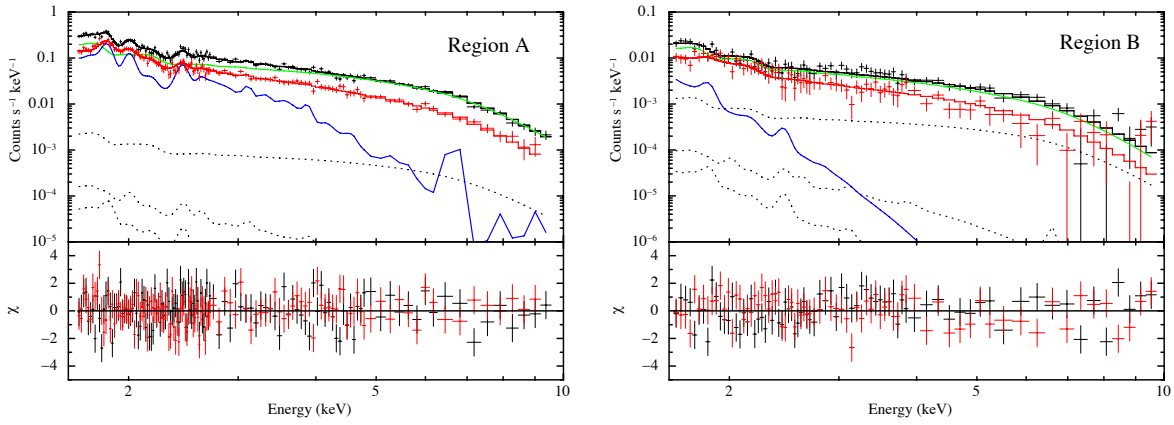

Figure A.1: Same as Figure 6.4 but for regions A and B.

Table A.1: Best-fit model parameters of the spectra in regions A and B.

Model function	Parameter	1SAX J0617.1+2221 region A	U061530.75+224910.6 region B
TBabs	$N_{\rm H}$ (10^{22} cm^{-2})	0.7 (fixed)	0.7 (fixed)
Power law	Photon index	$1.89\ ^{+0.08}_{-0.07}$	$2.22\ ^{+0.15}_{-0.16}$
	Normalization*	$801\ ^{+114}_{-94}$	$254\ ^{+30}_{-50}$
VVRNEI	kT_e (keV)	$0.34\ ^{+0.05}_{-0.04}$	$0.31\ ^{+0.49}_{-0.20}$
(RP comp.)	kT_{init} (keV)	5 (fixed)	5 (fixed)
	$Z_{\rm Si}$ (solar)	$2.4\ ^{+0.7}_{-0.5}$	1 (fixed)
	$Z_{\rm S} = Z_{\rm Ar} = Z_{\rm Ca}$ (solar)	$1.3\ ^{+0.4}_{-0.3}$	1 (fixed)
	$n_e t$ (10^{11} s cm^{-3})	$4.2\ ^{+0.6}_{-0.4}$	> 100
	VEM (10^{57} cm^{-3})†	$1.2\ ^{+0.2}_{-0.4}$	$1.0\ ^{+5.7}_{-1.0}$
	χ^2_ν (ν)	1.16 (241)	1.05 (149)

† Volume emission measure at the distance of 1.5 kpc: $VEM = \int n_e n_{\rm H} dV$, where n_e, $n_{\rm H}$, and V are the electron and hydrogen densities, and the emitting volume, respectively.
* The unit is photons s^{-1} cm^{-2} keV^{-1} sr^{-1} at 1 keV.

A.2 Fitting results of the spectra in the regions 1–20

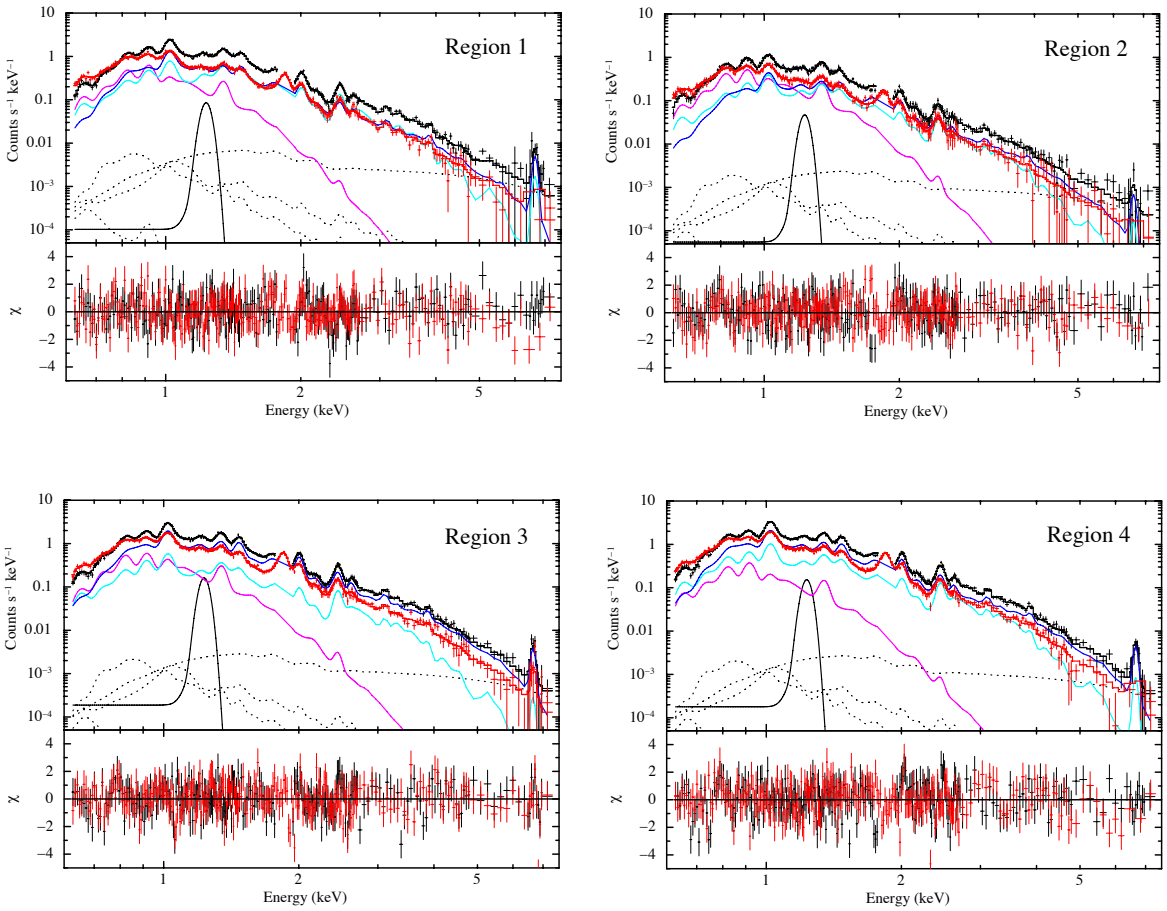

Figure A.2: Same as Figure 6.4 but for regions 1–4.

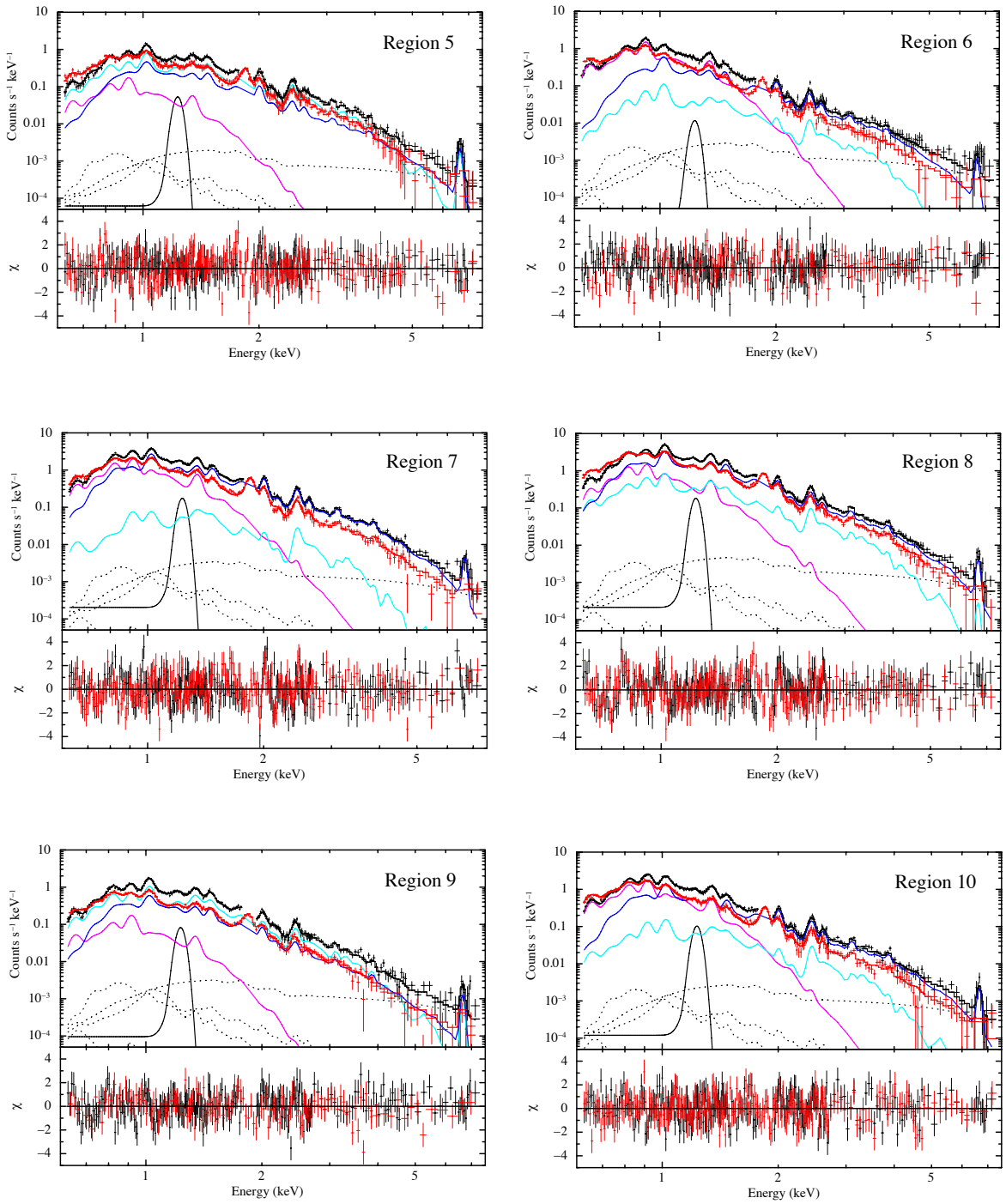

Figure A.3: Same as Figure 6.4 but for regions 5–10.

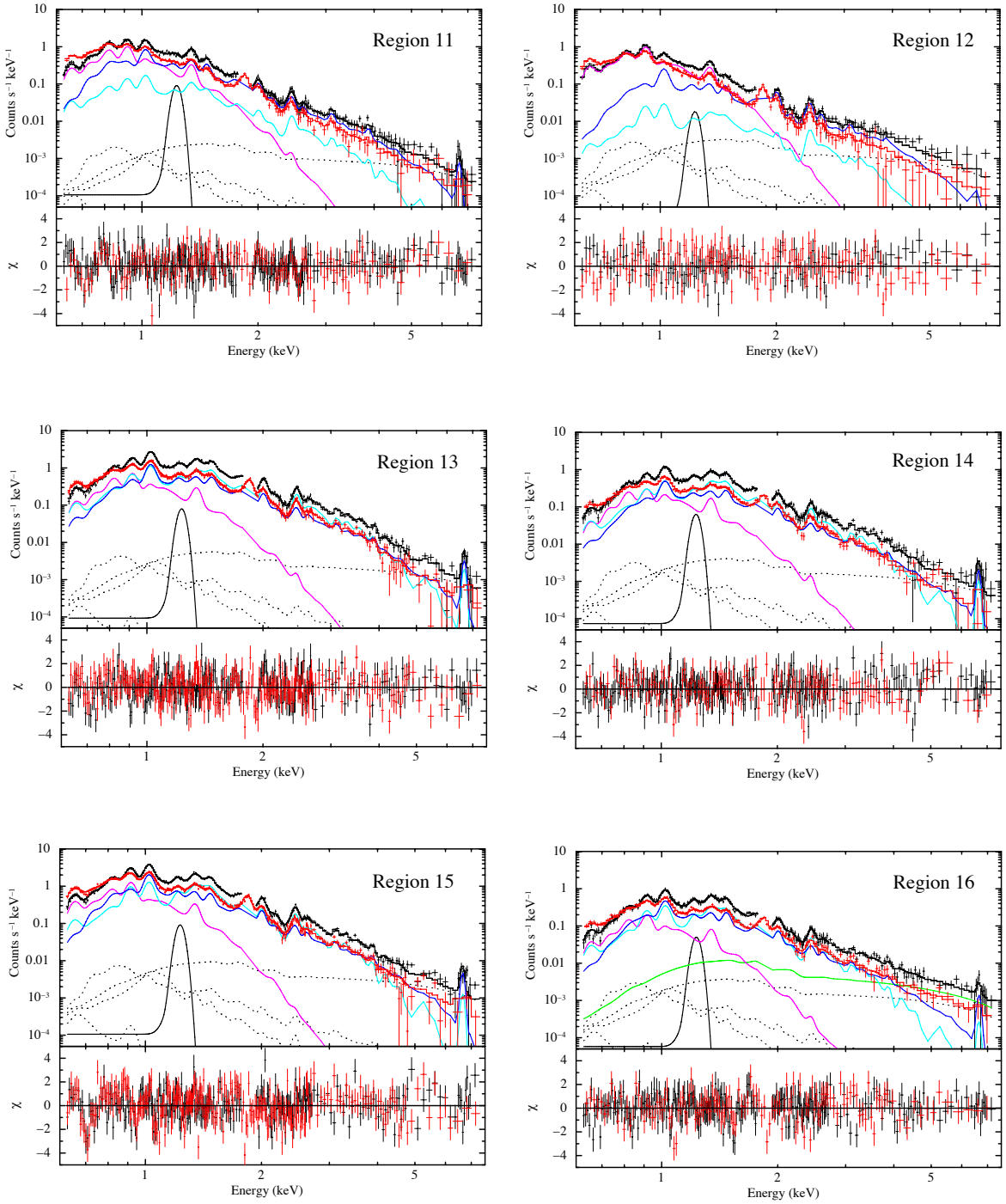

Figure A.4: Same as Figure 6.4 but for regions 11–16.

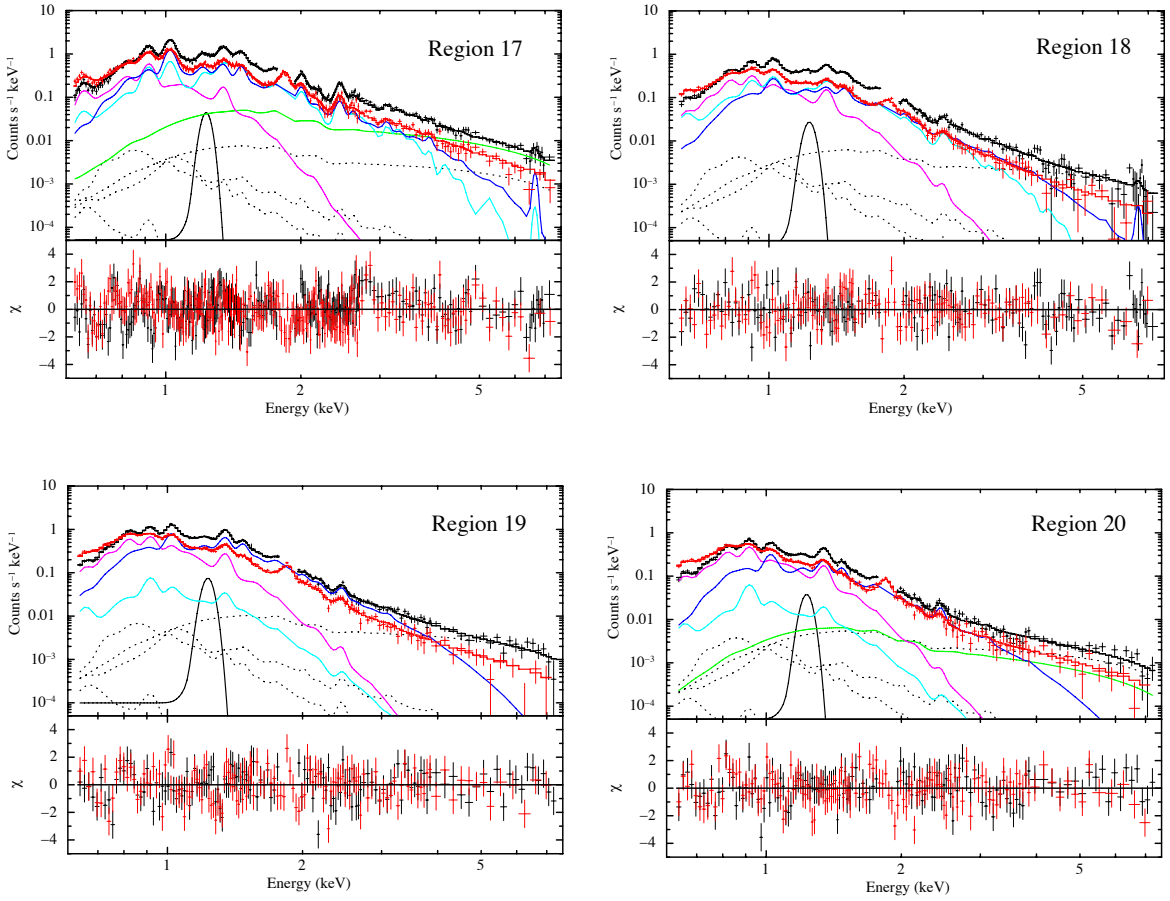

Figure A.5: Same as Figure 6.4 but for regions 17–20.

Table A.2: Best-fit model parameters of the spectra from regions 1–10.

Model function	Parameter	reg.1	reg.2	reg.3	reg.4	reg.5	reg.6	reg.7	reg.8	reg.9	reg.10
TBabs	$N_{\rm H}$ (10^{22} cm^{-2})	$0.94^{+0.04}_{-0.04}$	$0.95^{+0.04}_{-0.04}$	$0.82^{+0.03}_{-0.04}$	$0.79^{+0.03}_{-0.03}$	$0.88^{+0.05}_{-0.06}$	$0.89^{+0.02}_{-0.02}$	$0.79^{+0.02}_{-0.02}$	$0.70^{+0.03}_{-0.02}$	$0.84^{+0.04}_{-0.05}$	$0.74^{+0.02}_{-0.03}$
VVRNEI1	kT_e (keV)	$0.24^{+0.02}_{-0.01}$	$0.26^{+0.01}_{-0.02}$	$0.28^{+0.05}_{-0.01}$	$0.25^{+0.04}_{-0.01}$	$0.22^{+0.05}_{-0.03}$	$0.21^{+0.01}_{-0.01}$	$0.24^{+0.01}_{-0.01}$	$0.26^{+0.01}_{-0.01}$	$0.20^{+0.06}_{-0.06}$	$0.23^{+0.01}_{-0.01}$
(CIE comp.)	$Z_{\rm all}$ (solar)	1 (fixed)	1 (fixed)	1 (fixed)	1 (fixed)	1 (fixed)	1 (fixed)	1 (fixed)	1 (fixed)	1 (fixed)	1 (fixed)
	VEM (10^{57} cm^{-3})†	$2.9^{+1.3}_{-0.9}$	$1.7^{+0.6}_{-0.5}$	$1.1^{+0.5}_{-0.4}$	$0.8^{+0.4}_{-0.4}$	$0.8^{+0.7}_{-0.3}$	$7.5^{+1.1}_{-0.9}$	$4.3^{+1.7}_{-0.4}$	$2.7^{+0.6}_{-0.5}$	$1.1^{+1.1}_{-1.0}$	$4.5^{+1.0}_{-0.7}$
VVRNEI2	kT_e (keV)	$0.22^{+0.01}_{-0.01}$	$0.28^{+0.05}_{-0.07}$	$0.25^{+0.05}_{-0.05}$	$0.27^{+0.02}_{-0.02}$	$0.25^{+0.02}_{-0.01}$	$0.27^{+0.07}_{-0.09}$	$0.16^{+0.08}_{-0.07}$	$0.26^{+0.01}_{-0.01}$	$0.25^{+0.04}_{-0.05}$	$0.22^{+0.07}_{-0.03}$
($\rm RP_{cold}$ comp.)	$kT_{\rm init}$ (keV)	5 (fixed)	5 (fixed)	5 (fixed)	5 (fixed)	5 (fixed)	5 (fixed)	5 (fixed)	5 (fixed)	5 (fixed)	5 (fixed)
	$Z_{\rm Ne}$ (solar)	$2.5^{+0.4}_{-0.3}$	$1.9^{+0.3}_{-0.4}$	$2.2^{+0.2}_{-0.3}$	$1.9^{+0.2}_{-0.1}$	$2.3^{+0.3}_{-0.3}$	$5.1^{+1.7}_{-1.5}$	$2.2^{+0.3}_{-0.2}$	$1.8^{+0.1}_{-0.1}$	$2.0^{+0.2}_{-0.3}$	$3.4^{+0.5}_{-0.5}$
	$Z_{\rm Mg}$ (solar)	$1.5^{+0.1}_{-0.2}$	$1.2^{+0.2}_{-0.2}$	$1.5^{+0.1}_{-0.2}$	$1.4^{+0.1}_{-0.1}$	$1.3^{+0.3}_{-0.1}$	$2.2^{+0.8}_{-0.6}$	$1.3^{+0.2}_{-0.1}$	$1.4^{+0.1}_{-0.1}$	$1.4^{+0.2}_{-0.1}$	$1.7^{+0.3}_{-0.3}$
	$Z_{\rm Si}$ (solar)	$2.0^{+0.2}_{-0.2}$	$1.7^{+0.2}_{-0.3}$	$2.7^{+0.2}_{-0.2}$	$2.5^{+0.2}_{-0.1}$	$2.4^{+0.2}_{-0.2}$	$4.9^{+1.6}_{-1.1}$	$3.4^{+0.1}_{-0.3}$	$2.2^{+0.1}_{-0.2}$	$1.5^{+0.2}_{-0.1}$	$4.2^{+0.6}_{-0.5}$
	$Z_{\rm S}$ (solar)	$1.2^{+0.1}_{-0.2}$	$1.0^{+0.2}_{-0.2}$	$1.7^{+0.2}_{-0.1}$	$1.6^{+0.1}_{-0.2}$	$1.4^{+0.2}_{-0.1}$	$3.6^{+0.9}_{-0.9}$	$2.4^{+0.3}_{-0.2}$	$1.6^{+0.1}_{-0.2}$	$0.9^{+0.1}_{-0.1}$	$3.3^{+0.4}_{-0.4}$
	$Z_{\rm Ar} = Z_{\rm Ca}$ (solar)	$1.3^{+0.3}_{-0.2}$	$0.9^{+0.5}_{-0.4}$	$1.6^{+0.3}_{-0.2}$	$1.4^{+0.2}_{-0.3}$	$1.3^{+0.3}_{-0.3}$	$2.4^{+1.2}_{-1.2}$	$2.5^{+0.4}_{-0.4}$	$1.9^{+0.3}_{-0.2}$	$1.0^{+0.3}_{-0.2}$	$3.1^{+0.8}_{-0.6}$
	$Z_{\rm Fe} = Z_{\rm Ni}$ (solar)	$0.7^{+0.1}_{-0.1}$	$0.4^{+0.1}_{-0.1}$	$0.5^{+0.1}_{-0.1}$	$0.5^{+0.1}_{-0.1}$	$0.8^{+0.1}_{-0.2}$	$1.1^{+0.5}_{-0.3}$	$0.6^{+0.1}_{-0.1}$	$0.5^{+0.1}_{-0.1}$	$0.8^{+0.2}_{-0.1}$	$0.8^{+0.2}_{-0.1}$
	$n_e t$ (10^{11} s cm^{-3})	$4.1^{+0.3}_{-0.2}$	$5.6^{+0.6}_{-0.6}$	$5.4^{+0.4}_{-0.2}$	$5.1^{+0.2}_{-0.2}$	$4.4^{+0.2}_{-0.3}$	$5.6^{+0.5}_{-0.4}$	$5.4^{+0.1}_{-0.3}$	$5.7^{+0.2}_{-0.2}$	$5.4^{+0.4}_{-0.3}$	$5.6^{+0.2}_{-0.3}$
	VEM (10^{57} cm^{-3})†	$3.3^{+0.5}_{-0.5}$	$1.1^{+0.7}_{-0.5}$	$1.2^{+0.4}_{-0.3}$	$1.8^{+0.3}_{-0.4}$	$2.1^{+0.3}_{-0.3}$	$0.1^{+0.1}_{-0.1}$	$0.3^{+0.2}_{-0.2}$	$1.8^{+0.6}_{-0.5}$	$3.2^{+0.5}_{-0.5}$	$0.3^{+0.1}_{-0.1}$
VVRNEI3	kT_e (keV)	$0.56^{+0.04}_{-0.05}$	$0.62^{+0.07}_{-0.07}$	$0.62^{+0.02}_{-0.03}$	$0.59^{+0.03}_{-0.02}$	$0.67^{+0.06}_{-0.05}$	$0.64^{+0.06}_{-0.04}$	$0.55^{+0.03}_{-0.02}$	$0.57^{+0.02}_{-0.01}$	$0.61^{+0.04}_{-0.06}$	$0.61^{+0.03}_{-0.03}$
($\rm RP_{hot}$ comp.)	$kT_{\rm init}$ (keV)	5 (fixed)	5 (fixed)	5 (fixed)	5 (fixed)	5 (fixed)	5 (fixed)	5 (fixed)	5 (fixed)	5 (fixed)	5 (fixed)
	$Z_{\rm all}$ (solar)	= $\rm RP_{cold}$	= $\rm RP_{cold}$	= $\rm RP_{cold}$	= $\rm RP_{cold}$	= $\rm RP_{cold}$	= $\rm RP_{cold}$	= $\rm RP_{cold}$	= $\rm RP_{cold}$	= $\rm RP_{cold}$	= $\rm RP_{cold}$
	$n_e t$ (10^{11} s cm^{-3})	= $\rm RP_{cold}$	= $\rm RP_{cold}$	= $\rm RP_{cold}$	= $\rm RP_{cold}$	= $\rm RP_{cold}$	= $\rm RP_{cold}$	= $\rm RP_{cold}$	= $\rm RP_{cold}$	= $\rm RP_{cold}$	= $\rm RP_{cold}$
	VEM (10^{57} cm^{-3})†	$1.4^{+0.2}_{-0.3}$	$0.5^{+0.3}_{-0.2}$	$1.4^{+0.2}_{-0.2}$	$1.4^{+0.2}_{-0.2}$	$0.4^{+0.1}_{-0.1}$	$0.3^{+0.1}_{-0.1}$	$1.5^{+0.2}_{-0.1}$	$2.2^{+0.2}_{-0.2}$	$0.6^{+0.1}_{-0.1}$	$0.6^{+0.1}_{-0.1}$
Gaussian	Centroid (keV)	1.23 (fixed)	1.23 (fixed)	1.23 (fixed)	1.23 (fixed)	1.23 (fixed)	1.23 (fixed)	1.23 (fixed)	1.23 (fixed)	1.23 (fixed)	1.23 (fixed)
	Normalization‡	14^{+7}_{-7}	19^{+11}_{-11}	47^{+10}_{-13}	46^{+13}_{-12}	24^{+13}_{-6}	3^{+9}_{-3}	42^{+11}_{-12}	30^{+8}_{-8}	22^{+8}_{-8}	30^{+10}_{-12}
Power law	Photon index	———	———	———	———	———	———	———	———	———	———
	Normalization*	———	———	———	———	———	———	———	———	———	———
	χ^2_ν (ν)	1.13 (477)	1.15 (477)	1.12 (485)	1.32 (477)	1.17 (477)	1.24 (365)	1.39 (477)	1.30 (477)	1.04 (365)	1.16 (477)

† Volume emission measure at the distance of 1.5 kpc: $VEM = \int n_e n_{\rm H} dV$, where n_e, $n_{\rm H}$, and V are the electron and hydrogen densities, and the emitting volume, respectively.

‡ The unit is photons s^{-1} cm^{-2} sr^{-1}.

* The unit is photons s^{-1} cm^{-2} keV^{-1} sr^{-1} at 1 keV.

Table A.3: Best-fit model parameters of the spectra from regions 11–20.

Model function	Parameter	reg.11	reg.12	reg.13	reg.14	reg.15	reg.16	reg.17	reg.18	reg.19	reg.20
TBabs	$N_{\rm H}$ (10^{22} cm^{-2})	$0.74^{+0.04}_{-0.03}$	$0.81^{+0.02}_{-0.03}$	$0.88^{+0.03}_{-0.03}$	$0.98^{+0.04}_{-0.05}$	$0.77^{+0.03}_{-0.03}$	$0.91^{+0.14}_{-0.09}$	$0.96^{+0.03}_{-0.03}$	$0.85^{+0.04}_{-0.03}$	$0.67^{+0.02}_{-0.03}$	$0.77^{+0.05}_{-0.02}$
VVRNEI	kT_e (keV)	$0.24^{+0.01}_{-0.01}$	$0.22^{+0.01}_{-0.01}$	$0.24^{+0.02}_{-0.02}$	$0.27^{+0.02}_{-0.03}$	$0.20^{+0.02}_{-0.01}$	$0.24^{+0.05}_{-0.05}$	$0.19^{+0.01}_{-0.01}$	$0.25^{+0.05}_{-0.06}$	$0.27^{+0.01}_{-0.01}$	$0.24^{+0.01}_{-0.01}$
(CIE comp.)	$Z_{\rm all}$ (solar)	1 (fixed)	1 (fixed)	1 (fixed)	1 (fixed)	1 (fixed)	1 (fixed)	1 (fixed)	1 (fixed)	1 (fixed)	1 (fixed)
	VEM (10^{57} cm^{-3})†	$2.7^{+0.8}_{-0.4}$	$4.5^{+0.6}_{-0.7}$	$2.1^{+0.6}_{-0.5}$	$0.9^{+0.3}_{-0.3}$	$5.5^{+1.5}_{-1.5}$	$0.7^{+2.0}_{-0.4}$	$5.3^{+1.3}_{-0.7}$	$1.0^{+0.3}_{-0.4}$	$1.3^{+0.2}_{-0.2}$	$1.7^{+0.8}_{-0.6}$
VVRNEI1	kT_e (keV)	$0.24^{+0.05}_{-0.07}$	$0.26^{+0.09}_{-0.08}$	$0.21^{+0.02}_{-0.11}$	$0.19^{+0.02}_{-0.01}$	$0.18^{+0.01}_{-0.01}$	$0.19^{+0.01}_{-0.02}$	$0.19^{+0.04}_{-0.03}$	$0.22^{+0.02}_{-0.02}$	$0.24^{+0.04}_{-0.05}$	$0.22^{+0.09}_{-0.08}$
(RP$_{\rm cold}$ comp.)	$kT_{\rm init}$ (keV)	5 (fixed)	5 (fixed)	5 (fixed)	5 (fixed)	5 (fixed)	5 (fixed)	5 (fixed)	5 (fixed)	5 (fixed)	5 (fixed)
	$Z_{\rm Ne}$ (solar)	$2.0^{+0.3}_{-0.3}$	$6.8^{+5.4}_{-2.9}$	$2.3^{+0.3}_{-0.4}$	$2.4^{+0.5}_{-0.4}$	$4.4^{+0.7}_{-0.6}$	$3.9^{+2.0}_{-0.9}$	$5.0^{+0.4}_{-0.5}$	$1.9^{+0.3}_{-0.3}$	$1.5^{+0.1}_{-0.2}$	$2.6^{+1.1}_{-0.7}$
	$Z_{\rm Mg}$ (solar)	$1.5^{+0.3}_{-0.2}$	$2.9^{+4.1}_{-1.3}$	$1.3^{+0.1}_{-0.3}$	$1.4^{+0.2}_{-0.3}$	$1.9^{+0.3}_{-0.1}$	$2.0^{+0.8}_{-0.5}$	$2.4^{+0.2}_{-0.2}$	$1.1^{+0.1}_{-0.2}$	$1.1^{+0.1}_{-0.1}$	$1.5^{+0.4}_{-0.2}$
	$Z_{\rm Si}$ (solar)	$1.7^{+0.4}_{-0.2}$	$9.5^{+5.3}_{-3.5}$	$1.6^{+0.1}_{-0.2}$	$1.2^{+0.2}_{-0.2}$	$2.3^{+0.3}_{-0.2}$	$1.9^{+0.6}_{-0.3}$	$2.5^{+0.2}_{-0.2}$	$0.7^{+0.1}_{-0.2}$	$0.7^{+0.1}_{-0.1}$	$1.4^{+0.4}_{-0.2}$
	$Z_{\rm S}$ (solar)	$1.1^{+0.2}_{-0.2}$	$6.7^{+14.3}_{-2.5}$	$0.9^{+0.1}_{-0.1}$	$0.8^{+0.1}_{-0.1}$	$1.4^{+0.1}_{-0.2}$	$1.1^{+0.4}_{-0.2}$	$1.8^{+0.2}_{-0.2}$	$0.3^{+0.1}_{-0.1}$	$0.4^{+0.1}_{-0.1}$	$0.8^{+0.3}_{-0.2}$
	$Z_{\rm Ar} = Z_{\rm Ca}$ (solar)	$1.8^{+0.6}_{-0.5}$	$5.2^{+5.4}_{-3.1}$	$0.8^{+0.2}_{-0.2}$	$0.8^{+0.2}_{-0.2}$	$1.4^{+0.3}_{-0.2}$	$1.2^{+0.6}_{-0.5}$	$2.0^{+0.5}_{-0.5}$	$= Z_{\rm S}$	$= Z_{\rm S}$	$= Z_{\rm S}$
	$Z_{\rm Fe} = Z_{\rm Ni}$ (solar)	$0.5^{+0.2}_{-0.1}$	$0.8^{+1.2}_{-0.5}$	$0.3^{+0.1}_{-0.1}$	$0.4^{+0.2}_{-0.2}$	$0.8^{+0.2}_{-0.2}$	$0.7^{+0.5}_{-0.2}$	$0.6^{+0.1}_{-0.2}$	$0.3^{+0.2}_{-0.1}$	$0.2^{+0.1}_{-0.1}$	$0.4^{+0.1}_{-0.1}$
	$n_e t$ (10^{11} s cm^{-3})	$5.8^{+0.5}_{-0.4}$	$5.7^{+0.7}_{-0.5}$	$3.8^{+0.3}_{-0.3}$	$3.8^{+0.4}_{-0.4}$	$4.3^{+0.2}_{-0.1}$	$4.7^{+0.4}_{-0.5}$	$4.8^{+0.2}_{-0.2}$	$5.8^{+0.7}_{-0.7}$	$12.3^{+2.3}_{-1.7}$	$15.1^{+8.3}_{-4.1}$
	VEM (10^{57} cm^{-3})†	$0.5^{+0.4}_{-0.4}$	≤ 0.1	$3.7^{+0.5}_{-0.4}$	$2.3^{+0.3}_{-0.5}$	$3.2^{+0.6}_{-0.5}$	$1.1^{+0.3}_{-0.4}$	$1.7^{+0.6}_{-0.8}$	$1.5^{+0.6}_{-0.4}$	≤ 0.2	$0.2^{+0.4}_{-0.2}$
VVRNEI3	kT_e (keV)	$0.54^{+0.03}_{-0.08}$	$0.63^{+0.10}_{-0.08}$	$0.48^{+0.07}_{-0.19}$	$0.59^{+0.07}_{-0.14}$	$0.54^{+0.04}_{-0.03}$	$0.64^{+0.06}_{-0.11}$	$0.55^{+0.04}_{-0.04}$	$0.63^{+0.07}_{-0.04}$	$0.62^{+0.02}_{-0.01}$	$0.62^{+0.03}_{-0.04}$
(RP$_{\rm hot}$ comp.)	$kT_{\rm init}$ (keV)	5 (fixed)	5 (fixed)	5 (fixed)	5 (fixed)	5 (fixed)	5 (fixed)	5 (fixed)	5 (fixed)	5 (fixed)	5 (fixed)
	$Z_{\rm all}$ (solar)	= RP$_{\rm cold}$	= RP$_{\rm cold}$	= RP$_{\rm cold}$	= RP$_{\rm cold}$	= RP$_{\rm cold}$	= RP$_{\rm cold}$	= RP$_{\rm cold}$	= RP$_{\rm cold}$	= RP$_{\rm cold}$	= RP$_{\rm cold}$
	$n_e t$ (10^{11} s cm^{-3})	= RP$_{\rm cold}$	= RP$_{\rm cold}$	= RP$_{\rm cold}$	= RP$_{\rm cold}$	= RP$_{\rm cold}$	= RP$_{\rm cold}$	= RP$_{\rm cold}$	= RP$_{\rm cold}$	= RP$_{\rm cold}$	= RP$_{\rm cold}$
	VEM (10^{57} cm^{-3})†	$0.5^{+0.3}_{-0.2}$	$0.1^{+0.1}_{-0.1}$	$1.2^{+1.1}_{-1.0}$	$0.5^{+0.4}_{-0.1}$	$0.9^{+0.2}_{-0.1}$	$0.3^{+0.1}_{-0.1}$	$0.7^{+0.2}_{-0.1}$	$0.3^{+0.1}_{-0.1}$	$0.8^{+0.1}_{-0.1}$	$0.3^{+0.1}_{-0.1}$
Gaussian	Centroid (keV)	1.23 (fixed)	1.23 (fixed)	1.23 (fixed)	1.23 (fixed)	1.23 (fixed)	1.23 (fixed)	1.23 (fixed)	1.23 (fixed)	1.23 (fixed)	1.23 (fixed)
	Normalization‡	28^{+8}_{-8}	5^{+4}_{-5}	12^{+7}_{-7}	15^{+8}_{-4}	9^{+5}_{-5}	11^{+7}_{-8}	4^{+4}_{-4}	4^{+3}_{-2}	5^{+1}_{-1}	6^{+2}_{-2}
Power law	Photon index	————	————	————	————	————	1.89 (fixed)	1.89 (fixed)	————	————	2.22 (fixed)
	Normalization*	————	————	————	————	————	45^{+9}_{-9}	97^{+7}_{-7}	————	————	18^{+4}_{-5}
	χ^2_ν (ν)	1.18 (365)	1.35 (250)	1.25 (477)	1.22 (365)	1.53 (477)	1.13 (364)	1.36 (476)	1.19 (273)	1.27 (257)	1.18 (256)

† Volume emission measure at the distance of 1.5 kpc: $VEM = \int n_e n_{\rm H} dV$, where n_e, $n_{\rm H}$, and V are the electron and hydrogen densities, and the emitting volume, respectively.

‡ The unit is photons s^{-1} cm^{-2} sr^{-1}.

* The unit is photons s^{-1} cm^{-2} keV^{-1} sr^{-1} at 1 keV.

Appendix B

Spatially resolved spectroscopy of W44

B.1 Fitting results of the spectra in the regions 2–10

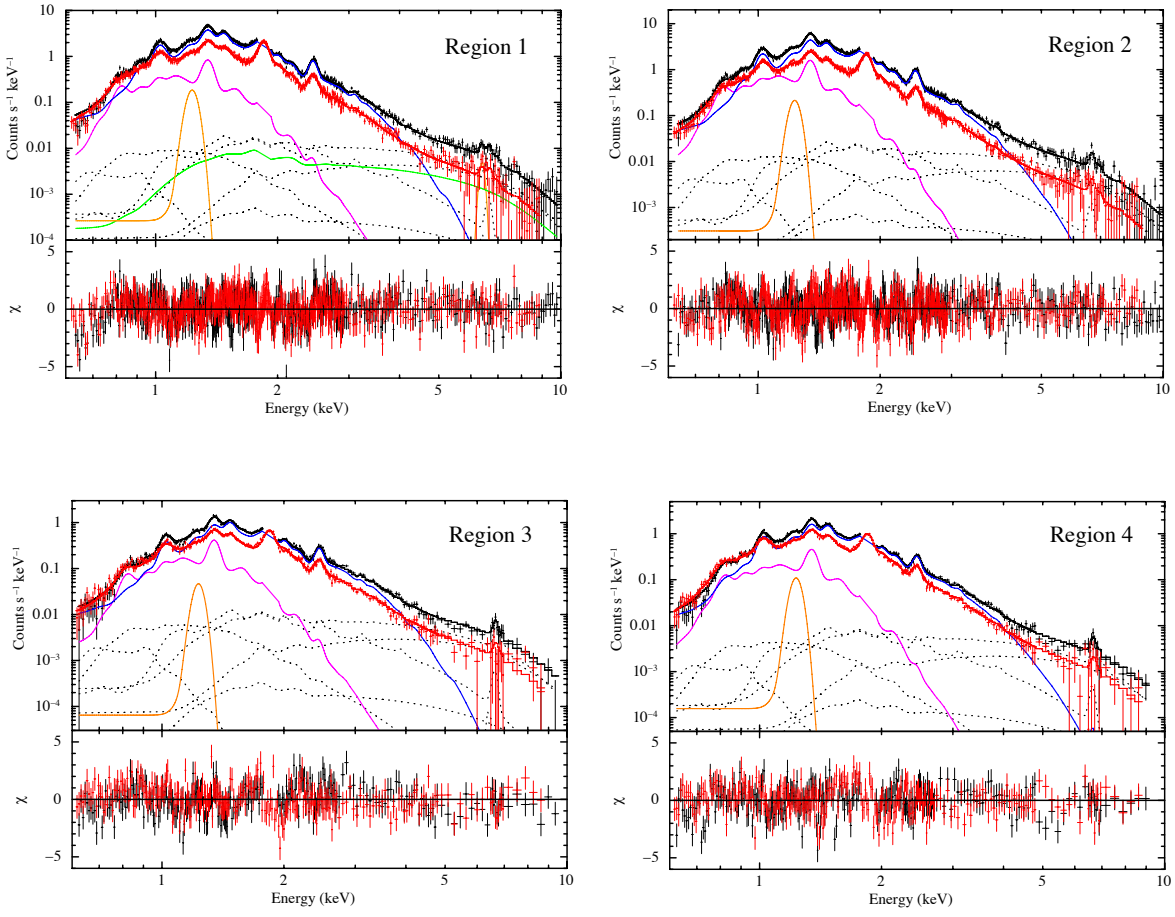

Figure B.1: Same as Figure 7.5 but for regions 1–4.

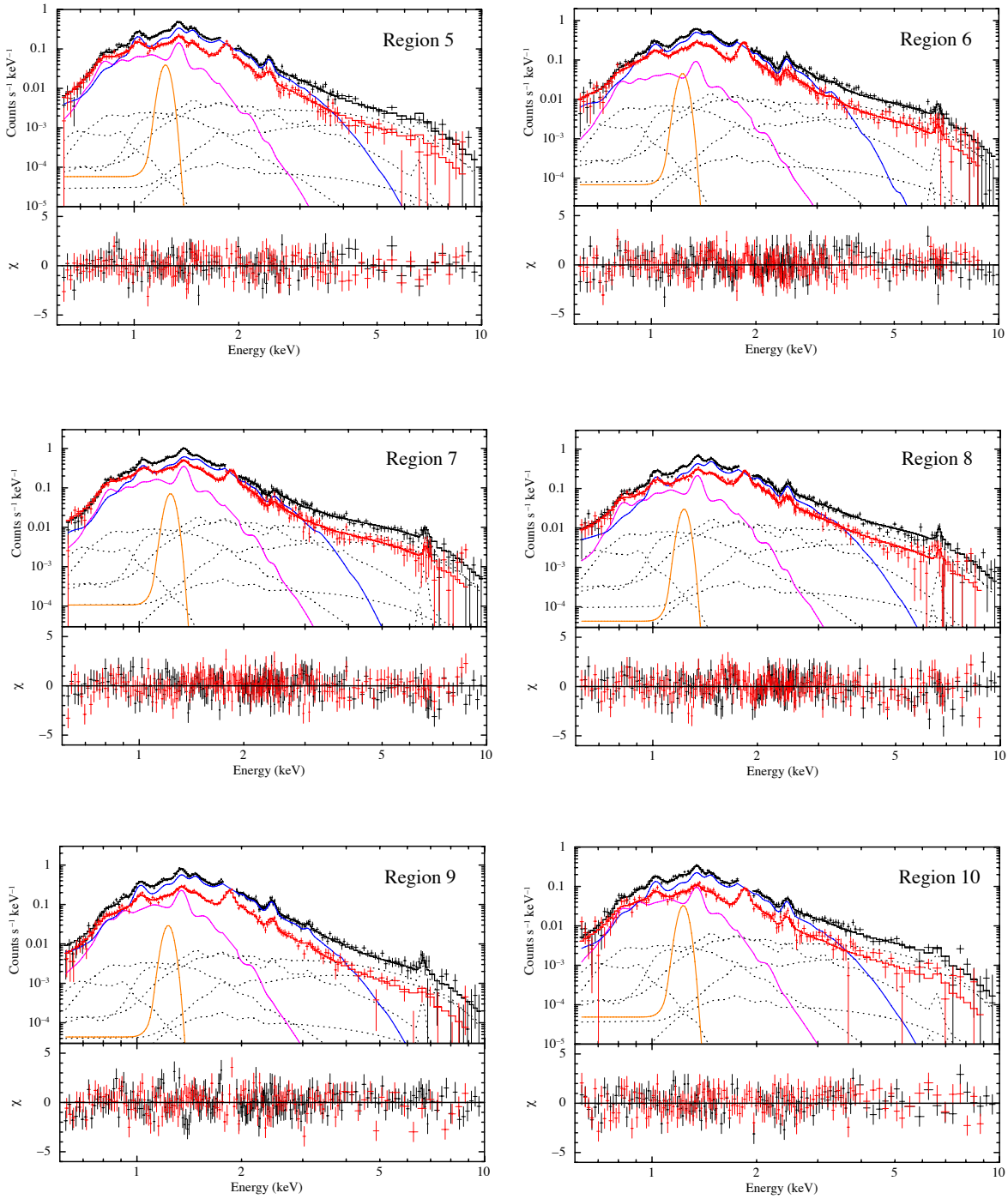

Figure B.2: Same as Figure 7.5 but for regions 5–10.

Table B.1: Best-fit model parameters of the spectra from regions 2–10.

Model function	Parameter	reg.2	reg.3	reg.4	reg.5	reg.6	reg.7	reg.8	reg.9	reg.10
TBabs	$N_{\rm H}$ (10^{22} cm^{-2})	$2.03\ ^{+0.01}_{-0.02}$	$2.19\ ^{+0.07}_{-0.05}$	1.96 ± 0.03	1.87 ± 0.06	1.93 ± 0.06	$2.03\ ^{+0.07}_{-0.06}$	$2.16\ ^{+0.06}_{-0.07}$	2.14 ± 0.05	$1.90\ ^{+0.08}_{-0.09}$
VVRNEI1	kT_e (keV)	0.22 ± 0.01	$0.23\ ^{+0.01}_{-0.02}$	$0.20\ ^{+0.02}_{-0.01}$	$0.20\ ^{+0.03}_{-0.01}$	$0.20\ ^{+0.03}_{-0.02}$	$0.21\ ^{+0.01}_{-0.02}$	$0.21\ ^{+0.01}_{-0.02}$	0.18 ± 0.01	$0.18\ ^{+0.03}_{-0.01}$
(CIE comp.)	$Z_{\rm all}$ (solar)	$= Z_{\rm all,Whole}$	$= Z_{\rm all,Whole}$	$= Z_{\rm all,Whole}$	$= Z_{\rm all,Whole}$	$= Z_{\rm all,Whole}$	$= Z_{\rm all,Whole}$	$= Z_{\rm all,Whole}$	$= Z_{\rm all,Whole}$	$= Z_{\rm all,Whole}$
	Normalization†	$12.47\ ^{+1.64}_{-3.10}$	$5.13\ ^{+2.35}_{-1.58}$	$11.78\ ^{+3.17}_{-3.06}$	$6.35\ ^{+3.56}_{-2.96}$	$1.82\ ^{+1.74}_{-1.17}$	$4.72\ ^{+2.79}_{-1.94}$	$3.13\ ^{+1.60}_{-1.18}$	$17.55\ ^{+8.78}_{-5.84}$	$4.50\ ^{+3.69}_{-2.72}$
VVRNEI2	kT_e (keV)	$0.42\ ^{+0.01}_{-0.02}$	0.35 ± 0.01	0.44 ± 0.02	$0.38\ ^{+0.05}_{-0.04}$	0.26 ± 0.01	0.28 ± 0.02	$0.37\ ^{+0.05}_{-0.03}$	0.42 ± 0.04	$0.37\ ^{+0.13}_{-0.05}$
(RP comp.)	$kT_{\rm init}$ (keV)	0.93 (fixed)	0.93 (fixed)	0.93 (fixed)	0.93 (fixed)	0.93 (fixed)	0.93 (fixed)	0.93 (fixed)	0.93 (fixed)	0.93 (fixed)
	$Z_{\rm O} = Z_{\rm Ne}$ (solar)	3.6 (fixed)	3.6 (fixed)	3.6 (fixed)	3.6 (fixed)	3.6 (fixed)	3.6 (fixed)	3.6 (fixed)	3.6 (fixed)	3.6 (fixed)
	$Z_{\rm Mg}$ (solar)	$2.5\ ^{+0.2}_{-0.1}$	2.9 ± 0.3	2.8 ± 0.2	$2.7\ ^{+0.6}_{-0.4}$	3.0 ± 0.3	2.1 ± 0.5	$2.6\ ^{+0.5}_{-0.4}$	2.3 ± 0.3	$2.8\ ^{+0.8}_{-0.6}$
	$Z_{\rm Si}$ (solar)	4.1 ± 0.2	$4.8\ ^{+0.3}_{-0.5}$	$3.1\ ^{+0.2}_{-0.3}$	$3.4\ ^{+0.8}_{-0.6}$	7.9 ± 0.7	$3.5\ ^{+0.7}_{-0.6}$	$3.6\ ^{+0.8}_{-0.7}$	$3.0\ ^{+0.5}_{-0.6}$	$4.9\ ^{+1.4}_{-1.6}$
	$Z_{\rm S}$ (solar)	$3.5\ ^{+0.3}_{-0.2}$	$4.6\ ^{+0.5}_{-0.6}$	2.6 ± 0.4	$3.0\ ^{+1.4}_{-0.8}$	$7.9\ ^{+1.5}_{-1.3}$	$2.3\ ^{+1.3}_{-0.9}$	$3.2\ ^{+0.9}_{-0.7}$	2.6 ± 0.7	$4.2\ ^{+2.6}_{-2.3}$
	$Z_{\rm Ar} = Z_{\rm Ca}$ (solar)	$5.4\ ^{+1.3}_{-1.2}$	$7.3\ ^{+3.2}_{-1.8}$	$3.4\ ^{+1.1}_{-1.5}$	$3.7\ ^{+8.8}_{-3.5}$	$= Z_{\rm S}$	$= Z_{\rm S}$	$1.9\ ^{+4.2}_{-1.7}$	$5.4\ ^{+4.4}_{-3.4}$	$= Z_{\rm S}$
	$Z_{\rm Fe} = Z_{\rm Ni}$ (solar)	< 0.09	< 0.36	$0.31\ ^{+0.11}_{-0.10}$	< 0.76	< 0.49	< 1.7	< 0.49	$0.43\ ^{+0.25}_{-0.19}$	< 1.0
	$n_e t$ (10^{11} s cm^{-3})	4.1 ± 0.1	2.2 ± 0.3	3.1 ± 0.2	$3.7\ ^{+0.3}_{-0.5}$	4.0 ± 0.4	$4.9\ ^{1.1}_{1.0}$	$2.0\ ^{+0.6}_{-0.4}$	$3.7\ ^{+0.5}_{-0.4}$	$3.9\ ^{+0.8}_{-0.7}$
	Normalization†	$2.00\ ^{+0.07}_{-0.06}$	1.10 ± 0.07	$1.90\ ^{+0.08}_{-0.10}$	$0.77\ ^{+0.12}_{-0.09}$	$0.63\ ^{+0.05}_{-0.06}$	$0.70\ ^{+0.16}_{-0.11}$	$0.44\ ^{+0.05}_{-0.04}$	$1.15\ ^{+0.12}_{-0.13}$	$0.31\ ^{+0.08}_{-0.12}$
Gaussian	Centroid (keV)	1.23 (fixed)	1.23 (fixed)	1.23 (fixed)	1.23 (fixed)	1.23 (fixed)	1.23 (fixed)	1.23 (fixed)	1.23 (fixed)	1.23 (fixed)
	Normalization‡	38 ± 8	17 ± 8	$52\ ^{+12}_{-13}$	$31\ ^{+12}_{-11}$	14 ± 5	$18\ ^{+6}_{-5}$	$9\ ^{+6}_{-5}$	22 ± 14	$16\ ^{+7}_{-6}$
	χ^2_ν (ν)	1.39 (1100)	1.37 (499)	1.41 (498)	1.08 (265)	1.09 (395)	1.02 (395)	1.19 (394)	1.33 (328)	1.26 (266)

† The emission measure integrated over the line of sight, i.e., $(1\ /\ 4\pi) \int n_e n_{\rm H} dl$ in units of 10^{18} cm^{-5} sr^{-1}.

‡ The unit is photons s^{-1} cm^{-2} sr^{-1}.

* The unit is photons s^{-1} cm^{-2} keV^{-1} sr^{-1} at 1 keV.

Acknowledgement

I am deeply grateful to Dr. Takaaki Tanaka, Dr. Hiroyuki Uchida, and Prof. Takeshi Go Tsuru for their helpful advice and support. I am very grateful to my collaborators, Dr. Masatoshi Nobukawa, Dr. Kumiko Kawabata Nobukawa, Mr. Makoto Itou, and Mr. Hiromichi Okon. I would like to thank Dr. Satoshi Yoshiike for providing us with the NANTEN2 data. I also grateful to the Suzaku team members for their constant efforts. This work is supported by Research Fellowships of the Japan Society for the Promotion of Science for Young Scientists. I am indebted to my friends and family for their understanding and kind supports.

Reference

Suzaku XIS document, September 2007,
http://www.astro.isas.ac.jp/suzaku/doc/suzakumemo/suzakumemo-2007-08.pdf

Suzaku XIS document, January 2010,
http://www.astro.isas.ac.jp/suzaku/doc/suzakumemo/suzakumemo-2010-01.pdf

Suzaku Technical Description, January 2015,
https://heasarc.gsfc.nasa.gov/docs/suzaku/prop_tools/suzaku_td/

Report of the flickering pixels in the XIS, April 2016,
https://heasarc.gsfc.nasa.gov/docs/suzaku/analysis/xisnxbnew.html

Abdo, A. A., Ackermann, M., Ajello, M., et al. 2010, ApJ, 722, 1303

Anders, E., & Grevesse, N. 1989, *Geochim. Cosmochim. Acta*, 53, 197

Araya, M. 2013, MNRAS, 434, 2202

Arnaud, M., & Rothenflug, R. 1985, A&AS, 60, 425

Arnaud, M., & Raymond, J. 1992, ApJ, 398, 394

Barbon, R., Ciatti, F., & Rosino, L. 1973, A&A, 29, 57

Bautz, M. W., Kissel, S. E., Prigozhin, G. Y., et al. 2004, *Proc. SPIE*, 5501, 111

Bocchino, F., & Bykov, A. M. 2001, A&A, 376, 248

Bocchino, F., & Bykov, A. M. 2003, A&A, 400, 203

Bocchino, F., Miceli, M., & Troja, E. 2009, A&A, 498, 139

Borkowski, K. J., Reynolds, S. P., & Roberts, M. S. E. 2016, ApJ, 819, 160

Burrows, D. N., & Guo, Z. 1994, ApJL, 421, L19

Chen, Y., Zhou, P., & Chu, Y.-H. 2013, ApJL, 769, L16

Chevalier, R. A. 1974, ApJ, 188, 501

Claussen, M. J., Frail, D. A., Goss, W. M., & Gaume, R. A. 1997, ApJ, 489, 143

Cioffi, D. F., McKee, C. F., & Bertschinger, E. 1988, ApJ, 334, 252

Cornett, R. H., Chin, G., & Knapp, G. R. 1977, A&A, 54, 889

Cox, D. P., Shelton, R. L., Maciejewski, W., et al. 1999, ApJ, 524, 179

Cowie, L. L., & McKee, C. F. 1977, ApJ, 211, 135

Dalton, W. W., & Balbus, S. A. 1993, ApJ, 404, 625

David, L. P., Slyz, A., Jones, C., et al. 1993, ApJ, 412, 479

Denoyer, L. K. 1979, ApJL, 232, L165

Dickey, J. M., & Lockman, F. J. 1990, ARA&A, 28, 215

Elias, J. H., Matthews, K., Neugebauer, G., & Persson, S. E. 1985, ApJ, 296, 379

Ergin, T., Sezer, A., Saha, L., et al. 2014, ApJ, 790, 65

Ergin, T., Sezer, A., Sano, H., Yamazaki, R., & Fukui, Y. 2017, ApJ, 842, 22

Fairley, B. W., Jones, L. R., Scharf, C., et al. 2000, MNRAS, 315, 669

Fesen, R. A., & Kirshner, R. P. 1980, ApJ, 242, 1023

Guo, Z., & Burrows, D. N. 1997, ApJL, 480, L51

Hayato, A., Yamaguchi, H., Tamagawa, T., et al. 2010, ApJ, 725, 894

Helfand, D. J., Becker, R. H., White, R. L., Fallon, A., & Tuttle, S. 2006, AJ, 131, 2525

Helsdon, S. F., & Ponman, T. J. 2000, MNRAS, 315, 356

H. E. S. S. Collaboration, Abdalla, H., Abramowski, A., et al. 2016, arXiv:1609.00600

Ishisaki, Y., Maeda, Y., Fujimoto, R., et al. 2007, PASJ, 59, 113

Itoh, H., & Masai, K. 1989, MNRAS, 236, 885

Iwamoto, K., Brachwitz, F., Nomoto, K., et al. 1999, ApJS, 125, 439

Kamitsukasa, F., Koyama, K., Uchida, H., et al. 2015, PASJ, 67, 16

Kamitsukasa, F., Koyama, K., Nakajima, H., et al. 2016, PASJ, 68, S7

Katayama, H., Takahashi, I., Ikebe, Y., Matsushita, K., & Freyberg, M. J. 2004, A&A, 414, 767

Kawasaki, M. T., Ozaki, M., Nagase, F., et al. 2002, ApJ, 572, 897

Kawasaki, M., Ozaki, M., Nagase, F., Inoue, H., & Petre, R. 2005, ApJ, 631, 935

Kelley, R. L., Mitsuda, K., Allen, C. A., et al. 2007, PASJ, 59, 77

Keohane, J. W., Reach, W. T., Rho, J., & Jarrett, T. H. 2007, ApJ, 654, 938

Kokubun, M., Makishima, K., Takahashi, T., et al. 2007, PASJ, 59, 53

Kokusho, T., Nagayama, T., Kaneda, H., et al. 2013, ApJL, 768, L8

Koyama, K., Tsunemi, H., Dotani, T., et al. 2007, PASJ, 59, 23

Kundu, M. R., & Velusamy, T. 1972, A&A, 20, 237

LaMarr, B., Bautz, M. W., Kissel, S. E., et al. 2004, *Proc. SPIE*, 5501, 385

Landecker, T. L., Pineault, S., Routledge, D., & Vaneldik, J. F. 1982, ApJL, 261, L41

Lazendic, J. S., & Slane, P. O. 2006, ApJ, 647, 350

Lee, J.-J., Koo, B.-C., Yun, M. S., et al. 2008, AJ, 135, 796

Lopez, L. A., Ramirez-Ruiz, E., Castro, D., & Pearson, S. 2013a, ApJ, 764, 50

Lopez, L. A., Pearson, S., Ramirez-Ruiz, E., et al. 2013b, ApJ, 777, 145

Lu, F. J., Ge, M. Y., Zheng, S. J., et al. 2015, ApJ, 805, 142

Masai, K. 1994, ApJ, 437, 770

Maeda, K., Röpke, F. K., Fink, M., et al. 2010, ApJ, 712, 624

Masui, K., Mitsuda, K., Yamasaki, N. Y., et al. 2009, PASJ, 61, S115

Matsumura, H., Uchida, H., Tanaka, T., et al. 2017, PASJ, 69, 30

Matsumura, H., Tanaka, T., Uchida, H., et al. 2017, ApJ, Accepted

McKee, C. F. 1974, ApJ, 188, 335

McKee, C. F., & Cowie, L. L. 1975, ApJ, 195, 715

McKee, C. F., & Ostriker, J. P. 1977, ApJ, 218, 148

Minkowski, R. 1939, ApJ, 89, 156

Minkowski, R. 1940, PASP, 52, 206

Mitsuda, K., Bautz, M., Inoue, H., et al. 2007, PASJ, 59, S1

Moffett, D. A., & Reynolds, S. P. 1994, ApJ, 437, 705

Mori, H., Iizuka, R., Shibata, R., et al. 2005, PASJ, 57, 245

Moriya, T. J. 2012, ApJL, 750, L13

Morrison, R., & McCammon, D. 1983, ApJ, 270, 119

Mushotzky, R. F., & Scharf, C. A. 1997, ApJL, 482, L13

Nakajima, H., Yamaguchi, H., Matsumoto, H., et al. 2008, PASJ, 60, S1

Nobukawa, K. K., Nobukawa, M., Uchiyama, H., et al. 2015, ApJL, 807, L10

Nomoto, K., Thielemann, F.-K., & Yokoi, K. 1984, ApJ, 286, 644

Olbert, C. M., Clearfield, C. R., Williams, N. E., Keohane, J. W., & Frail, D. A. 2001, ApJL, 554, L205

Ohnishi, T., Koyama, K., Tsuru, T. G., et al. 2011, PASJ, 63, 527

Ohnishi, T., Uchida, H., Tsuru, T. G., & Koyama, K., 2014, ApJ, 784, 74

Ozawa, M., Uchiyama, H., Matsumoto, H., et al. 2009a, PASJ, 61, S1

Ozawa, M., Koyama, K., Yamaguchi, H., Masai, K., & Tamagawa, T. 2009b, ApJL, 706, L71

Petre, R., Szymkowiak, A. E., Seward, F. D., & Willingale, R. 1988, ApJ, 335, 215

Petre, R., Kuntz, K. D., & Shelton, R. L. 2002, ApJ, 579, 404

Pineault, S., Landecker, T. L., & Routledge, D. 1987, ApJ, 315, 580

Porquet, D., Mewe, R., Dubau, J., Raassen, A. J. J., & Kaastra, J. S. 2001, A&A, 376, 1113

Prigozhin, G. Y., Kissel, S. E., Bautz, M. W., et al. 2000, *Proc. SPIE*, 4140, 123

Pye, J. P., Becker, R. H., Seward, F. D., & Thomas, N. 1984, MNRAS, 207, 649

Radhakrishnan, V., Goss, W. M., Murray, J. D., & Brooks, J. W. 1972, ApJS, 24, 49

Rho, J., Petre, R., Schlegel, E. M., & Hester, J. J. 1994, ApJ, 430, 757

Rho, J., & Petre, R. 1998, ApJL, 503, L167

Ruiz-Lapuente, P., Comeron, F., Méndez, J., et al. 2004, Nature, 431, 1069

Rybicki, G. B., & Lightman, A. P. 1979, New York, Wiley-Interscience, 1979, Radiative process in astrophysics

Sato, T., Koyama, K., Takahashi, T., Odaka, H., & Nakashima, S. 2014, PASJ, 66, 124

Sato, T., Koyama, K., Lee, S.-H., & Takahashi, T. 2016, PASJ, 68, S8

Sawada, M., PhD thesis, Kyoto University, 2011.

Sawada, M., & Koyama, K. 2012, PASJ, 64, 81

Serlemitsos, P. J., Soong, Y., Chan, K.-W., et al. 2007, PASJ, 59, S9

Seta, M., Hasegawa, T., Sakamoto, S., et al. 2004, AJ, 127, 1098

Sharpless, S. 1959, ApJS, 4, 257

Shelton, R. L., Cox, D. P., Maciejewski, W., et al. 1999, ApJ, 524, 192

Shimizu, T., Masai, K., & Koyama, K. 2012, PASJ, 64, 24

Simon, R., Jackson, J. M., Clemens, D. P., Bania, T. M., & Heyer, M. H. 2001, ApJ, 551, 747

Smith, A., Peacock, A., Jones, L. R., & Pye, J. P. 1985, ApJ, 296, 469

Smith, R. K., Odaka, H., Audard, M., et al. 2014, arXiv:1412.1172

Slane, P., Helfand, D. J., van der Swaluw, E., & Murray, S. S. 2004, ApJ, 616, 403

Spitzer, L. 1956, Physics of Fully Ionized Gases, New York: Interscience Publishers, 1956,

Sutherland, R. S., & Dopita, M. A. 1993, ApJS, 88, 253

Swartz, D. A., Pavlov, G. G., Clarke, T., et al. 2015, ApJ, 808, 84

Takahashi, T., Abe, K., Endo, M., et al. 2007, PASJ, 59, 35

Tawa, N., Hayashida, K., Nagai, M., et al. 2008, PASJ, 60, S11

Troja, E., Bocchino, F., & Reale, F et al. 2006, ApJ, 649, 258

Truelove, J. K., & McKee, C. F. 1999, ApJS, 120, 299

Uchida, H., Tsunemi, H., Katsuda, S., et al. 2009, PASJ, 61, 503

Uchida, H., Koyama, K., Yamaguchi, H., et al. 2012, PASJ, 64, 141

Uchida, H., Koyama, K., & Yamaguchi, H. 2015, ApJ, 808, 77

Uchiyama, H., Ozawa, M., Matsumoto, H., et al. 2009, PASJ, 61, S9

Uchiyama, H., Nobukawa, M., Tsuru, T. G., & Koyama, K. 2013, PASJ, 65, 19

Vink, J. 2012, A&AR, 20, 49

Washino, R., Uchida, H., Nobukawa, M., et al. 2016, PASJ, 68, S4

Webbink, R. F. 1984, ApJ, 277, 355

Welsh, B. Y., & Sallmen, S. 2003, A&A, 408, 545

Wheeler, J. C., Harkness, R. P., Barker, E. S., Cochran, A. L., & Wills, D. 1987, ApJL, 313, L69

Wheeler, J. C., & Harkness, R. P. 1990, *Reports on Progress in Physics*, 53, 1467

Whelan, J., & Iben, I., Jr. 1973, ApJ, 186, 1007

White, R. L., & Long, K. S. 1991, ApJ, 373, 543

Wilms, J., Allen, A., & McCray, R. 2000, ApJ, 542, 914

Wolszczan, A., Cordes, J. M., & Dewey, R. J. 1991, ApJL, 372, L99

Woosley, S. E., & Weaver, T. A. 1995, ApJS, 101, 181

Xu, J.-L., Wang, J.-J., & Miller, M. 2011, ApJ, 727, 81

Yamanaka, M., Kawabata, K. S., Kinugasa, K., et al. 2009, ApJL, 707, L118

Yamaguchi, H., Ozawa, M., Koyama, K., et al. 2009, ApJL, 705, L6

Yamaguchi, H., Koyama, K., & Uchida, H. 2011, PASJ, 63, S837

Yamauchi, S., Nobukawa, M., Koyama, K., & Yonemori, M. 2013, PASJ, 65, 6

Yamauchi, S., Minami, S., Ota, N., & Koyama, K. 2014, PASJ, 66, 2

Yoshiike, S., PhD. thesis, Nagoya University, 2017.

Zeldovich, Y. B., & Raizer, Y. P. 1966, New York: Academic Press, 1966, edited by Hayes, W.D.; Probstein, Ronald F.,

Zhou, P., & Vink, J. 2017, arXiv:1707.05107